



An experimental study on the drag  
and inertia forces due to mussel  
growth on vertical poles exposed to  
waves



# An experimental study on the drag and inertia forces due to mussel growth on vertical poles exposed to waves

by

E. te Velde

in partial fulfilment of the degree of Master of Science  
at the Delft University of Technology,  
to be defended publicly on Tuesday May 12, 2022 at 15:45 PM.

Student number:	4358996	
Project duration:	May 15, 2021 - May 12, 2022	
Thesis committee:	Prof. dr. ir. W.S.J. Uijtewaal,	TU Delft, chair
	Dr. Ir. B. Hofland,	TU Delft
	Prof. dr. ir. J.C. Winterwerp,	TU Delft
	Ir. A. Gijón Mancheño,	TU Delft, supervisor
	Ir. T. Wilms,	Witteveen+Bos, supervisor

An electronic version of this thesis is available at <http://repository.tudelft.nl/>.

# Preface

This thesis marks the end of my time in Delft, where I've made numerous memories and many friends. It was a time which I will never forget. The process of graduation has been a challenging but rewarding experience. I can't wait to start a new chapter in my life, but I first want to thank some people who have helped along the way.

I want to thank my committee. First of all, Alejandra. You have been of enormous help during my thesis, and I could not have wished for a better mentor. I appreciate your honesty, our non-study related conversations, support, and feedback. I wish you all the best and good luck on your defence. Then, I want to thank Tom for your time and for introducing me to Witteveen+Bos. I really enjoyed my time at Witteveen+Bos, especially when we were allowed to go to the office. Thank you for all your efforts in the report and the nice and helpful meetings. Wim, Bas, and Han thank you so much for your comments and feedback on the report. Lastly, I want to thank Ad Reniers, who was not on my committee but was so kind to meet me and help with my cnoidal waves and the results.

Then I would like to thank Flip for helping me with my physical model during your holidays. I know that rotating every mussel to the correct angle was not the most fun thing, but thank you for making it work. Your input and knowledge on 3D printing and modelling are appreciated. Next, I want to thank Pieter, Chantal, Arie, Arno, Frank and Sander for your tremendous help during the experiment. So many things went wrong during my experiments, but you have helped me in every way.

Lastly, I want to thank my boyfriend, roommates, family and friends for always supporting me and believing in me. Without you, all of this would not have been possible.

*E. te Velde*  
*Delft, May 12 2022*

# Summary

Mangroves trap sediment and are the first coastal defence line for many coastal areas. Unfortunately, mangrove coasts worldwide are eroding due to deforestation, exposing local communities to flood hazards. In Demak, Indonesia, a Building with Nature approach was chosen to counteract erosion by rehabilitating mangroves. Permeable dams were built on the foreshore to attenuate waves and restore the sediment balance. The dams have increased the bed level locally and mangroves expand after construction. However, juvenile mangroves did not survive due to subsidence rates in the area. A new project called MuMaCo (Mussels as Mangrove facilitators for Coastal defence) is launched to integrate mussel aquaculture into the mangrove rehabilitation project in Demak. Mussels increase the roughness and diameter of the bamboo poles, which could increase their wave attenuation capacity. Moreover, mussel culture gives the local communities an economic incentive to sustain the structures. The effect of bamboo structures on waves and currents depends on the hydrodynamic forces acting on the poles, and such processes could be affected by the presence of mussels. This thesis describes and quantifies how mussels' growth influences the forces acting on bamboo poles. Small-scale experiments are performed in the wave flume of the Delft University of Technology on a scale of 1:3 and 1:6. The physical model consists of two 3D-printed semi-circular cylindrical shells with realistic mussel growth. The shells are mounted around vertical aluminium cylinders with screws. The model is based on an existing model from literature and improves it by using a mussel shape, distribution and orientation. Three different models are designed, namely a mussel with a marketable size for a scale of 1:6 ('Standard mussel') and a marketable size for a scale of 1:3 ('Large mussel') and a half-grown size for 1:3 ('Medium Mussel'). The physical models were used for experiments with steady flow and waves. The steady flow experiments cover a range of Reynolds ( $Re$ ) numbers between  $10^3$  and  $10^4$  to seek the drag coefficient crisis. Single mussel covered cylinders for both scales are compared to smooth cylinders and cylinders with an equivalent diameter. For the wave experiments, cnoidal waves with Keulegan-Carpenter ( $KC$ ) numbers ranging from 3 to 113 that correspond with measured waves in Demak are chosen. Moreover, only mussel covered cylinders are compared to a smooth cylinder for a scale of 1:6. Fenton theory is used to define the paddle motion of the wave generator to create cnoidal waves. During the experiments, the flow velocity, force, and surface elevation are measured, and the drag and inertia coefficients are obtained with the help of the Morison equation. The drag coefficient shows a clear relationship with the Reynolds numbers for steady flow. The drag coefficient exponentially decrease for  $Re < 2000$  and stabilizes for  $Re > 2000$ . Although the drag coefficients display the same qualitative behaviour as in other studies in the literature, the drag coefficients of the smooth cylinder are more than 40 % larger than in the literature. This is probably due to large variations in the offset of the velocity meters (EMS) during the experiments. The large mussels show higher drag coefficients than the smooth cylinder. There is no clear difference between the medium mussel, standard mussel, and smooth cylinder. Also, the graphs of the drag coefficients do not show any evidence of the drag crisis. For the wave experiments, the drag coefficients show good correspondence to other studies in the literature, but the inertia coefficients are a factor two larger than expected for smooth cylinders. Treating the peak and trough of the cnoidal wave as individual sinusoidal waves shows similar results and suggest that cnoidal waves can be represented by  $KC$  numbers, as it is done for linear waves. The best fit to the literature values was found by solving the Morison equation with the measured force with the depth-integrated velocity squared and acceleration from the Fenton theory. This suggests that the results of the wave experiments have been uncertain due to inaccuracies in the EMS recordings. All three methods show no difference between the smooth and mussel covered cylinders. This thesis presents a method to schematize mussels for laboratory experiments and provides a qualitative comparison of the forces acting on poles with and without mussels. For future experiments, it is recommended to use a scale of 1:3 because it showed significant differences between the smooth and mussel covered cylinder. Moreover, more than one type of sensor should be used to measure the velocity, as the inaccuracies in the results are likely to stem from the EMF recordings. Defining the changes in the drag coefficient with and without mussels would enable quantifying how much extra wave dissipation is provided by mussels. This would be helpful to study the economic feasibility of integrating mussel aquaculture in structures for mangrove restoration.

# Contents

List of Figures	vii
List of Tables	xii
1 Introduction	1
1.1 Problem indication . . . . .	1
1.2 Objective and research questions . . . . .	2
1.3 Research approach and thesis outline. . . . .	2
2 Theoretical background	4
2.1 Steady flow around a cylinder. . . . .	4
2.2 Forces on a cylinder in a steady flow . . . . .	7
2.3 Forces on a cylinder in oscillatory motion. . . . .	8
2.4 Flow around a cylinder in oscillatory flow. . . . .	8
2.5 The effect of roughness elements . . . . .	9
2.6 Waves and wave conditions in Demak . . . . .	11
2.7 Cnoidal waves . . . . .	13
3 Methodology	14
3.1 Physical model . . . . .	14
3.1.1 Scaling. . . . .	14
3.1.2 The base of the physical model . . . . .	15
3.1.3 Construction around the cylinder . . . . .	15
3.1.4 Realistic modelling of mussel growth . . . . .	15
3.1.5 Mussel characteristics in Demak. . . . .	15
3.1.6 Final design of the physical model . . . . .	17
3.2 Laboratory experiments. . . . .	19
3.2.1 General wave flume properties. . . . .	19
3.2.2 Data collection. . . . .	19
3.2.3 Experimental program. . . . .	20
3.2.4 Wave generation . . . . .	21
3.2.5 Set-up wave flume . . . . .	22
3.3 Data processing of the steady flow . . . . .	23
3.3.1 General outline for the steady flow. . . . .	23
3.4 Data processing for the waves. . . . .	24
3.4.1 General outline for the waves . . . . .	24
3.4.2 Low pass filter . . . . .	25
3.4.3 Calculation of the phase velocity. . . . .	26
4 Results	27
4.1 General . . . . .	27
4.1.1 Equivalent Diameter . . . . .	27
4.2 Results of the steady flow experiments . . . . .	28
4.2.1 Velocity profile . . . . .	28
4.2.2 Drag coefficients. . . . .	29
4.2.3 Summary of the results of the steady flow experiments . . . . .	30
4.3 Results of the wave experiments . . . . .	30
4.3.1 Surface elevation. . . . .	31
4.3.2 Vertical velocity and acceleration profile. . . . .	33
4.3.3 Depth integrated velocity squared and acceleration. . . . .	35
4.3.4 The drag and inertia coefficients. . . . .	36
4.3.5 Summary of results of the wave results. . . . .	37

5	Discussion	39
5.1	Physical Model	39
5.1.1	Mussel schematization.	39
5.2	Measurements of the steady flow	39
5.2.1	Measured drag coefficients.	40
5.2.2	EMF performance during the steady flow experiments	40
5.2.3	Performance of the force transducer during the steady flow experiments	40
5.2.4	Determination of the flow velocity.	41
5.3	Measurements on waves	41
5.3.1	Observations of the drag and inertia coefficient	41
6	Conclusion and recommendations	44
6.1	Conclusion	44
6.1.1	Sub-questions	44
6.1.2	Main research question	45
6.2	Recommendations	45
A	Mussel pattern	47
A.1	Dimensions	47
A.2	Realistic shape	48
A.3	Mussel pattern	48
A.4	Python Script	50
A.5	Verification	51
B	Instruments	52
B.1	Details on wave height meters	53
B.2	Details on electromagnetic velocity meter	55
B.3	Details on force transducer	57
B.4	Calibration of the force transducer	58
C	Wave paddle script for Cnoidal waves	59
D	Location of the cylinder	61
D.1	Required Reynolds number	61
D.2	Turbulent Boundary layer.	62
D.3	Thickness of the boundary layer	62
E	Averaging interval	63
F	Filters for the force data	64
G	Graphs of the waves	66
G.1	Smooth cylinder: $H = 4$ cm and $T = 1$ s	66
G.2	Smooth cylinder: $H = 4$ cm and $T = 2$ s	67
G.3	Smooth cylinder: $H = 4$ cm and $T = 3$ s	68
G.4	Smooth cylinder: $H = 13$ and $T = 2$ s.	69
G.5	Smooth cylinder: $H = 13$ cm and $T = 3$ s.	70
G.6	Smooth cylinder: $H = 13$ cm and $T = 6$ s.	71
G.7	Smooth cylinder: $H = 13$ cm and $T = 7$ s.	72
G.8	Mussels: $H = 6.66$ cm and $T = 1$ s	73
G.9	Mussels: $H = 6.66$ cm and $T = 2$ s	74
G.10	Mussels: $H = 6.66$ cm and $T = 3$ s	75
G.11	Mussels: $H = 21.3$ cm and $T = 1.5$ s	76
G.12	Mussels: $H = 21.3$ cm and $T = 2$ s	77
G.13	Mussels: $H = 21.3$ cm and $T = 3$ s	78
G.14	Mussels: $H = 21.3$ cm and $T = 4$ s	79
G.15	Mussels: $H = 21.3$ cm and $T = 5$ s	80
G.16	Mussels: $H = 21.3$ cm and $T = 6$ s	81
G.17	Mussels: $H = 21.3$ cm and $T = 7$ s	82
G.18	Overview	82

---

H	Velocity and acceleration profile	83
H.1	Velocity and acceleration points at the bed and surface . . . . .	83
H.2	Fitted line . . . . .	83
I	Script for Fenton	84



# List of Figures

1.1	Coastal protection services offered by a mangrove forest consist of wave attenuation, soil reinforcement and sediment trapping. (Gijón Mancheño et al., 2021b) . . . . .	2
1.2	Visual overview of the report. The pink boxes represent the chapter where a sub-research question is answered. SRQ 1 is answered in chapter 3. In chapter 4, sub-research question (SRQ) 2 and 3 are answered. Consequently, chapter 4 answers 4 and 5. . . . .	3
2.1	The top view of the flow around a cylinder explains the boundary layer separation (Groh, 2016)	4
2.2	Regimes of flow around a smooth, circular cylinder in a steady current (Sumer and Fredsoe, 1997)	5
2.3	Regimes of flow around a smooth, circular cylinder in a steady current (Sumer and Fredsoe, 1997). Measurements from Williamson (1989), Roshko (1960) and Schewe (1983). . . . .	6
2.4	Drag coefficient for a smooth cylinder as a function of Reynolds number (Sumer and Fredsoe, 1997) . . . . .	7
2.5	The total force in oscillatory flow (Sumer and Fredsoe, 1997) . . . . .	9
2.6	The drag coefficient for a smooth and rough cylinder as a function of Reynolds number. Measurements by Wieselberger for $40 < Re < 50 \times 10^5$ and Schewe (1983) for $Re > 10^5$ . The graph is of Schlichting (1955) . . . . .	10
2.7	Simplification for realistic modelling of mussels by Marty et al., 2021. $K$ represents the height of the roughness element, $S$ the height of the mussel and $l$ the width of the mussel. The numbers are typical dimensions of the research of Marty et al., 2021 . . . . .	10
2.8	$H_{m0}$ over ten years at the structures in Demak. Data of Wave Watch III. . . . .	12
2.9	The Reynolds numbers over ten years at the structures in Demak. Data of Wave Watch III. . . . .	12
2.10	The kd numbers over ten years at the structures in Demak. Data of Wave Watch III. . . . .	12
2.11	The wave direction in degrees over ten years at the structures in Demak. Data of Wave Watch III. . . . .	12
2.12	Overview of validity region of the wave theories (Le Méhauté, 1976) . . . . .	13
2.13	The overview of the wave theories with the propagated wave conditions in Demak. . . . .	13
3.1	Overview of the cylinders used during the experiments with a 2, 2.5, 4 and 5 cm diameter. The cylinders with a scaling of 1:6 are included the red rectangle and with the scaling of 1:3 in the yellow rectangle. The part of the cylinder covered by mussel rings are depicted with green squares. . . . .	15
3.2	Two structures to make the cylinder rigidly fixed. Figure (A) was used for all cylinders except for the smooth cylinder with a diameter of 2.5 cm. . . . .	16
3.3	Outline of the green Asian mussel. Region 1 is schematised as a roughness element, and region 2 is an impermeable layer. . . . .	16
3.4	The final design consists of (1) Roughness elements (2) Impermeable layer (3) Extra thickness. The 3D model is made in Fusion360 by Flip Colin . . . . .	16
3.5	Process of obtaining the spatial distribution and orientation of the mussels with the help of images from the field. . . . .	17
3.6	Overview of the physical model process with the help of a 3D model and resin casting. . . . .	18
3.7	The outline of the wave flume:(1) Wave generator,(2) Wave absorber, (3ab) Inlets, (4ab) Outlets and (5ab) Metal plates . . . . .	19
3.8	The set-up of the flume for the steady flow experiments . . . . .	22
3.9	The set-up of the flume for the oscillatory flow experiments . . . . .	22
3.10	The flow chart for the data processing of the wave experiments. With $u$ the velocity, $F$ the force and $h$ is the water depth. . . . .	24
3.11	The flow chart for the data processing of the wave experiments, since surface elevation, forces and velocities were measured at different positions along the flume. With $\eta$ representing the surface elevation, $u$ the velocity, and $F$ the force. . . . .	25
3.12	The magnitude spectrum of wave height of 13 cm and period of 7 seconds (H013T7). The vertical line represents the cut off frequency of 0.05 Hz. . . . .	26

3.13	The magnitude spectrum of wave height of 4 cm and period of 1 second (H004T1). The vertical line represents the cut off frequency of 0.05 Hz. . . . .	26
3.14	The magnitude spectrum of wave height of 21.6 cm and period of 7 seconds (H0216T7). The vertical line represents the cut off frequency of 0.05 Hz. . . . .	26
3.15	Each of the four wave gauges measured the surface elevation. Whereby, wave gauge four was positioned the closest to the wave generator . . . . .	26
3.16	The aligned surface elevation measured by each of the four wave gauges . . . . .	26
4.1	Image of the standard mussel covered cylinder . . . . .	27
4.2	Binary image for MATLAB . . . . .	27
4.3	Comparison of a 5-points velocity profile (blue crosses) to a 13-points velocity profile (orange dots). The variability in the velocity signal is depicted with error bars at each point. An exponential function is fitted to the data points of the 13-points velocity profile (dashed green line) . . . . .	28
4.4	The results for the two sets of the steady flow experiments, namely scales of 1:6 and 1:3. Figures 4.4a and 4.4b plot the measured force against the measured depth-integrated velocity. Figures 4.4c and 4.4d show the obtained drag coefficient plotted with fitting lines for smooth single cylinder by Munson et al. (1994) (dashed dark blue line) and White (1994) (dashed light blue line). Figures 4.4f and 4.4e present the lines that are fitted to the measured data points. . . . .	30
4.5	An overview of the analysis of the wave experiments. This is also the order in which the results are presented. . . . .	31
4.6	The measured (solid blue line) and the predicted (dashed orange line) surface elevations are plotted for the two wave conditions. The black line represents the $y = 0$ axis. The dashed green line is the predicted surface elevation with the measured wave height as input and is called predicted wave 2. Predicted wave 2 is used for the results. . . . .	32
4.7	Relative error $\epsilon = dH/H$ for different wave conditions, where $dH$ is the difference between the target and the measured wave condition, and $H$ is the target wave condition. . . . .	32
4.8	The surface elevation of the measured wave for two wave conditions. The dashed lines show at which relative time with respect to the wave period $T$ the velocity profiles are shown in figure 4.9 . . . . .	33
4.9	The vertical velocity and accelerations profiles at $t/T = 1/8$ and $t/T = 3/8$ of figures 4.8a and 4.8b. The points represent the mean measured velocity at $z = 0.04$ m, $z = 0.05$ m, $z = 0.10$ m, $z = 0.20$ m, $z = 0.30$ m and $z = 0.40$ m. The vertical velocity profile constructed with fitting a function through the points is presented with a pink dashed line called the fitted function. The vertical velocity profile constructed with non-linear extrapolation is presented with a grey dashed line called scaled. More information on the extrapolation of the profiles is included in appendix H. Lastly, the vertical velocity profile from Fenton is presented as a yellow dashed line. . . . .	34
4.10	The depth-integrated velocity squared and acceleration is plotted over time for both wave conditions. The solid blue line shows the measured data, the dashed yellow line presents the line constructed with fitting a function through the points, the dashed green line shows the line based on the non-linear extrapolation and the dashed red line presents the Fenton theory. . . . .	35
4.11	Drag and inertia coefficients are plotted for three different approach methods, namely the Least Squared Method with python function <code>np.linalg.lstsq</code> , the Least Squared Method with the fitted function and the Maximum Likelihood. Moreover, the obtained coefficients by using the Fenton theory are depicted. The variability of the box plots is due to the variability in the force signals. The velocity was measured at six points over the height during the experiments. Therefore, six signals of the force are measured for every wave condition. . . . .	36
4.12	The measured force signal (solid blue line) is presented with the force signal calculated with the obtained coefficients by the Least Squared Methods (dashed orange and dashed green line) and the Maximum likelihood (dashed red line). Moreover, the signal is compared to the Fenton theory (dashed grey line), solved with the Least squared method. . . . .	37
4.13	The results are plotted together with data points of Obasaju et al.(1988), Graham(1980) and Keulegan and Carpenter (1958). Moreover, a line was plotted to fit the measurements (dashed black line). The variability of the data points is due to the variability in the force measurements. . . . .	38

5.1	The EMF's velocity signal in still water at five different heights over the water depth. The signal is used as the offset for the velocity. This signal was measured on 29/10/2021. (a) presents the signal in the morning, (b) presents the signal at noon, and (c) presents the signal at the end of the day . . . . .	41
5.2	A comparison of the original output signal of the force (orange line) with the fitted sinus function (blue line). . . . .	41
5.3	The signals of wave condition H004T2. The blue line presents the measured data, the dashed orange and green lines represent the fitted function and non-linear extrapolation of the velocity profiles. The signals are compared with the Fenton theory (dashed red line). The results of the coefficients are presented with box plots. The error bars indicate the variability in the force measurements. . . . .	43
A.1	Six images of mussels. A blue outline of mussel number 1 is shown around the other five mussels to verify that the mussels have similar shape. . . . .	47
A.2	The definitions of the measured parameters. . . . .	48
A.3	Three sides of the 3D model. . . . .	48
A.4	Three images from the field. The red box defines a fixed area, where the position of the mussel are investigated. . . . .	49
A.5	Three sides of the 3D model. . . . .	49
A.6	Outcom of the python script . . . . .	51
B.1	Calibration formula measured at 23 cm from the bed . . . . .	58
B.2	Calibration formula measured at 34.5 cm from the bed . . . . .	58
B.3	Calibration formula measured at 46 cm from the bed . . . . .	58
B.4	Calibration formula measured at 72 cm from the bed . . . . .	58
D.1	Development of the boundary layer over the distance, $x$ (Munson et al., 1994) . . . . .	62
E.1	The difference in mean velocity using multiple averaging intervals. . . . .	63
F.1	The full and raw time series of the force data . . . . .	64
F.2	The zoomed in and raw time series of the force data . . . . .	64
F.3	Overview of 5 ways to filter the time series of the force data . . . . .	65
F.4	Filter based on the resonance of the cylinder . . . . .	65
F.5	3 Filter based on the peaks, through and zero-down crossing of the force data . . . . .	65
F.6	Comparison of the moving average filter, low pass filter and the zero down crossing filter . . . . .	65
G.1	The surface elevation for $H = 4$ cm and $T = 1$ sec. . . . .	66
G.2	The velocity for $H = 4$ cm and $T = 1$ sec . . . . .	66
G.3	The force on the cylinder with the fitted sinus function for $H = 4$ cm and $T = 1$ sec. . . . .	66
G.4	Surface elevation, velocity and force plotted together. . . . .	66
G.5	The measured and calculated force. . . . .	66
G.6	Drag and inertia coefficients . . . . .	66
G.7	The surface elevation for $H = 4$ cm and $T = 2$ sec. . . . .	67
G.8	The velocity for $H = 4$ cm and $T = 2$ sec . . . . .	67
G.9	The force on the cylinder with the fitted sinus function for $H = 4$ cm and $T = 2$ sec. . . . .	67
G.10	Surface elevation, velocity and force plotted together. . . . .	67
G.11	The measured and calculated force. . . . .	67
G.12	Drag and inertia coefficients . . . . .	67
G.13	The surface elevation for $H = 4$ cm and $T = 3$ sec. . . . .	68
G.14	The velocity for $H = 4$ cm and $T = 3$ sec . . . . .	68
G.15	The force on the cylinder with the fitted sinus function for $H = 4$ cm and $T = 3$ sec. . . . .	68
G.16	Surface elevation, velocity and force plotted together. . . . .	68
G.17	The measured and calculated force. . . . .	68
G.18	Drag and inertia coefficients . . . . .	68
G.19	The surface elevation for $H = 13$ cm and $T = 2$ sec. . . . .	69
G.20	The velocity for $H = 13$ cm and $T = 2$ sec. . . . .	69

G.21 The force on the cylinder with the fitted sinus function for $H = 13$ cm and $T = 2$ sec. . . . .	69
G.22 Surface elevation, velocity and force plotted together. . . . .	69
G.23 The measured and calculated force. . . . .	69
G.24 Drag and inertia coefficients . . . . .	69
G.25 The surface elevation for $H = 13$ cm and $T = 3$ sec. . . . .	70
G.26 The velocity for $H = 13$ cm and $T = 3$ sec . . . . .	70
G.27 The force on the cylinder with the fitted sinus function for $H = 13$ cm and $T = 3$ sec. . . . .	70
G.28 Surface elevation, velocity and force plotted together. . . . .	70
G.29 The measured and calculated force. . . . .	70
G.30 Drag and inertia coefficients . . . . .	70
G.31 The surface elevation for $H = 13$ cm and $T = 6$ sec. . . . .	71
G.32 The velocity for $H = 13$ cm and $T = 6$ sec . . . . .	71
G.33 The force on the cylinder with the fitted sinus function for $H = 13$ cm and $T = 6$ sec. . . . .	71
G.34 Surface elevation, velocity and force plotted together. . . . .	71
G.35 The measured and calculated force. . . . .	71
G.36 Drag and inertia coefficients . . . . .	71
G.37 The surface elevation for $H = 13$ cm and $T = 7$ sec. . . . .	72
G.38 The velocity for $H = 13$ cm and $T = 7$ sec . . . . .	72
G.39 The force on the cylinder with the fitted sinus function for $H = 13$ cm and $T = 7$ sec. . . . .	72
G.40 Surface elevation, velocity and force plotted together. . . . .	72
G.41 The measured and calculated force. . . . .	72
G.42 Drag and inertia coefficients . . . . .	72
G.43 The surface elevation for $H = 6.66$ cm and $T = 1$ sec. . . . .	73
G.44 The velocity for $H = 6.66$ cm and $T = 1$ sec . . . . .	73
G.45 The force on the cylinder with the fitted sinus function for $H = 6.66$ cm and $T = 1$ sec. . . . .	73
G.46 Surface elevation, velocity and force plotted together. . . . .	73
G.47 The measured and calculated force. . . . .	73
G.48 Drag and inertia coefficients . . . . .	73
G.49 The surface elevation for $H = 6.66$ cm and $T = 2$ sec. . . . .	74
G.50 The velocity for $H = 6.66$ cm and $T = 2$ sec . . . . .	74
G.51 The force on the cylinder with the fitted sinus function for $H = 6.66$ cm and $T = 2$ sec. . . . .	74
G.52 Surface elevation, velocity and force plotted together. . . . .	74
G.53 The measured and calculated force. . . . .	74
G.54 Drag and inertia coefficients . . . . .	74
G.55 The surface elevation for $H = 6.66$ cm and $T = 3$ sec. . . . .	75
G.56 The velocity for $H = 6.66$ cm and $T = 3$ sec. . . . .	75
G.57 The force on the cylinder with the fitted sinus function for $H = 6.66$ cm and $T = 3$ sec. . . . .	75
G.58 Surface elevation, velocity and force plotted together. . . . .	75
G.59 The measured and calculated force. . . . .	75
G.60 Drag and inertia coefficients . . . . .	75
G.61 The surface elevation for $H = 21.3$ cm and $T = 1.5$ sec. . . . .	76
G.62 The velocity for $H = 21.3$ cm and $T = 1.5$ sec. . . . .	76
G.63 The force on the cylinder with the fitted sinus function for $H = 21.3$ cm and $T = 1.5$ sec. . . . .	76
G.64 Surface elevation, velocity and force plotted together. . . . .	76
G.65 The measured and calculated force. . . . .	76
G.66 Drag and inertia coefficients . . . . .	76
G.67 The surface elevation for $H = 4$ cm and $T = 1$ sec. . . . .	77
G.68 The velocity for $H = 4$ cm and $T = 1$ sec . . . . .	77
G.69 The force on the cylinder with the fitted sinus function for $H = 4$ cm and $T = 1$ sec. . . . .	77
G.70 Surface elevation, velocity and force plotted together. . . . .	77
G.71 The measured and calculated force. . . . .	77
G.72 Drag and inertia coefficients . . . . .	77
G.73 The surface elevation for $H = 4$ cm and $T = 1$ sec. . . . .	78
G.74 The velocity for $H = 4$ cm and $T = 1$ sec . . . . .	78
G.75 The force on the cylinder with the fitted sinus function for $H = 4$ cm and $T = 1$ sec. . . . .	78
G.76 Surface elevation, velocity and force plotted together. . . . .	78

G.77 The measured and calculated force. . . . .	78
G.78 Drag and inertia coefficients . . . . .	78
G.79 The surface elevation for H = 21.3 cm and T = 4 sec. . . . .	79
G.80 The velocity for H = 21.3 cm and T = 4 sec. . . . .	79
G.81 The force on the cylinder with the fitted sinus function for H = 21.3 cm and T = 4 sec. . . . .	79
G.82 Surface elevation, velocity and force plotted together. . . . .	79
G.83 The measured and calculated force. . . . .	79
G.84 Drag and inertia coefficients . . . . .	79
G.85 The surface elevation for H = 21.3 cm and T = 5 sec. . . . .	80
G.86 The velocity for H = 21.3 and T = 5 sec . . . . .	80
G.87 The force on the cylinder with the fitted sinus function for H = 21.3 and T = 5 sec. . . . .	80
G.88 Surface elevation, velocity and force plotted together. . . . .	80
G.89 The measured and calculated force. . . . .	80
G.90 Drag and inertia coefficients . . . . .	80
G.91 The surface elevation for H = 4 cm T = 6 sec 85 . . . . .	81
G.92 The velocity for H = 4 cm and T = 6 sec . . . . .	81
G.93 The force on the cylinder with the fitted sinus function for H = 4 cm and T = 1 sec. . . . .	81
G.94 Surface elevation, velocity and force plotted together. . . . .	81
G.95 The measured and calculated force. . . . .	81
G.96 Drag and inertia coefficients . . . . .	81
G.97 The surface elevation for H = 4 cm and T = 7 sec. . . . .	82
G.98 The velocity for H = 4 cm and T = 7 sec . . . . .	82
G.99 The force on the cylinder with the fitted sinus function for H = 4 cm and T = 1 sec. . . . .	82
G.100 Surface elevation, velocity and force plotted together. . . . .	82
G.101 The measured and calculated force. . . . .	82
G.102 Drag and inertia coefficients . . . . .	82
G.103 Drag coefficient . . . . .	82
G.104 Inertia coefficient . . . . .	82

# List of Tables

2.1	Empirical relationships between the drag coefficient and the Reynolds number for smooth vertical cylinders. . . . .	8
2.2	Drag and inertia coefficients for marine growth from literature . . . . .	11
3.1	The average dimension of the green Asian mussel . . . . .	16
3.2	The details on the final design of the mussel rings. The relative roughness ( $e$ ) is calculated by dividing the roughness height by 2*superimposed layer + 2* extra layer thickness + the inner diameter. . . . .	17
3.3	A rough estimation of the flow velocity that needs to be reached to obtain $Re = 10^3-10^4$ is calculated with the outer diameter. The steady flow is generated by manually adjusting a pump and it is not possible to set the flow to a certain velocity. Therefore a rough estimation was made to create a range of flow velocities. . . . .	20
3.4	The tested wave conditions . . . . .	21
3.5	The effect of the cut-off frequency on the variance for the different instruments and different wave conditions. . . . .	26
4.1	Determination of equivalent diameter for the standard mussel . . . . .	27
4.2	The equivalent diameters of the three mussel covered cylinders . . . . .	28
4.3	The depth-integrated velocity and velocity squared are presented for the velocity profiles and the fitted functions. The mean depth-integrated velocity ( $\overline{U}$ ) and velocity squared ( $\overline{U^2}$ ) are compared to the square root of the mean of the values ( $U_{RMS}$ and $U_{RMS}^2$ ) to approach the $\int u dz [m/s]$ and $\int u^2 dz [(m/s)^2]$ of the fitted function. . . . .	29
4.4	The values of the drag coefficients of the fitted lines for the tested cylinders. S1:6 is the smooth cylinder for a scale of 1:6, ES1:6 is the smooth cylinder with an equivalent diameter as S1:6, SM is the Standard Mussel, S1:3 is the smooth cylinder for a scale of 1:3, MM is the half-grown mussel, and LM is the fully grown mussel. . . . .	29
4.5	The parameters $a$ , $b$ and $c$ for the fitted function based on the model function by White (2006): $C_d = a+b*Re^c$ . . . . .	29
A.1	Averaged dimensions in the field in cm . . . . .	48
A.2	Analysis of the simplified patterns. Version A is figure A.5a, version B is figure A.5b, version C is figure A.5c and version D is figure A.5d . . . . .	50

# Nomenclature

	Difference between the target and the measured wave conditions [-]
$f_v$	Vortex shedding frequency [Hz]
$\nu$	Kinematic viscosity [Pa*s]
$\epsilon$	Relative error [-]
$\eta_{WG}$	Surface elevation measured by the wave gauge [m]
$\frac{\partial u}{\partial t}$	Flow acceleration [m/s <sup>2</sup> ]
$\lambda$	Wavelength [m]
$\bar{F}_f$	Friction force [N]
$\bar{F}_p$	Pressure force [N]
$\overline{U_{RMS}}$	Root means square velocity [m/s]
$\bar{U}$	Mean velocity [m/s]
$\phi$	Location along the perimeter [rad]
$\rho_w$	Density of water [kg/m <sup>3</sup> ]
$\tau_0$	Wall shear stress [N/m <sup>2</sup> ]
$A$	Cross-sectional Area [m <sup>2</sup> ]
$a_w$	Wave amplitude [m]
$A_{blackpixels}$	Cross-sectional Area of black pixels [m <sup>2</sup> ]
$C_d$	Drag coefficient [-]
$C_M$	Inertia coefficient [-]
$C_m$	Hydrodynamic mass coefficient [-]
$C_{d,ES1:6}$	Drag coefficient for smooth cylinder with an equivalent diameter for a scale of 1:6
$C_{d,LM}$	Drag coefficient for large mussels [-]
$C_{d,MM}$	Drag coefficient for medium mussels [-]
$C_{d,S1:3}$	Drag coefficient for smooth cylinder for a scale of 1:3 [-]
$C_{d,S1:6}$	Drag coefficient for smooth cylinder for a scale of 1:6 [-]
$C_{d,SM}$	Drag coefficient for a standard mussels [-]
$D$	Diameter [m]
$D_o$	Outer Diameter [m]
$D_{eq}$	Equivalent Diameter [m]
$dt$	Time step [s]

---

$F$	In-line force [N]
$F_d$	Drag force [N]
$F_{FT}$	Force measured by the force transducer [N]
$Fr$	Froude number [-]
$H$	Wave height [m]
$h$	Water depth [m]
$K$	Roughness height [m]
$KC$	Keulegan-Carpenter number [-]
$kd$	Wavenumber times the depth [-]
$L$	Characteristic length [m]
$l$	Width of the mussel [m]
$L_{shell}$	Length of the shell [m]
$n$	Scaling factor [-]
$r_0$	Radius of the cylinder [m]
$Re$	Reynolds number [-]
$S$	Height of the mussel [m]
$St$	Strouhall number [-]
$t$	Time [s]
$T_w$	Wave period [s]
$U$	Flow velocity [m/s]
$U_m$	Maximum flow velocity [m/s]
$U_{da}$	Depth averaged velocity [m/s]
$U_{EMF}$	Velocity measured by EMF [m/s]
$U_{Ursell}$	Ursell number [-]
$X$	Position of the wave paddle [m]



# 1

## Introduction

### 1.1. Problem indication

Since 2013, a public-private partnership coordinated by EcoShape has been working on rehabilitating the coast at Demak (Wilms et al., 2019). Demak is a district on the northern coast of Java consisting of muddy shores. Mangroves largely covered the coastal region of the district by the 1800s, but they were almost deforested for shrimp farming during the 20th century. Mangrove forests provide coastal protection due to their ability to attenuate waves and trap sediment (van Wesenbeeck et al., 2015), illustrated in Figure 1.1. However, in combination with subsidence rates up to 16 cm/year due to groundwater extraction, mangrove loss has resulted in severe erosion (Winterwerp et al., 2020). Besides the conversion to ponds and land subsidence, erosion is also caused by river canalization, coastal infrastructure construction, and the use of mangroves for timber. Unfortunately, Demak is not an isolated case, and mangroves-coasts all over the world are eroding due to deforestation. With climate change and rising sea levels, protecting the coastal areas from natural hazards becomes increasingly important (Wilms et al., 2019).

Mangroves have been planted in areas where natural forests have been either removed or damaged, but these effects have not always been successful. Planting efforts failed due to not correctly understanding the system and using inappropriate species and sites (Lewis, 2001; Primavera and Esteban, 2008). The lessons learned are that successful rehabilitation of mangroves is a combination of understanding the ecological system, patience and persistence, and involvement of the local communities (Winterwerp et al., 2020). Involvement of the local communities is vital as socio-economic incentives from activities such as aquaculture threaten the forest. In addition, by restoring the mangroves, there will be an inevitable loss of intensive aquacultures (Winterwerp et al., 2005). Therefore, it is vital to have an alternative that does not harm the mangroves to ensure them long-term and give the local community an economic incentive to sustain them (van Wesenbeeck et al., 2015).

In Demak, a Building with Nature approach was chosen for the muddy coasts to counteract erosion, rehabilitating the mangroves instead of constructing conventional hard structures. Mangrove deforestation disturbed the sediment balance, causing steeper slopes on the foreshore. Permeable dams of bamboo and brushwood were constructed to restore this balance (Winterwerp et al., 2020). The dams attenuated wave energy while also allowing the sediment influx by the tide. Hence, creating milder slopes and giving mangroves a calm environment to naturally expand. The pilot structures, built in 2013, showed a significant bed level rise and expansion of the mangroves after the construction. Unfortunately, juvenile mangroves did not survive, likely due to the high subsidence rates of the area. Despite this, permeable dams were applied to more locations (Winterwerp et al., 2020).

Recent research by Gijón Mancheño et al. (2021a) found that rows of bamboo could be used as an alternative to the brushwood. The conventional brushwood dams could be replaced by vertical poles, which resemble the bamboo poles used for mussel aquaculture (NWO et al., 2017). Subsequently, a new project called MuMaCo (Mussels as Mangrove facilitators for Coastal defence) was launched in Demak, integrating mussel aquaculture into the mangrove rehabilitation project. Mussel aquaculture is a mangrove-friendly alternative to shrimp farming, because it does not need building ponds, and it can take place in shallow marine areas (Rejeki et al., 2021). The green Asian mussels, *Perna Viridis*, have already been grown at vertical poles in Demak, and it is thus chosen as the species to be locally produced. The expectation is that the added

roughness and diameter of the mussels will increase the wave dissipation. The proposed structures consist of vertical piles with a diameter of 15 cm and the poles will have a 25-30 cm diameter when covered. This will be the first coastal defence line, as it is needed to be combined with other structures.

The waves in Demak are non-linear waves and fall in a cnoidal regime (Haage, 2018, Jansen, 2019). Waves can be grouped in oscillatory flow regimes by the Keulegan-Carpenter ( $KC$ ) number. For drag dominated waves ( $KC > 30$ ) waves, the drag crisis can decrease the effect of mussel growth for specific Reynolds ( $Re$ ) numbers (Sumer and Fredsoe, 1997). This is not beneficial for the wave damping properties of the structures. Therefore, research is required on which  $Re$  numbers are in the drag crisis, as this is not yet done for mussel roughness.

The effect of mussels on poles is not as explored as mussels on longlines (Gieschen et al., 2021; Landmann et al., 2019) and the seabed (Donker et al., 2013). It was confirmed that for seabed with mussels, the increase of roughness indeed increases wave attenuation (Donker et al., 2013). Little is known regarding the wave damping properties of mussel covered vertical poles. To facilitate the design of the structures, this study aims to quantify the interaction between the poles and waves.

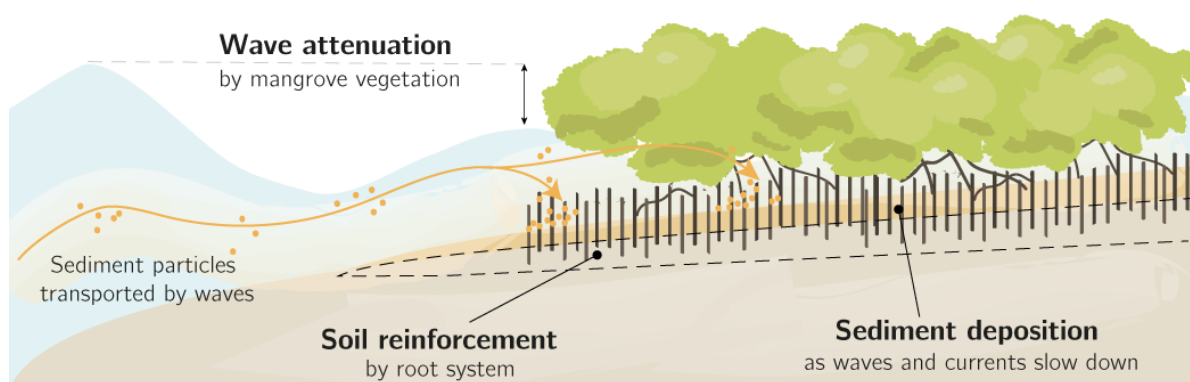


Figure 1.1: Coastal protection services offered by a mangrove forest consist of wave attenuation, soil reinforcement and sediment trapping. (Gijón Mancheño et al., 2021b)

## 1.2. Objective and research questions

The objective of this thesis is to investigate the effect of mussel growth on wave attenuation by vertical poles. The main research question of the thesis is:

How does the growth of the mussel, *Perna Viridis*, on vertical bamboo poles affect the physical processes driving wave dissipation for different wave conditions?

Furthermore, the sub research questions are:

1. How can mussels in small-scale experiments be schematized?
2. What is the effect of mussels on the hydrodynamic forces of a vertical pole in a current?
3. Is the drag crisis likely to be relevant for poles with mussels in the field?
4. What is the effect of mussel on the hydrodynamic forces of a vertical pole in waves?
5. Can the drag coefficient of cnoidal waves be linked to the Keulegan-Carpenter number, as it is done for the linear waves?

## 1.3. Research approach and thesis outline

With the complex geometry of mussel covered poles subjected to currents and waves in shallow conditions, there is a need for experimental data to validate numerical models eventually. Therefore, it is chosen to

produce data for currents and waves in a laboratory test using down-scaled models of the poles. Experiments for single cylinders and mussel-covered cylinder are performed in the Hydraulic Engineering laboratory of the Delft University Technology.

This thesis consists of a literature study and an experimental study. Chapter 2 describes the theoretical background and the relevant literature for this thesis. It discusses the physical processes driving wave dissipation and performed research on the effect of mussels growth. Next, in chapter 3, the design of the physical model is presented and the laboratory experiments for the steady flow and waves are discussed. Each component of the physical model is explained and it is shown how the physical model is constructed. The second part of chapter 3 describes how the data is processed. Then chapter 4 shows the results of the experiments. Lastly, chapter 5 and 6 present the discussion, conclusion and recommendation.

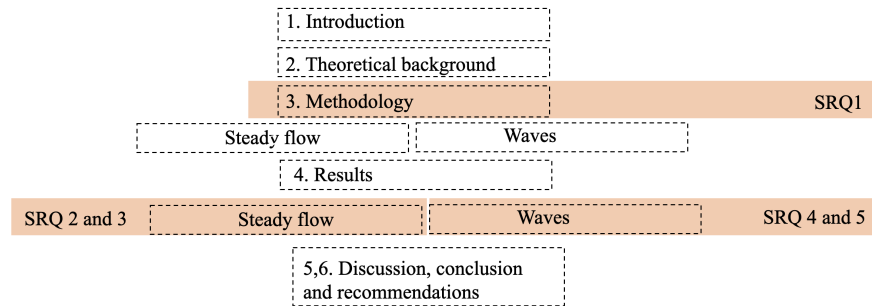


Figure 1.2: Visual overview of the report. The pink boxes represent the chapter where a sub-research question is answered. SRQ 1 is answered in chapter 3. In chapter 4, sub-research question (SRQ) 2 and 3 are answered. Consequently, chapter 4 answers 4 and 5.

# 2

## Theoretical background

*This chapter describes the fundamentals of the interaction between a single vertical cylinder and its surrounding flow. Firstly, the flow and hydrodynamic forces acting on a cylinder in a steady flow are explained. Next, the same is done for the cylinder in an oscillatory flow. Hereafter, the effect of roughness elements on the flow and forces is discussed. This is followed by a section reflecting the mussels as roughness elements. At last, all of the information gathered is applied to the situation in Demak. The section below describes the behaviour of smooth cylinder, unless when indicated otherwise.*

### 2.1. Steady flow around a cylinder

The presence of a cylinder in a current results in the formation of a boundary layer along the surface of the cylinder. Through this layer, the flow velocity reduces from its undisturbed value to zero at the solid surface. The flow characteristics at the boundary layer depend on the cylinder diameter and the flow velocity. This dependency is usually represented using the dimensionless Reynolds numbers:

$$Re = UD/\nu \quad (2.1)$$

Where  $U$  is the flow velocity,  $D$  is the diameter and  $\nu$  is the kinematic viscosity.  $Re$  represents the ratio of inertial forces to viscous forces. The viscous force is the resistance of molecules on the surface of the cylinder sticking to each other, while the kinetic force is the force due to the momentum of the flow. The viscous forces are dominant for low Reynolds numbers, affecting a large area around the cylinder. However, when the Reynolds number increases, the inertial forces become dominant. The viscous layer becomes thinner and the boundary layer that develops along the perimeter tends to detach forming a turbulent wake.

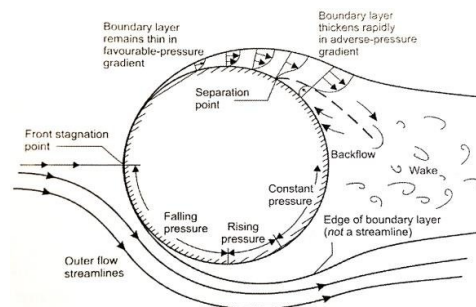


Figure 2.1: The top view of the flow around a cylinder explains the boundary layer separation (Groh, 2016)

The development of the boundary layer is essential for vortex-shedding, and the process is described in the figure 2.1.

As the flow approaches the cylinder, it is stopped at the stagnation point, where it results in a locally increased pressure. The Bernoulli equations state that the pressure decreases when the fluid accelerates. Fluids flow are generally driven by a negative pressure gradient. At the side of the cylinder, the velocity is at

its maximum, and the flow slows down again, creating a positive pressure gradient, and the velocity gradient reacts adversely. For circular cylinder at  $Re < 5$ , the flow can overcome the negative velocity gradient and follows the cylinder's shape. However, the velocity gradient becomes so large for higher Reynolds numbers that the flow velocity at a point (the separation point) becomes zero. Beyond this point, the flow separates, and a re-circulation region is formed. For  $Re > 5$ , the vorticity in the boundary layer transforms the shear layer into a vortex at both sides of the cylinder. This happens on both sides of the cylinder. For  $Re > 40$ , the vortices become unstable and interact with each other and start shedding.


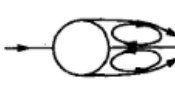


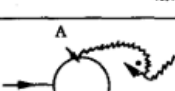
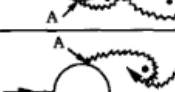
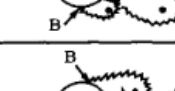
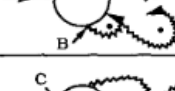

a)		No separation. Creeping flow	$Re < 5$
b)		A fixed pair of symmetric vortices	$5 < Re < 40$
c)		Laminar vortex street	$40 < Re < 200$
d)		Transition to turbulence in the wake	$200 < Re < 300$
e)		Wake completely turbulent. A: Laminar boundary layer separation	$300 < Re < 3 \times 10^5$  Subcritical
f)		A: Laminar boundary layer separation B: Turbulent boundary layer separation; but boundary layer laminar	$3 \times 10^5 < Re < 3.5 \times 10^5$ Critical (Lower transition)
g)		B: Turbulent boundary layer separation; the boundary layer partly laminar partly turbulent	$3.5 \times 10^5 < Re < 1.5 \times 10^6$ Supercritical
h)		C: Boundary layer com- pletely turbulent at one side	$1.5 \times 10^6 < Re < 4 \times 10^6$ Upper transition
i)		C: Boundary layer com- pletely turbulent at two sides	$4 \times 10^6 < Re$ Transcritical

Figure 2.2: Regimes of flow around a smooth, circular cylinder in a steady current (Sumer and Fredsoe, 1997)

Figure 2.2 displays the different regimes for cylinders with the corresponding numbers and terminology. The shifting of the separation point to the rear side of the cylinder occurs when the boundary layer turns turbulent for  $3.0 \times 10^5 < Re < 3.5 \times 10^5$ . As a result, the vortices will interact over a smaller distance, producing a smaller wake. The next section explains the consequence of this shift on the forces.

The vortex shedding frequency can also be used to characterise the flow regime, and it is expressed using the Strouhall number:

$$St = \frac{f_v D}{U} \tag{2.2}$$

Where  $St$  is the Strouhall number [-] and  $f_v$  is the vortex shedding frequency in Hz. In figure 2.3, the influence

of a smaller wake can be seen as the Strouhall number jumps from 0.2 to 0.45 with the Reynolds number increasing above  $3 \times 10^5$ .

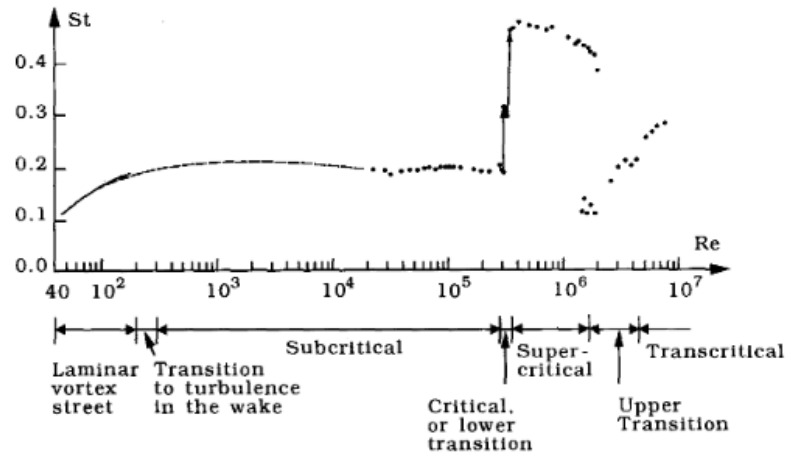


Figure 2.3: Regimes of flow around a smooth, circular cylinder in a steady current (Sumer and Fredsoe, 1997). Measurements from Williamson (1989), Roshko (1960) and Schewe (1983).

Lastly, the same flow regimes can occur at different Reynolds numbers. This depends on whether the cylinder has a rough or smooth surface or if the incoming flow is already turbulent upstream from the cylinder. Moreover, the shape of the emergence of an object has a significant influence on the hydrodynamics of the flow.

In the thesis, experiments are aimed to be in the sub-critical regime (i.e. for  $300 < Re < 3 * 10^5$ , see figure 2.2), as these are the conditions experienced by the structures in Demak. Thus the wake is fully turbulent, but the boundary remains laminar, and the position of the separation point will be between the front and rear sides of the cylinder. Therefore the wake will be relatively large.

## 2.2. Forces on a cylinder in a steady flow

The most important forces that act on a cylinder in a steady flow are the lift force and the drag force. The lift force is defined as the force perpendicular to the mean flow direction and points sideways for vertical cylinders submerged in a horizontal flow. The lift force is generated in case there is a steady flow gradient. The drag force acts in the direction of the flow, and it is a combination of the form drag due to the pressure, and the friction drag, due to the wall shear stress. This is described with the following equation:

$$\overline{F}_d = \overline{F}_p + \overline{F}_f = \int_0^{2\pi} \overline{p} \cos(\phi) r_0 d\phi + \int_0^{2\pi} \overline{\tau}_0 \sin(\phi) r_0 d\phi \quad (2.3)$$

Where  $\overline{F}_p$  is the pressure force,  $\overline{F}_f$  is the friction force,  $r_0$  the radius of the cylinder,  $\phi$  the location along the perimeter and  $\tau_0$  the wall shear stress. The equation 2.3 makes it clear that the drag force changes along the perimeter and that the force due to pressure and shear has a phase difference of 90 degrees. However, the friction is often neglected for  $Re > 10^4$  because it is a small part of the total drag force.

Equation 2.3 can be rewritten into equation 2.4, and with this step, the empirical non-dimensional drag coefficient is obtained.

$$\overline{C}_d = \frac{\overline{F}_d}{\frac{1}{2} \rho_w A U^2} \quad (2.4)$$

Where  $A$  is the cross-sectional area of a cylinder and  $\rho_w$  the density of water. The drag coefficient is a function of the Reynolds number, as shown in figure 2.4. The drag coefficient decreases with the increasing Reynolds number, until it stabilizes at a value of  $C_d = 1$  for  $Re = 1000$ . However, a sudden dip in the drag coefficient for  $3.5 * 10^5 < Re < 1.5 * 10^6$  is noticed. The sudden dip is the drag coefficient crisis and corresponds with the earlier mentioned shifting of the separation point. The flow restores for higher Reynolds numbers, and the wake slowly increases. This increases the drag coefficient. This critical moment covers a small region but has a large effect on the resistance of a vertical pole in the flow.

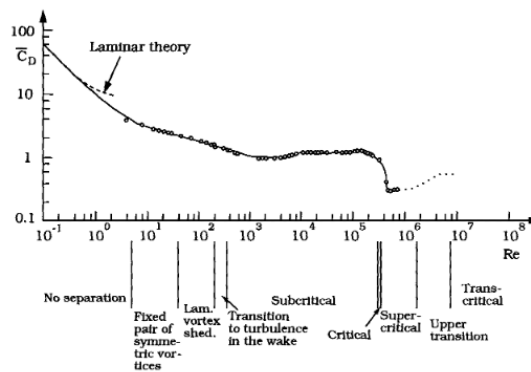


Figure 2.4: Drag coefficient for a smooth cylinder as a function of Reynolds number (Sumer and Fredsoe, 1997)

The drag coefficient can thus be obtained using equation 2.4 with force and velocity measurements. Consequently, multiple researchers fitted empirical functions through their experimentally found drag coefficients. Several empirical equations for a single smooth cylinder for  $Re < 10^5$  are summarized in the table 2.1.

Table 2.1: Empirical relationships between the drag coefficient and the Reynolds number for smooth vertical cylinders.

Author	equation for $C_d$
White, (1994)	$C_d = 1 + 10.0Re^{-0.5}$
Munson et al.(1994)	$C_d = \frac{5.93}{\sqrt{(Re)}} + 1.17$
Ameryoun et al.(1994)	$C_d = 0.7152 + \frac{-2.9 * 10^{-4}}{\frac{k}{Re} + 4.12 * 10^{-4}}$

### 2.3. Forces on a cylinder in oscillatory motion

The force in the in-line direction of an oscillatory motion is often described with the Morison equation. For a stationary cylinder in oscillatory flow, the total force has two additional components associated with the flow acceleration. These are the hydrodynamic-mass force and the Froude-Krylov force, whereby the hydrodynamic-mass force represents the force experienced by the cylinder to accelerate the surrounding fluid (Sumer and Fredsoe, 1997). Additionally, the Froude Krylov is an extra force due to the pressure gradient coming from the acceleration. The total force can thus be described as (Morison et al., 1950):

$$F = \frac{1}{2}\rho C_d D U |U| + \rho C_m A \frac{\partial U}{\partial t} + \rho A \frac{\partial u}{\partial t} \quad (2.5)$$

where  $F$  is the in-line force,  $C_m$  is the hydrodynamic mass coefficient,  $\frac{\partial u}{\partial t}$  is the flow acceleration and the additional forces are in the same order as named before.

The total in-line force can rewrite into the following often-used equation:

$$F = \int_{-h}^{\eta} \left( \frac{1}{2}\rho C_d D U |U| + \rho C_M \frac{\pi D^2}{4} \frac{\partial U}{\partial t} dz \right) \quad (2.6)$$

Where  $h$  is the water depth,  $\eta$  is the surface elevation,  $C_M = C_m + 1$  is the inertia coefficient and the  $z$  the height over the water column. The hydrodynamic-mass and Froude-Krylov components are grouped using the inertia coefficient.

From equation 2.6 and figure 2.5, it can be seen that the inertia and drag forces are not in phase. However, the phase difference between the velocity and the force will vary depending on the wave conditions, and on the relative magnitude of the inertia and drag components. For many researchers, the aim is to see the maximum force on a cylinder to estimate the stability of structures.

In literature, it can be seen that there is a large scatter in determining the coefficients (Wolfram and Naghipour, 1999, Journée and Massie, 2001). Wolfram discussed different methods to determine the  $C_d$  and  $C_M$ . By comparing eight methods based on time-domain and frequency domain techniques, he suggests to use the least square method was the best (Wolfram and Naghipour, 1999). With this method, the coefficients were determined on the principle that the mean-squared difference between the measured data and the Morison equation is as small as possible.

### 2.4. Flow around a cylinder in oscillatory flow

In wave, the wake development depends on how long the wave excursion is compared to the cylinder's size. The Keulegan-Carpenter number ( $KC$  number) groups oscillatory flow regimes similar to the Reynolds number. However, although  $KC$  influences the flow regimes in wave flows, the forces acting on the cylinder also remain dependent on  $Re$ . The  $KC$  number is described as:

$$KC = \frac{U_m T_w}{D} \quad (2.7)$$

$U_m$  is the maximum velocity and  $T_w$  is the wave period. The  $KC$  number describes the ratio of drag and acceleration forces assuming that the acceleration is  $U/T$ . For low  $KC$  numbers, the orbital motion of water is small compared to the diameter, and inertial effects are more important than the drag component of the force. However, for high  $KC$  numbers, the orbital excursion is much larger than the cylinder diameter, and the drag forces dominate the total force. The flow regimes also depend on the Reynolds number, so the  $KC$  regimes are not fixed.



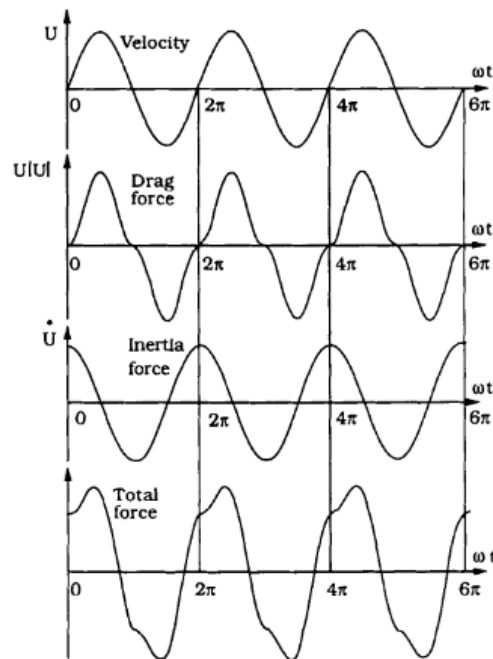


Figure 4.5 Time variation regarding the drag- and the inertia force in oscillatory flows.

Figure 2.5: The total force in oscillatory flow (Sumer and Fredsoe, 1997)

More vortices are shed for higher  $KC$  numbers. In oscillatory flows, the flow reverses and vortices are shed every half cycle. The first regime is called the single pair regime, and it sheds in the direction perpendicular to the flow. Every following regime has an extra pair of vortices. Thus, naturally, the second regime is called the double-pair regime. However, it now sheds only a 45-degree angle to the flow direction. Subsequently, the next regime is the three-pair regime and so on. Thus, the higher the  $KC$  number, the more vortices the flow shed.

This thesis investigates with a broad range of  $KC$  numbers 3 – 113, to capture the complete transition between inertia and drag dominated conditions. This should give more information on how the drag coefficients also behave in the drag dominated regimes.

## 2.5. The effect of roughness elements

Roughness elements on the surface of the cylinder affect the flow regime and, consequently, the forces on the cylinder. In figure 2.6, a smooth cylinder is compared to a rough cylinder for a steady flow. Higher roughness results in more significant drag coefficients and a shift of the drag coefficient crisis towards lower Reynolds numbers. The added roughness causes an earlier transition to a turbulent boundary layer and a smaller angular location of the separation. Therefore, the wake is also more extensive than for a smooth cylinder, so the dip in the drag coefficient is less deep.

For the oscillatory motion,  $C_M$  does not increase with increasing roughness. Sarpkaya (1977) concluded from comparing different research that not at every Reynolds number, the effect of roughness can be seen on the drag and flow characteristics. Moreover, the drag coefficient for oscillatory motion is higher than for steady flow (Marty et al., 2021; Sarpkaya, 1977).

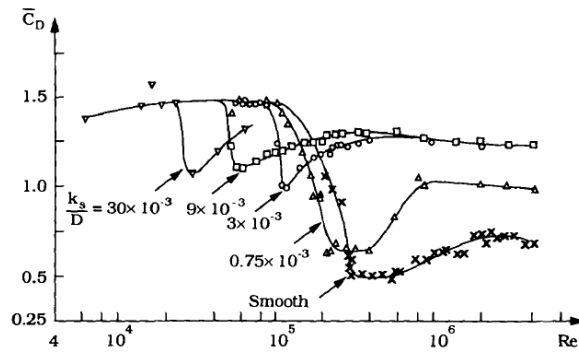


Figure 2.6: The drag coefficient for a smooth and rough cylinder as a function of Reynolds number. Measurements by Wieselberger for  $40 < Re < 50 \times 10^5$  and Schewe (1983) for  $Re > 10^5$ . The graph is of Schlichting (1955)

In literature, larger roughness elements than in figure 2.4 can be seen in marine growth applied to offshore structures (Ameryoun et al., 2019; Marty et al., 2021; Page and Hubbard, 1987). Natural roughness elements can be schematized in different ways. For example, Wolfram and Naghipour schematized marine growth as pyramids. Marty et al. (2021) used a more realistic model. An interesting simplification they used for their realistic modelling is that the lower part of the mussel can be modelled as a closed surface, as the mussels create a compact superimposed layer (Marty et al., 2021). Moreover, they concluded that most hydrodynamical tests over-simplify the shape of marine growth, and when it is more realistic, the exact shape is not well documented. Therefore, they insist that future research precisely document the relative roughness, shape, organization, and areal density.

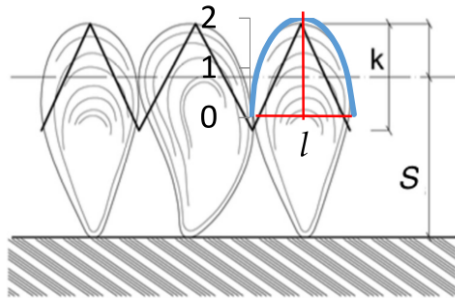


Figure 2.7: Simplification for realistic modelling of mussels by Marty et al., 2021.  $K$  represents the height of the roughness element,  $S$  the height of the mussel and  $l$  the width of the mussel. The numbers are typical dimensions of the research of Marty et al., 2021

Table 2.2 summarizes the drag coefficient from the literature.

Author	Marty et al., 2021	Marty et al., 2021	Wolfram and Naghipour, 1999	Wolfram and Naghipour, 1999	Nath, 1982
Flow	Steady flow	Waves	Waves	Waves	Waves
Roughness shape	Realistic	Realistic	Pyramids	Pyramids	Cones
Relative roughness	0.091 and 0.136	0.091 and 0.136	0.038	0.038	0.1
Conditions	$10^4 < Re < 3 * 10^5$	$KC = 3$	$KC = 0.2-17.5$	$KC = 0.4-37.9$	$KC=5$ and $KC = 12$
$C_d$	1.05 and 1.2	1.3 and 2.1	1.88	1.95	Unknown
$C_M$	N/A	1.4 and 1	2.08	1.91	2.8 and 2.5

Table 2.2: Drag and inertia coefficients for marine growth from literature

In summary, roughness causes a larger drag coefficient for an oscillation motion. However, the previous studies covered relative roughness which were much smaller compared to the situation of Demak or covered limited  $KC$  range. Thus, the effect of growing mussels on the bamboo poles cannot solely be predicted based on the conditions stated in the literature. Therefore, experiments are needed with the accurate relative roughness, namely of the green Asian mussel on bamboo poles, for a large range of  $KC$  numbers.

## 2.6. Waves and wave conditions in Demak

Alferink (2022), showed that the data of Wave Watch II agrees with offshore measurements collected by a buoy in Demak. Here, the Wave Watch III measurements are propagated with shoaling and refraction until a water depth of 1.5 m, in order to estimate the flow characteristics at the potential location of a structured with mussels. The buoy is located 5.5 km from the coast at a water depth of 12 meters. The waves are propagated to the water depth at the structures using shoaling and breaking. Figure 2.8 shows the significant wave heights at the structure during ten years. The breaking of the waves limits the wave height. Therefore, the most significant wave height will be 1.2 meters at a water depth of 1.5 m. It becomes clear that the most extreme wave heights can be seen from November until April. This coincides with the rainy season, monsoon, between December and April on the north side of Java. Figure 2.9 shows the Reynolds numbers that are seen in the area. They range from zero to 20 000. Lastly, figure 2.11 shows the  $kd$  number, which is the wave number times the water depth. The  $kd$  numbers define the different water regions. It becomes clear that the numbers vary around 0.5 and 2. This means that the waves are in an intermediate regime.

In figure 2.13 the  $KC$  numbers are plotted with the wave theories. Figure 2.12 makes clear that the waves are primarily situated in a regime with cnoidal waves.

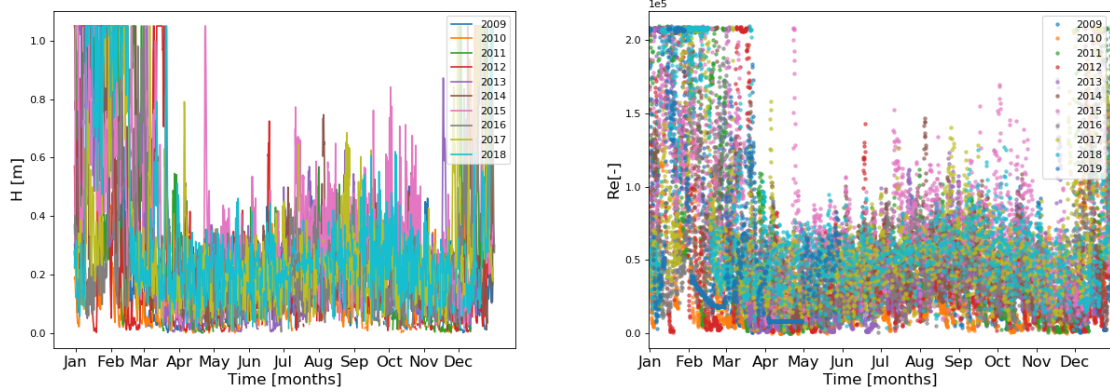


Figure 2.8:  $H_{m0}$  over ten years at the structures in Demak. Data of Wave Watch III.

Figure 2.9: The Reynolds numbers over ten years at the structures in Demak. Data of Wave Watch III.

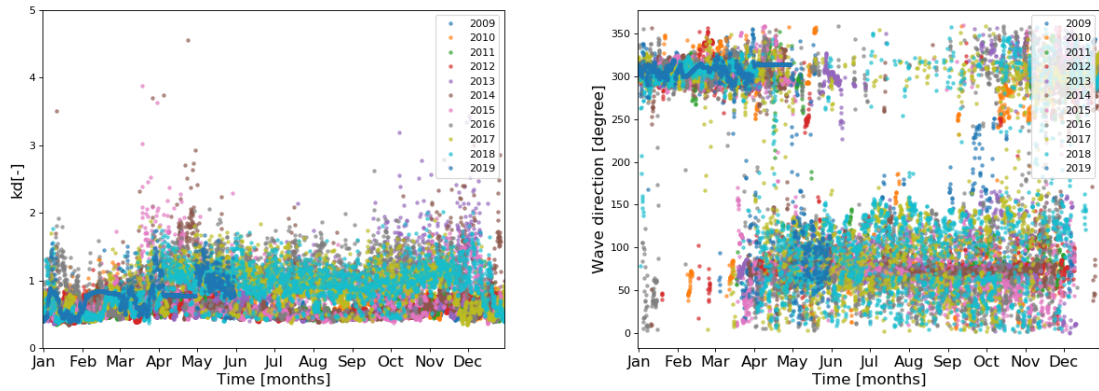


Figure 2.10: The  $kd$  numbers over ten years at the structures in Demak. Data of Wave Watch III.

Figure 2.11: The wave direction in degrees over ten years at the structures in Demak. Data of Wave Watch III.

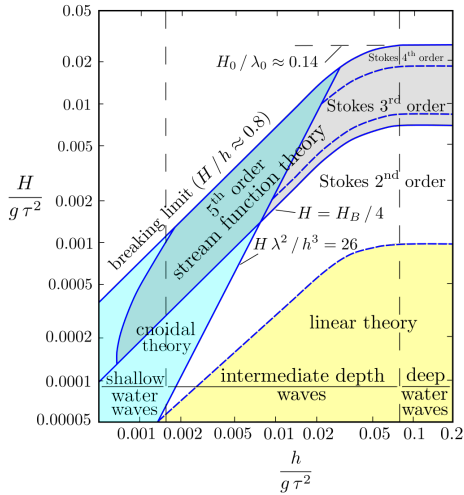


Figure 2.12: Overview of validity region of the wave theories (Le Méhauté, 1976)

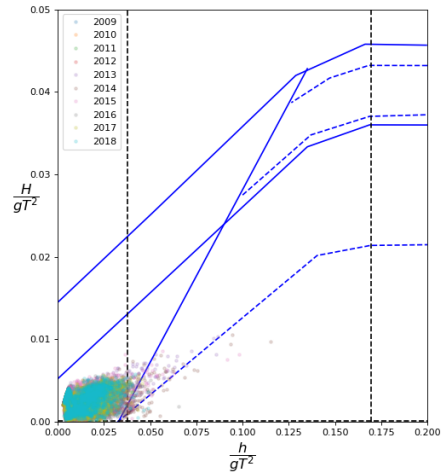


Figure 2.13: The overview of the wave theories with the propagated wave conditions in Demak.

## 2.7. Cnoidal waves

Cnoidal waves are characterized by sharp wave crests and shallow troughs. Therefore, the waves are non-linear and can not be approached with linear wave theory. Theories by Stokes (1847), Dean (1965) and Korteweg and the Vries (KdV) (1895) deal with non-harmonic waves. Theories by Stokes and Dean approximated these waves by adding high-order harmonics to a harmonic wave in successive and simultaneously order, respectively, including corrections dependent on the wave steepness. However, these theories are only applicable in deeper waters. Moreover, Fourier approximations methods, used by Dean, to approach the wave shape require computationally-expensive matrix techniques (Fenton, 1999). The Kortweg and the Vries, also called the cnoidal theory, is applicable for waves in shallow water. It is similar to the previous theories, however the basis of the KdV theory is a cnoidal wave and the corrections are applied to account for finite-depth effects (Holthuijsen, 2007). Stokes, Dean and cnoidal wave theories are thus not accurate for all waves. Fenton reviewed the existing theories and found an approach that was applicable over a wide range of waves. Instead of expressing the series for velocity in terms of relative wave height, it was expressed in terms of shallowness (Fenton, 1999) and the approach used a fifth order solution.

The Ursell number classifies how non-linear a wave is and is expressed with the following equation:

$$U_{Ursell} = H\lambda^2/h^3 \tag{2.8}$$

Where  $H$  is the wave height and  $\lambda$  is the wavelength.

The Ursell number also gives conditions as to which theory is applicable for the wave. For example, if  $N_{Ursell} > 26$  the cnoidal theory is best applicable and for  $N_{Ursell} < 10$  the theory of Stokes (Holthuijsen, 2007).

# 3

## Methodology

*An experimental study was done on how the growth of the mussel, Perna Viridis, on vertical bamboo poles affects physical processes that influence wave dissipation for various wave conditions. Single smooth cylinders were compared to various single cylinders covered with 3D-printed semi-circular shells with mussels for a steady flow and waves. The laboratory set-up and data processing are described below.*

### 3.1. Physical model

Each component of the physical model is discussed in this section. First, the laboratory model was scaled so that the physical processes in the field and the experiments are comparable. The scaling followed the rules presented in Section 3.1.1. Next, the construction of the physical model and its implementation in the flume is shown in Section 3.1.2. Then, the concept of representing the mussels using semi-circular shells is introduced. In the subsequent paragraphs, the details on the dimensions of the shells are elaborated on. At last, the final design is presented.

#### 3.1.1. Scaling

To reconstruct the situation in the field in the flume, the physical model needs to be scaled. The scaling principle prescribes that the dimensionless Froude number should be the same in the field and in the flume.

$$Fr = \frac{u}{\sqrt{gL}} \quad (3.1)$$

Where  $g$  is gravitational acceleration and  $L$  is the characteristic length.

With the help of a factor  $n$ , the ratio between the length of the prototype ( $p$ ) and the model ( $m$ ), the time, velocity and force can be scaled. This is done according to the following equations:

$$\sqrt{n} = \frac{t_p}{t_m} \quad (3.2)$$

$$\sqrt{n} = \frac{u_p}{u_m} \quad (3.3)$$

$$n^3 = \frac{F_p}{F_m} \quad (3.4)$$

The effect of the growth of mussels on vertical poles is studied for a steady flow and waves. The experimental program for waves covers a broad range of  $KC$  numbers ranging from inertia to drag-dominated conditions, always remaining in the turbulent flow regime inside the cylinder wake as stated in section 2.4). For the high  $KC$  number, the  $Re$  number decreases. The  $Re$  number is directly proportional to the length, whereas the  $KC$  number is inversely proportional to it. This means that very high diameters result in turbulent conditions (high  $Re$  numbers) but may fall in the inertial range (low  $KC$  numbers). The bamboo poles have a diameter of 15 cm in the field. After iterations and considering all relevant aspects, it was decided to apply a scale of 1:6. Since the smallest mussels with the 1:6 scale were too small to be printed (as they were below the minimum resolution of the 3D printer), a 1:3 scale was also applied to investigate the effect of different mussel sizes.

### 3.1.2. The base of the physical model

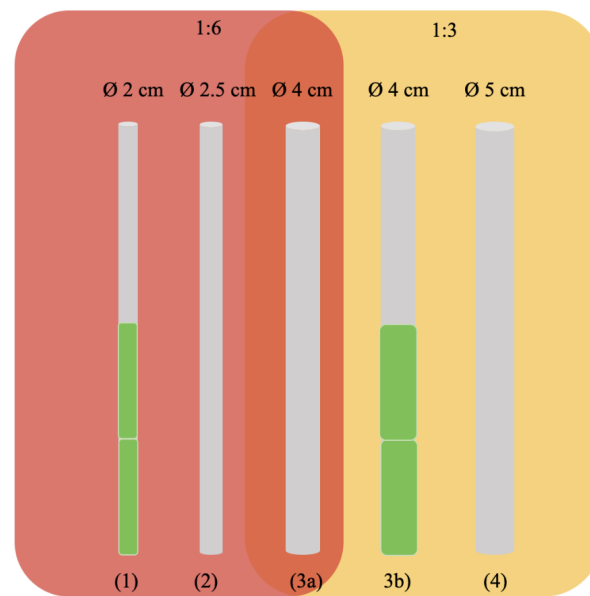


Figure 3.1: Overview of the cylinders used during the experiments with a 2, 2.5, 4 and 5 cm diameter. The cylinders with a scaling of 1:6 are included in the red rectangle and with the scaling of 1:3 in the yellow rectangle. The part of the cylinder covered by mussel rings is depicted with green squares.

The starting point of the physical model is a smooth single vertical cylinder with a length of 76 cm that is rigidly fixed at the top. The cylinder mimics a bamboo pole without mussel growth as part of the proposed aquaculture. It also serves as a base for the semi-circular cylindrical shells that simulate mussel growth. Therefore, different cylinders account for smooth cylinders and as a base for mussel growth. The different diameters are displayed in figure 3.1, from left to right in ascending order. For scale 1:6, cylinder 1 (with mussel growth) is compared to cylinder 2 (smooth) and also to cylinder 3a (smooth). The latter has the same frontal area as cylinder 1 and is added to verify the effect of roughness elements on the drag coefficient. For scale 1:3, cylinder 3b is the base of the two sizes of mussels and is compared to the cylinder without mussels (cylinder 4). The equivalent diameter is not considered during the 1:3 scale experiments. Regarding the material, all cylinders are made from aluminium except for cylinder 4. Cylinder 4 is made of PVC due to economic reasons.

### 3.1.3. Construction around the cylinder

The cylinder is rigidly fixed at the top to a force transducer, which is attached to a wooden construction (figure 3.2a). This contrasts with the field conditions, where the bamboo poles are drilled into the ground. The field conditions could have been emulated using a false bed. However, this concept could not be implemented as the force transducer was not water-resistant and the false bottom could have disturbed the flow. To avoid modifying the flow conditions with the artificial bed, the force transducer was attached to the top rather than at the base of the cylinder. Unfortunately, the 2.5 cm diameter cylinder vibrated heavily back and forth when the velocity increased during the experiments. Therefore, the construction was adjusted by fixing the 2.5 cm diameter cylinder rigidly at a lower point where the force was measured. This is depicted in figure 3.2b.

### 3.1.4. Realistic modelling of mussel growth

Semi-circular cylindrical shells (rings) with roughness elements are designed to model mussel growth. The mussels are schematised by an impermeable layer (layer 2 in figure 3.4) and an outer roughness (layer 1 in figure 3.4). Layer 2 is assumed impermeable since, in nature, the lower part of the mussels is so closely packed that the flow can be considered negligible (Marty et al., 2021). The rings consist of a third inner layer, which is added to make them rigid and re-use cylinders of previous experiments in the laboratory.

### 3.1.5. Mussel characteristics in Demak

To finish the design, the mussel dimensions had to be determined. Little information was available on the average dimensions of the green Asian mussels (*Perna Viridis*) that grow in Demak. A mussel length of 5 cm



(a) Cylinder fixed at the top



(b) Cylinder fixed halfway

Figure 3.2: Two structures to make the cylinder rigidly fixed. Figure (A) was used for all cylinders except for the smooth cylinder with a diameter of 2.5 cm.

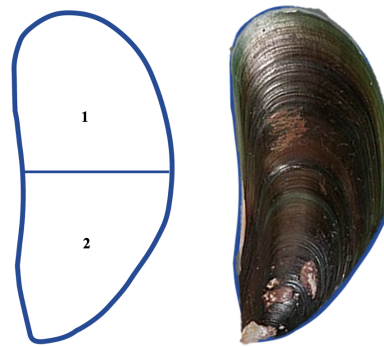


Figure 3.3: Outline of the green Asian mussel. Region 1 is schematised as a roughness element, and region 2 is an impermeable layer.

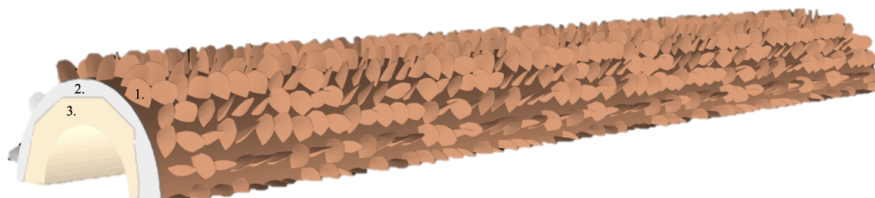


Figure 3.4: The final design consists of (1) Roughness elements (2) Impermeable layer (3) Extra thickness. The 3D model is made in Fusion360 by Flip Colin

was assumed, based on the target size for commercial purposes. Next, the width, the thickness and the height of region 1 (in figure 3.3) were estimated by studying the proportion using six images. The numbers of the schematisation used are presented in the table 3.1.

Table 3.1: The average dimension of the green Asian mussel

Scale	Width [cm]	Thickness [cm]	Height of region 1 [cm]
1:1 (field)	2.4	1.5	2.8
1:3	0.8	0.5	0.93
1:6	0.4	0.25	0.47



After that, the complete shape of the mussels was obtained from a 3D model in Sketchfab. The model replicated an image already used to determine the average dimensions. Eventually, it was scaled to the average dimensions for the 1:3 and 1:6 scales for the final designs.

Next, the spatial distribution and orientation of the mussels were obtained by digitising images of mussel poles from the field. Similar to research by Marty et al. (2021), the mussels were drawn as lines and thereby, the major axis of inclination was derived for each mussel. It was concluded that 52 % of the time, the mussels have a 45 °or 90 °difference with their neighbour and the rest of the time, the mussels have an average of  $\pm 10$  °difference. Moreover, the inclination was influenced by neighbouring mussels. These three aspects were incorporated in a Python script and randomly generated into a staggered pattern. Figure 3.5 illustrates the process, and details are provided in the Appendix A.

In summary, the roughness elements were defined by the average dimensions, the realistic shape and the pattern.

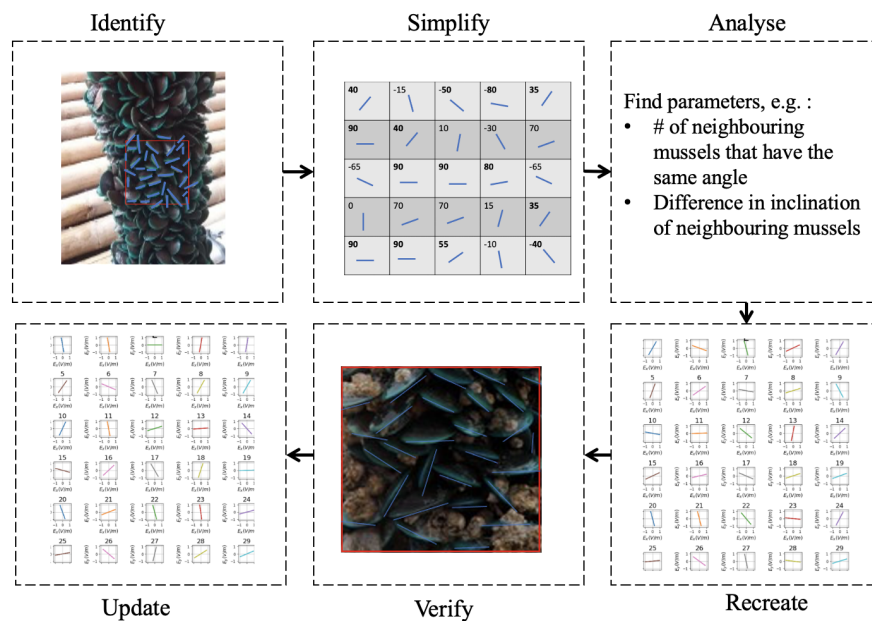


Figure 3.5: Process of obtaining the spatial distribution and orientation of the mussels with the help of images from the field.

### 3.1.6. Final design of the physical model

With the information of the previous section, the final designs for the 1:6 and 1:3 scale mussels are made. The ring with a scale of 1:6 for the mussels is referred to as the "standard' mussel ring. The two designs for 1:3 scaled mussels study the difference between a marketable mussel (5 cm in the field) and a not fully grown mussel (2.5 cm in the field). From now on they are named, named 'Large-sized mussels' and 'Medium-sized mussels' respectively. Each ring has a height of 24 cm, and the cylinder needs three rings stacked to fully cover a cylinder. The dimensions of the designs are summarised in the table 3.2.

Table 3.2: The details on the final design of the mussel rings. The relative roughness ( $e$ ) is calculated by dividing the roughness height by  $2^*$ superimposed layer +  $2^*$  extra layer thickness + the inner diameter.

	Standard mussel	Large sized mussels	Medium sized mussels
Scale	1:6	1:3	1:3
Roughness height (1)	0.36 cm	0.73 cm	0.36 cm
Superimposed layer (2)	0.47 cm	0.93 cm	0.47 cm
Extra layer thickness (3)	0.25 cm	0.5 cm	0.5 cm
Distance between mussels	0.4 cm	0.8 cm	0.4 cm
Inner Diameter	2.0 cm	4.0 cm	4.0 cm
Relative roughness ( $k/D$ )	0.10	0.10	0.06

The final design was a 3D model in Fusion360 by Flip Colin. First, the mussel rings were printed with a 3D

printer and multiplied with resin casting. The 3D printed model was used to cast a silicone mould, and with Polyurethane, the rings were reproduced. This technique saved time and expense, as the 3D printer requires 2-3 days to print each (complete) ring. At last, the rings are attached with four screws around the cylinder.

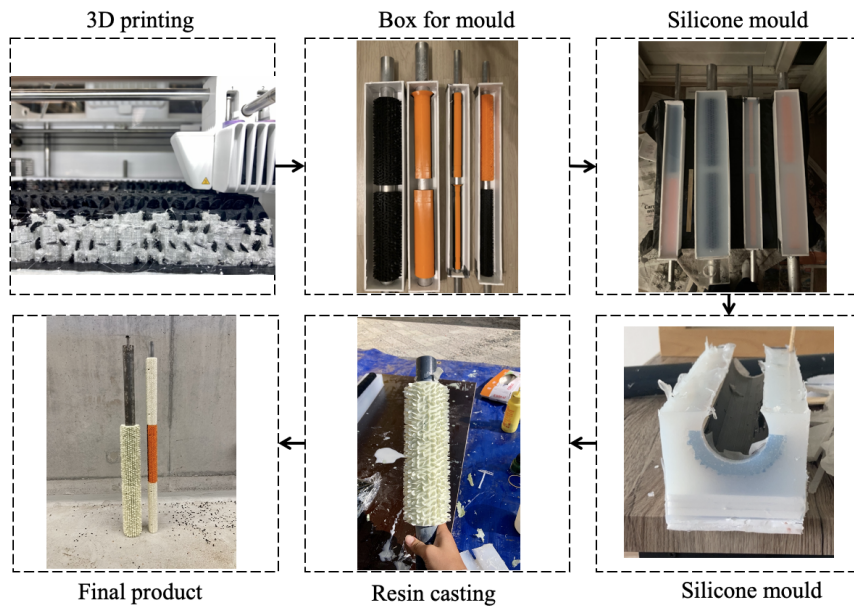


Figure 3.6: Overview of the physical model process with the help of a 3D model and resin casting.

Further information and impressions on the mussels' design aspects are in appendix A.

## 3.2. Laboratory experiments

This section discusses the general wave flume properties, followed by the instrument set-up for data collection, the program and a description of the experiments done to answer the objectives.

### 3.2.1. General wave flume properties

The experiments were conducted in the wave flume of Delft University of Technology, which has a length of 40 m, a width of 0.80 m and a maximum water depth of 1.0 m. The outline of the flume is depicted in figure 3.7. A wave generator with reflection compensation (1) is placed at one side of the flume and a wave absorber (2) at the opposite end. The flume can be filled and drained by the inlets and outlets (3 and 4) on each side. During the experiments, the inlets and outlets remained closed. Metal plates with holes (5a and 5b) cover the openings to the inlet and outlets (3a,3b,4a,4b) and ensure that water depth is the same everywhere. Moreover, the metal plates (5a and 5b) prevent large objects from floating through the pipe system.

The wave flume was transformed in order to reproduce steady flow conditions. For this purpose, the wave absorber and the metal plates were removed (5a and 5b). Otherwise, metal plate 5a would experience a large upward force from the incoming force and metal plate 5b would disturb the outflow. In addition, a weir in front of opening B was placed, providing the flume's desired water depth. Lastly, the steady flow was created by opening the inlet at the start of the flume (3a) and the outlets at the end flume (4b).

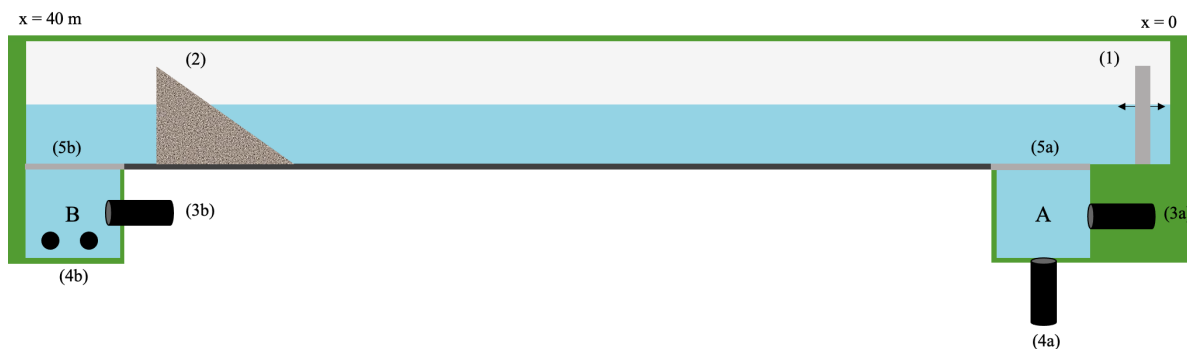


Figure 3.7: The outline of the wave flume:(1) Wave generator,(2) Wave absorber, (3ab) Inlets, (4ab) Outlets and (5ab) Metal plates

### 3.2.2. Data collection

The free surface elevation, the force acting on a cylinder, and flow velocities over depth are measured for every test. This is done with the following instruments:

1. **The wave gauges (WG)** record the free surface elevation. The wave gauge consists of two parallel stainless steel rods that measure the conductivity of water, which depends on the water level. Therefore, the output signal is in voltage and converted to the free surface elevation in meters with the calibration coefficient. These instruments were developed by Deltares and had an accuracy of 0.5 % (Deltares, 2021). The location of the wave gauges is depicted in Section 3.2.4.

The wave gauge measures the incoming wave amplitude and reflected wave amplitude.

2. **The electromagnetic velocity meters (EMF)** record the velocity of the fluid and consist of two parallel rods that measure voltage. The output is in volts and is converted to the flow velocity in m/s using the calibration factors provided by Deltares.

The EMF measures the undisturbed velocity, which is used together with the force measurements to determine the drag coefficient. The EMF is placed at 5 levels above the bed to create a velocity profile. The EMF can not measure too close to the bed of the flume because the bed would disturb the electromagnetic field. Thus, the lowest point it could measure is  $z = 4$  cm. This instrument has an accuracy of 0.5 % (Deltares, 2021).

3. **The force transducer** (FT) is used to measure the drag force on the cylinder.

The force transducer is calibrated with a Newton meter. The calibration constant is the difference in force divided by the output voltage. The AL10 C3SH 5e from Scaime is implemented with an amplifier of 1000.

More details on the instruments are included in the Appendix B.

### 3.2.3. Experimental program

The experimental set-up starts by testing all cylinders (with and without mussels) in a steady flow. The experiments cover Reynolds numbers between 1000 and 10 000 to study how mussels affect the drag crisis and the magnitude of the drag coefficient of the poles.

The various  $Re$  numbers are obtained by adjusting the flow velocity in the flume. In doing so, the water depth is set to 0.4 meters. Hence, the required velocity required a balance between the height of the weir and the opening of the inlet. The test was repeated five times per velocity for 3 minute intervals. Each time, the position of the EMF was changed over the depth to obtain the velocity profile. The EMF measured the velocity at  $z = 0.04$  m,  $z = 0.05$  m,  $z = 0.10$  m,  $z = 0.20$  m and  $z = 0.30$  m. When the data was collected at all elevations, the height of the weir was adjusted to obtain a new flow velocity. After a 5-minute period of flow adjustment, force and velocity measurements were collected. This process was done for all flow conditions. Table 3.3 gives the experimental program of the steady flow. The outer diameter ( $D_o$ ) was used as characteristic length scale for  $Re$  to determine the flow velocity to be reached. The outer diameter is determined as the sum of the thickness of layers 1, 2 and 3 for the mussels.

Table 3.3: A rough estimation of the flow velocity that needs to be reached to obtain  $Re = 10^3 - 10^4$  is calculated with the outer diameter. The steady flow is generated by manually adjusting a pump and it is not possible to set the flow to a certain velocity. Therefore a rough estimation was made to create a range of flow velocities.

Cylinder	$D_o$ [cm]	(Estimated) U [m/s]
1. Smooth cylinder	2.5	0.04 - 0.4
2. Standard Mussels	4.16	0.024 - 0.24
3. Equivalent Diameter	4	0.025 - 0.25
4. Smooth cylinder	5	0.02 - 0.2
5. Medium sized mussels	6.66	0.015 - 0.15
6. Large sized mussels	8.32	0.012 - 0.12

In the second part, the experiments are executed for various wave conditions. The waves cover a region of  $KC$  numbers from 3 to 113. Two situations are tested, the cylinder with a diameter of 2.5 cm and the standard mussels. To investigate the effect of the mussels, the wave height is scaled to obtain similar  $KC$  numbers for the smooth cylinder and the cylinder with mussels. This is done according to the following equation:

$$a_{w,2} = a_{w,1} \frac{D_1}{D_2} \quad (3.5)$$

Where  $a_w$  is the wave amplitude,  $D$  is the diameter of the cylinder, the subscript 1 represents the wave amplitude and diameter for a situation without mussels, and the subscript 2 for a situation with mussels. Given the wave amplitude and diameter for a smooth cylinder as input, the wave amplitude that would give the same  $KC$  number for a cylinder with mussels is calculated with equation 3.5.

The tests were repeated six times per wave condition, varying the height of the EMF between the tests to obtain the velocity profile. The water depth was 0.50 meters, and the velocity was measured at  $z = 0.04$  m,  $z = 0.05$  m,  $z = 0.10$  m,  $z = 0.20$  m,  $z = 0.30$  m and  $z = 0.40$  m. Also, a 3-minute waiting time between the tests was included to ensure that the water was still before starting a new experiment. The complete experimental program of the waves is shown in table 3.4.

Cylinder	H [m]	$T_w$ [s]	h [m]	KC number[-]
1.Smooth cylinder	0.04	1	0.5	5.2
2.Smooth cylinder	0.04	2	0.5	7.7
3.Smooth cylinder	0.04	3	0.5	11.0
4.Smooth cylinder	0.13	1.5	0.5	20.3
5.Smooth cylinder	0.13	2	0.5	25.2
6.Smooth cylinder	0.13	3	0.5	35.9
7.Smooth cylinder	0.13	4	0.5	47.1
8.Smooth cylinder	0.13	5	0.5	58.4
9.Smooth cylinder	0.13	6	0.5	69.75
10.Smooth cylinder	0.13	7	0.5	81.2
11.Standard mussel	0.066	1	0.5	5.2
12.Standard mussel	0.066	2	0.5	7.7
13.Standard mussel	0.066	3	0.5	11.0
14.Standard mussel	0.2163	1.5	0.5	20.3
15.Standard mussel	0.2163	2	0.5	25.2
16.Standard mussel	0.2163	3	0.5	35.9
17.Standard mussel	0.2163	4	0.5	47.1
18.Standard mussel	0.2163	5	0.5	58.4
19.Standard mussel	0.2163	6	0.5	69.75
20.Standard mussel	0.2163	7	0.5	81.2

Table 3.4: The tested wave conditions

### 3.2.4. Wave generation

The waves were created by defining the paddle motion using the script in Appendix C. The script is based on method of Goring (1978), which states that velocity of the wave paddle should be the same as the depth integrated velocity of the particles under the wave. The equation is as follows:

$$\frac{dX}{dt} = U_{da}(X, t) \quad (3.6)$$

Where  $X$  is the location of the wave paddle and  $U_{da}$  is the depth averaged velocity. van Wiechen (2020) showed that the Fenton theory predicts the celerity, surface elevation and the orbital velocities better than the Korteweg-de Vries theory. Therefore, the script used the Fenton theory to obtain the paddle motion. First, the script created cnoidal waves with small bumps in the troughs. This was caused by the Stokes drift of the paddle motion. This was removed by subtracting the mean Stokes drift from the instantaneous velocities.

### 3.2.5. Set-up wave flume

In figures 3.8 and 3.9, the set-up of the physical model and the instruments in the flume is shown for the steady flow and wave experiments. The model was located at the end of the flume, since for the studied Reynolds numbers the turbulent boundary layer is fully developed at a distance of  $x = 33$  m from the start of the flume (Appendix D). Contrary to the steady flow, the wave experiments were placed as close to the wave generator as possible. This was done to prevent interference between the incoming waves and the reflected waves from the back of the flume. Resulting from this the available time is the time a wave takes to reach the wave absorber and back to the model.

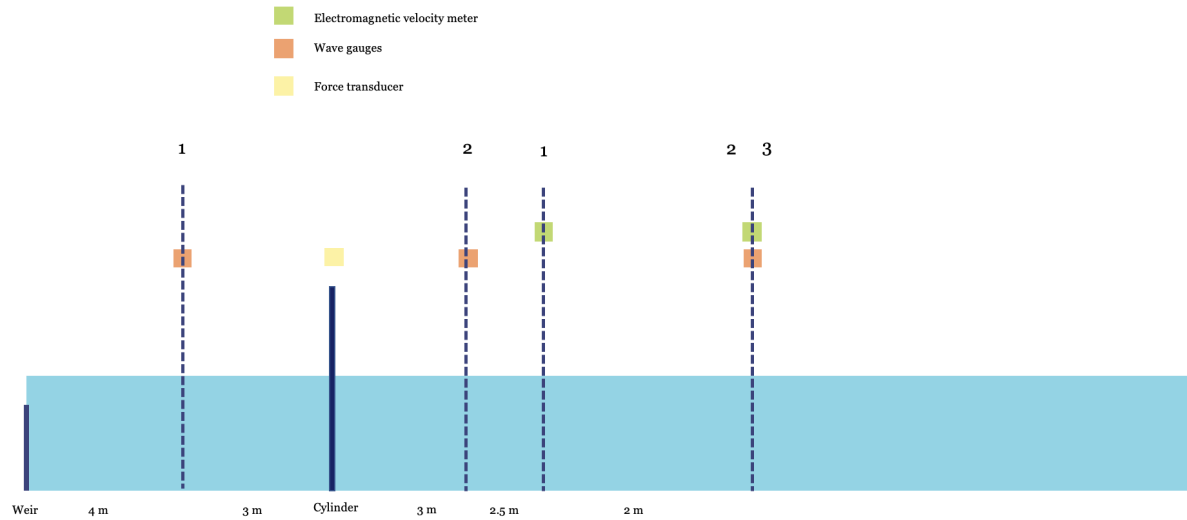


Figure 3.8: The set-up of the flume for the steady flow experiments

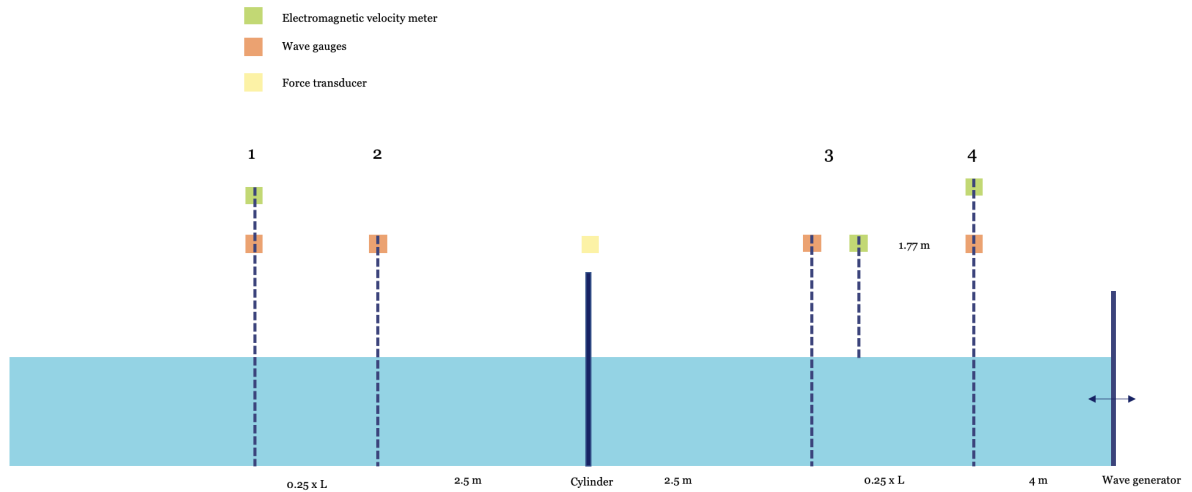


Figure 3.9: The set-up of the flume for the oscillatory flow experiments

### 3.3. Data processing of the steady flow

This section explains how the data was processed.

#### 3.3.1. General outline for the steady flow

Figure 3.11 shows the flowchart for the data processing of the steady flow experiments. The first step was to remove the offset of the instruments in still water. The offset of each sensor was determined by recording the signal in still water, before the pump was started. After that, the output of the instruments was transformed from voltage to the physical units using the calibration factor of each sensor. Next, the outliers were removed with the interquartile range. The time series of different experiments had small variations in the total duration, and an interval of 3 minutes was selected for further analysis. The depth-wise velocity was determined by combining the results collected at elevations of  $z = 0.04$  m,  $z = 0.05$  m,  $z = 0.10$  m,  $z = 0.20$  m and  $z = 0.30$  m from the bed. For each elevation, the mean velocity was calculated using an averaging interval equal to  $dt = 5$  s. Averaging between  $dt = 5 - 2000$  was also evaluated, but it had a negligible effect on the mean values (see Appendix E). Then, the depth-integrated velocity squared was determined by integrating the velocity measurements over the vertical. Since there were only five points velocity points, and they did not have an equal separation over the water depth, the depth-integrated velocity squared was approached by discretisation and weighing factors that accounted for the relative distance between points, as shown in figure 3.11. Lastly, the drag coefficients were then obtained using Equation 2.3 with the measured mean force, the measured water depth, the (equivalent) diameter and the depth-integrated velocity squared.

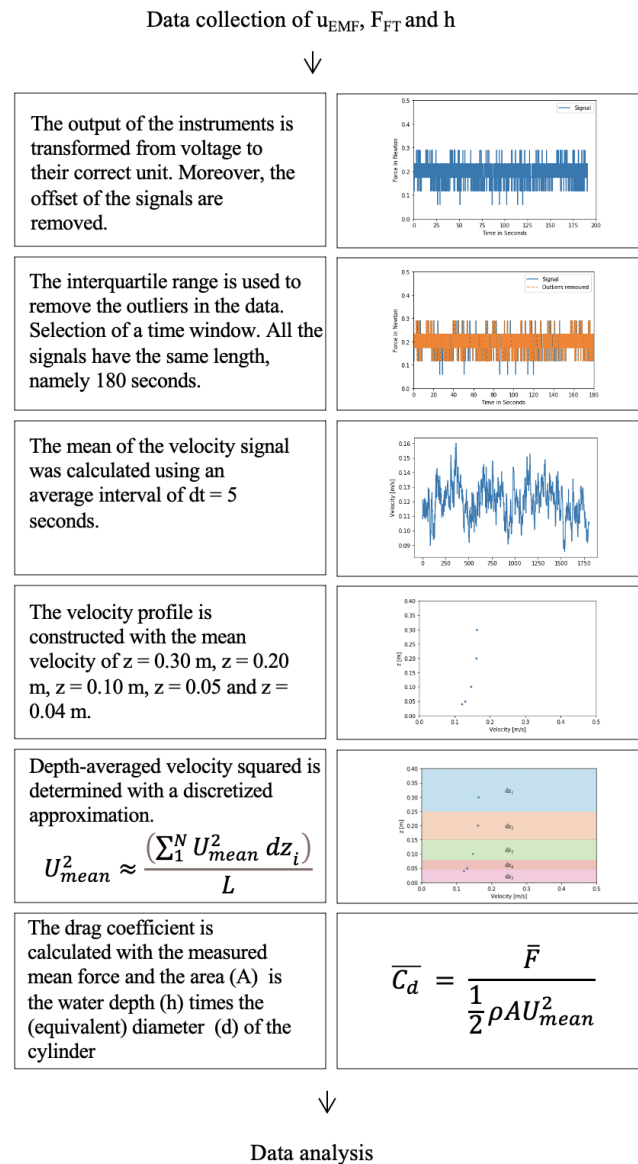


Figure 3.10: The flow chart for the data processing of the wave experiments. With  $u$  the velocity,  $F$  the force and  $h$  is the water depth.

### 3.4. Data processing for the waves

This section explains how the raw data was processed for the wave experiments. It followed a similar procedure as the steady flow data processing. However, the phase shifting of all the measurements to the location of the cylinder was added.

#### 3.4.1. General outline for the waves

Figure 3.11 shows the flowchart for the data processing of the wave experiments.



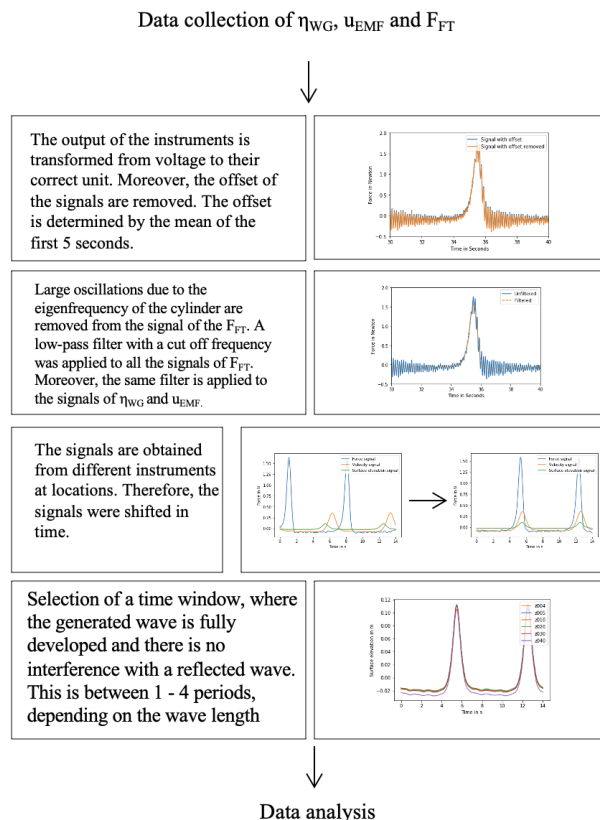


Figure 3.11: The flow chart for the data processing of the wave experiments, since surface elevation, forces and velocities were measured at different positions along the flume. With  $\eta$  representing the surface elevation,  $u$  the velocity, and  $F$  the force.

The processing started with transforming the output of the instruments to the correct unit with the help of calibration factors and equations. Then, the offset was removed from the signal. The offset was calculated as the average value over the first 5 seconds of the data when the water is still. Next, the large cylinder oscillations were removed by applying a low-pass filter, further explained in section 3.4.2. The third step was to phase shift all the measurements to the location of the cylinder. This was further explained in section 3.4.3. Next, the time window for analysis was selected, considering the part of the time series where the waves were fully developed, but wave reflection from the absorber had not yet reached the sensors. Therefore, the time window varies from 1 wave to 4 wave periods, depending on the wave conditions. Once the signals were filtered, and the period for analysis was selected, the depth integrated velocity squared and the depth integrated acceleration were calculated for each time step. Since the measurements did not fully cover the water depth, the velocity and acceleration were extrapolated at the bottom ( $z=0$  m) and at the water surface ( $z=0.5$  m). The drag and inertia coefficient were then obtained by applying Equation 2.6, using two different methods, a least square fit and the maximum likelihood method.

### 3.4.2. Low pass filter

A low-pass filter with a cut off frequency was applied to the signals of the  $\eta_{WGS}$ ,  $U_{EMFS}$  and  $F_{FT}$ . The filter was used to remove the oscillations due to the eigenfrequency of the cylinder in the force data and removed the noise. The same filter conditions were used for all of the wave conditions. Therefore, the cut-off frequency was based on the wave conditions with the most significant disturbance in the signal. This was the case for the wave with a wave height of 13 cm and a period of 7 seconds (H013T7). Figure 3.12 presents the magnitude spectrum and the chosen cut off frequency as a vertical dotted line at  $f = 0.05$  Hz. Multiple wave conditions were checked to see if the value did not suppress essential frequencies. This was not the case, as shown in figures 3.13 and 3.14.

The effect of the low-pass filter was significant for the force signal of H013T7, but very small for the other

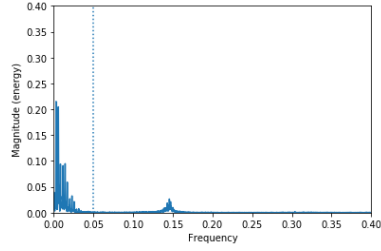


Figure 3.12: The magnitude spectrum of wave height of 13 cm and period of 7 seconds (H013T7). The vertical line represents the cut off frequency of 0.05 Hz.

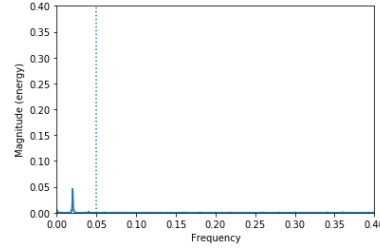


Figure 3.13: The magnitude spectrum of wave height of 4 cm and period of 1 second (H004T1). The vertical line represents the cut off frequency of 0.05 Hz.

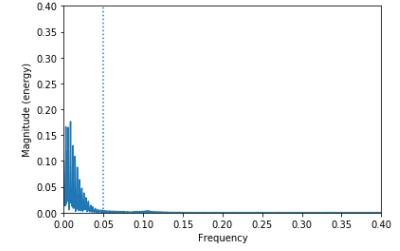


Figure 3.14: The magnitude spectrum of wave height of 21.6 cm and period of 7 seconds (H0216T7). The vertical line represents the cut off frequency of 0.05 Hz.

signals and wave conditions. This was because there is no disturbance by the eigenfrequency of the cylinder for H004T1 and H0216T7, confirmed by figures 3.13 and 3.14 and the percentages in table 3.5.

Wave	Cutoff [Hz]	Variance loss FT [%]	Variance loss EMF [%]	Variance loss WG [%]
H013T7	0.05	7.37	0.0002	0.0002
H004T1	0.05	0.04	0.0180	0.009
H0216T7	0.05	0.005	0.0013	0.001

Table 3.5: The effect of the cut-off frequency on the variance for the different instruments and different wave conditions.

The low pass filter was chosen after discussing five filters in appendix F.

### 3.4.3. Calculation of the phase velocity

The measurements of the surface elevation, flow velocity and forces were collected at different locations along the flume. In order to refer all measurements to the location of the cylinder, the time series of the different instruments were shifted in time according to:

$$\delta t = \frac{d}{C_g} \quad (3.7)$$

Where  $d$  is the distance between two sensors and  $C_g$  is the group celerity. The group celerity was calculated by determining the time shift between the signals of wave gauges 1, 2, 3 and 4.

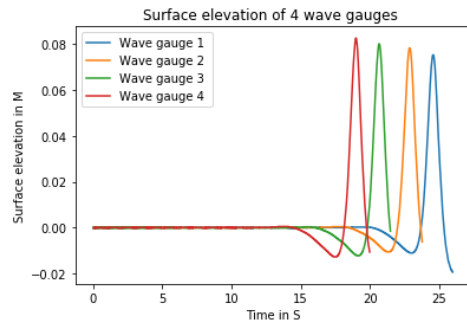


Figure 3.15: Each of the four wave gauges measured the surface elevation. Whereby, wave gauge four was positioned the closest to the wave generator

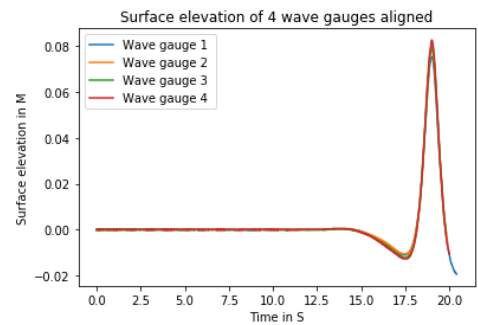


Figure 3.16: The aligned surface elevation measured by each of the four wave gauges

# 4

## Results

This chapter discusses the results of the experimental program. First, in section 4.1 the derivation of the equivalent diameter for the mussel covered cylinder is shown. Then, in section 4.2, the steady flow results are presented. Next, the results of the wave experiments are shown in section 4.3.

### 4.1. General

#### 4.1.1. Equivalent Diameter

The equivalent diameter ( $D_{eq}$ ) of the mussel covered cylinders is determined by projecting the 3D model of the mussel covered cylinder on a 2D plane and dividing the projected area by the cylinder height. The projected area is derived by transforming a 2D image into a binary image, as seen in figures 4.1 and 4.2. The percentage of black pixels in the image can be calculated by counting the black and white pixels. Then, the percentage of black pixels is used to derive the area of the cylinder in the image. Eventually, with the help of scaling, the surface area of the mussel covered is determined for the actual size. Lastly, the equivalent diameter is derived by dividing the area by the height of the shell (24 cm).

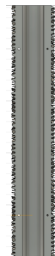


Figure 4.1: Image of the standard mussel covered cylinder



Figure 4.2: Binary image for MATLAB

For the standard mussel, the derivation results are presented in table 4.1. The physical model consists of two shells with each a different pattern. Therefore, the two sides of the model are compared and from the table it becomes clear that the difference is negligible.

Table 4.1: Determination of equivalent diameter for the standard mussel

Ring side	Number of white pixels	Number of black pixels	$A_{blackpixels}$	$D_{eq}$
1	40658	198768	95.804 cm <sup>2</sup>	3.99 cm
2	40829	200736	95.943 cm <sup>2</sup>	4.0 cm

The same is done for the medium sized and large sized models, and the results are in table 4.2. The equivalent diameters are used to determine to drag coefficient for the mussel covered cylinders.

Mussel version	$D_{eq}$
Standard mussel	4 cm
Medium sized mussel	6.5 cm
Large sized mussel	8 cm

Table 4.2: The equivalent diameters of the three mussel covered cylinders

## 4.2. Results of the steady flow experiments

This section describes the results of the steady flow experiments, where cylinders with and without mussels were exposed to a fully developed flow. Section 4.2.1 presents a measured velocity profile and compares different methods to obtain the depth-integrated velocity. The result of the drag coefficient for smooth and mussel cylinders are shown in section 4.2.2.

### 4.2.1. Velocity profile

Figure 4.3 presents a 5-points velocity profile and a 13-points velocity profile, constructed as in figure 3.11, for the same steady flow condition, which corresponded to a target depth-integrated velocity of  $U = 0.09$  m/s. The values of 13-points velocity profile were measured during one of the experiments. The error bars show the variability in the velocity and the velocity has a mean relative variation of 6%. An exponential function is fitted to the 13 velocity points profile from the bed to the surface level. The depth-integrated velocities of the fitted function and the 13-points velocity profile are compared to the depth-integrated velocity 5-points velocity profile, as the latter is the number of velocity points measured during the experiments.

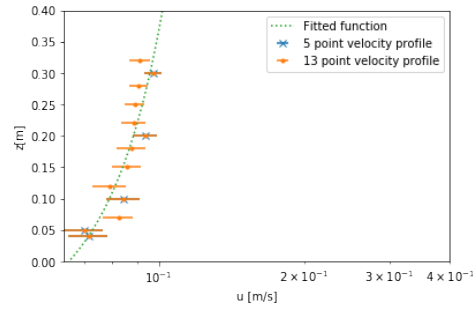


Figure 4.3: Comparison of a 5-points velocity profile (blue crosses) to a 13-points velocity profile (orange dots). The variability in the velocity signal is depicted with error bars at each point. An exponential function is fitted to the data points of the 13-points velocity profile (dashed green line)

The comparison of the depth-integrated velocities is presented in table 4.3. First, the 5-points velocity profile is compared to the 13-point velocity profile and the fitted function of the 13-points velocity profile. The latter is assumed to accurately represent the velocity profile because it includes the velocity at the bed and the surface. Therefore, it aims to derive a similar depth-integrated velocity of the fitted function with the 5-point velocity profile. Next, the velocities are derived with two methods: the mean of the values (equation 4.1) and the square root of the mean of the values (equation 4.2).

$$\bar{U} = \frac{\sum \bar{U} dz}{L_{shell}} \quad (4.1)$$

$$\bar{U}_{RMS} = \sqrt{\frac{\sum \bar{U}^2 dz}{L_{shell}}} \quad (4.2)$$

Consequently, the same equations are used for  $U^2$  and  $U_{RMS}^2$ . In figure 4.3. It becomes clear that the root mean square (RMS) approaches the velocity of the function the best for the velocity profiles. Moreover, the difference between the 5 and 13 points' velocity profiles is negligible. Therefore, the 5 points velocity profile is considered sufficient to derive the depth-integrated velocity accurately.

Velocity profile	$\bar{U}[m/s]$	$\overline{U_{RMS}}[m/s]$	$\overline{U^2}[(m/s)^2]$	$\overline{U_{RMS}^2}[(m/s)^2]$	$\int udz[m/s]$	$\int u^2 dz[(m/s)^2]$
5 - points	0.079	0.089	0.006	0.008	-	-
13 - points	0.089	0.088	0.008	0.008	-	-
Fitted function	-	-	-	-	0.086	0.008

Table 4.3: The depth-integrated velocity and velocity squared are presented for the velocity profiles and the fitted functions. The mean depth-integrated velocity ( $\bar{U}$ ) and velocity squared ( $\overline{U^2}$ ) are compared to the square root of the mean of the values ( $U_{RMS}$  and  $U_{RMS}^2$ ) to approach the  $\int udz[m/s]$  and  $\int u^2 dz[(m/s)^2]$  of the fitted function.

#### 4.2.2. Drag coefficients

Figure 4.4 shows the results of the steady flow experiments. First, figures 4.4a, 4.4c and 4.4e compare a smooth cylinder with the standard mussel cylinder and a cylinder with an equivalent diameter for a scale of 1:6. Figures 4.4b, 4.4d and 4.4f compare a smooth cylinder to the medium and large mussel cylinder for a scale of 1:3. Next, the obtained drag coefficients are plotted with values from the literature and with fitting lines adjusted to the present experiments, as seen in figures 4.4c, 4.4d, 4.4e and 4.4f.

The measured drag coefficients form a distinct line when plotted against the Reynolds numbers (figure 4.4). However, the fitted curves do not correspond with  $C_d-Re$  relationships for smooth cylinder from the literature such as White (2006) and Munson et al. (1994). Instead of approaching a drag coefficient of 1 and 1.17 for  $Re > 8000$ , the smooth cylinders approach drag coefficients of 1.49 and 1.74. Moreover, the drag coefficient of the literature increases exponentially for  $Re < 200$  as seen in figure 2.4. This phenomenon can already be seen for  $Re < 2000$  for the experiments. Standards mussels have a small effect on the drag coefficient for the scale of 1:6. However, an evident difference is noticeable between the smooth cylinder and the larger mussels. This is also shown in table 4.4. For  $Re = 6000$ , the drag coefficient increases to 51 % for the large mussel but only 20% for the standard mussel. The largest differences between the mussels and the smooth cylinder for both scales can be seen for  $Re = 3000 - 6000$ . For  $Re > 6000$ , these differences decrease. It is important to notice is that for  $Re = 6000 - 8000$ , the drag coefficients of the medium mussels are smaller than for the smooth cylinder.

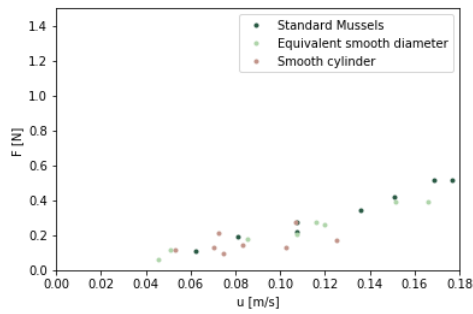
Re [-]	$C_{d,S1:6}[-]$	$C_{d,ES1:6}[-]$	$C_{d,SM}[-]$	$C_{d,S1:3}[-]$	$C_{d,MM}[-]$	$C_{d,LM}[-]$
4000	2.32	2.67	2.81	2.85	3.12	4.74
6000	1.88	2.09	2.25	2.25	2.08	3.40
8000	1.68	1.75	1.98	1.72	1.81	2.00
10000	1.63	1.63	1.86	1.93	1.43	2.33

Table 4.4: The values of the drag coefficients of the fitted lines for the tested cylinders. S1:6 is the smooth cylinder for a scale of 1:6, ES1:6 is the smooth cylinder with an equivalent diameter as S1:6, SM is the Standard Mussel, S1:3 is the smooth cylinder for a scale of 1:3, MM is the half-grown mussel, and LM is the fully grown mussel.

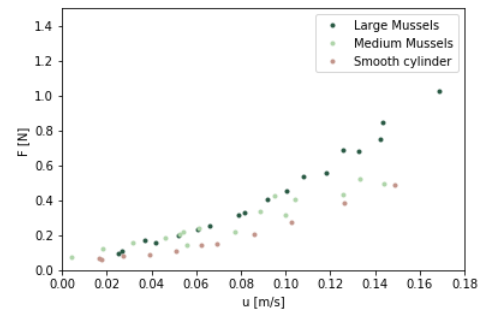
The fitted lines in figures 4.4e and 4.4f used the  $C_D-Re$  relationship by White (2006) as model function. Table 4.5 summarizes the parameters for the fitted functions.

Cylinder	a	b	c
Smooth cylinder	1.49	5109246	1.88
Equivalent diameter	0.932	6662	0.99
Standard mussel	1.41	44795	1.22
Smooth cylinder	1.74	9304875	1.92
Medium mussels	0.92	1138329	1.59
Large mussels	0.69	14566	0.98

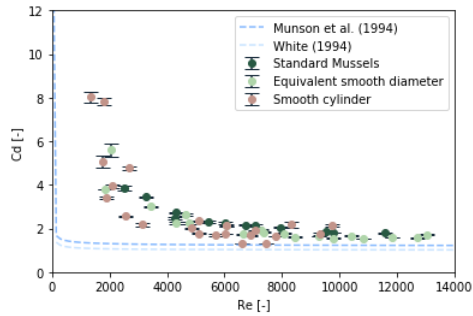
Table 4.5: The parameters  $a$ ,  $b$  and  $c$  for the fitted function based on the model function by White (2006):  $C_d = a+b*Re^c$ .



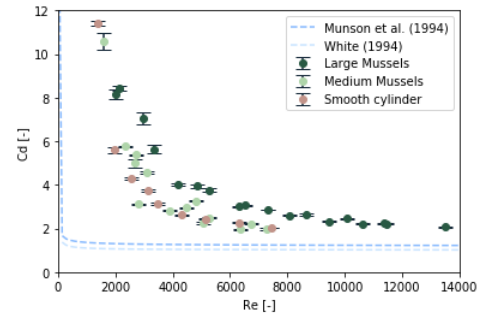
(a) The measured force plotted with the velocity for experiments with the scale of 1:6



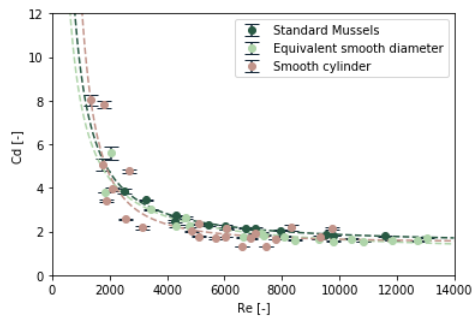
(b) The measured force plotted with the velocity for experiments with a scale of 1:3



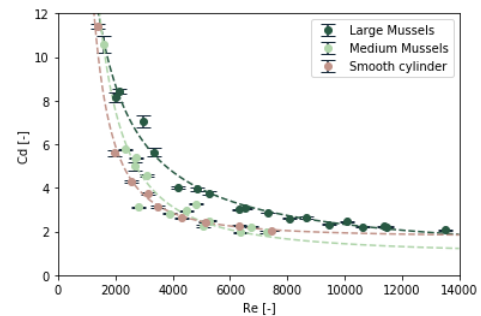
(c) The drag coefficient was plotted against the  $Re$  for experiments with 1:6 with literature



(d) The drag coefficient was plotted against the  $Re$  for experiments with 1:3 with literature



(e) The drag coefficient was plotted against the  $Re$  for experiments with 1:6 with the fitted lines



(f) The drag coefficient is plotted against the  $Re$  for experiments with 1:3 with fitted lines

Figure 4.4: The results for the two sets of the steady flow experiments, namely scales of 1:6 and 1:3. Figures 4.4a and 4.4b plot the measured force against the measured depth-integrated velocity. Figures 4.4c and 4.4d show the obtained drag coefficient plotted with fitting lines for smooth single cylinder by Munson et al. (1994) (dashed dark blue line) and White (1994) (dashed light blue line). Figures 4.4f and 4.4e present the lines that are fitted to the measured data points.

### 4.2.3. Summary of the results of the steady flow experiments

- A vertical profile for the velocity and velocity squared, consisting of measurements at five elevations, are sufficient to approach the depth-integrated velocity and velocity squared. They are best approached with the Root Mean Square method.
- The measured drag coefficients show an increase in drag coefficients for large mussels compared to a smooth cylinder. For  $Re = 6000$ , the drag coefficient is increased by approximately 50 %. However, the standard and the medium-sized mussel have a small to negligible effect on drag coefficients.

## 4.3. Results of the wave experiments

This section describes the results of the wave experiments, where cylinders with and without mussels were exposed to wave action. Figure 4.5 shows an overview of the data analysis and in the order in which the results

are presented. Surface elevation, velocity and force measurements are compared for two wave conditions, one corresponding with inertial conditions ( $KC = 3$ ) and one with drag-dominated conditions ( $KC = 113$ ). The steps followed in the data analysis are shown for those two wave conditions. First, the measured and expected wave heights and periods are compared in section 4.3.1. Then, Fenton wave theory (1985) is used to estimate the surface elevation and flow velocities for the wave conditions of table 3.4. Next, the estimates from Fenton are compared with the measured signals in section 4.3.1 for the surface elevation, and in section 4.3.2 for flow velocities and accelerations. Lastly, section 4.3.4, presents the drag and inertia coefficients derived from the measurements with the Morison equation (2.6). The equation is solved by three different methods. Force signals calculated with the obtained coefficients and measured force signals are shown to evaluate the quality of the fit of the coefficients.

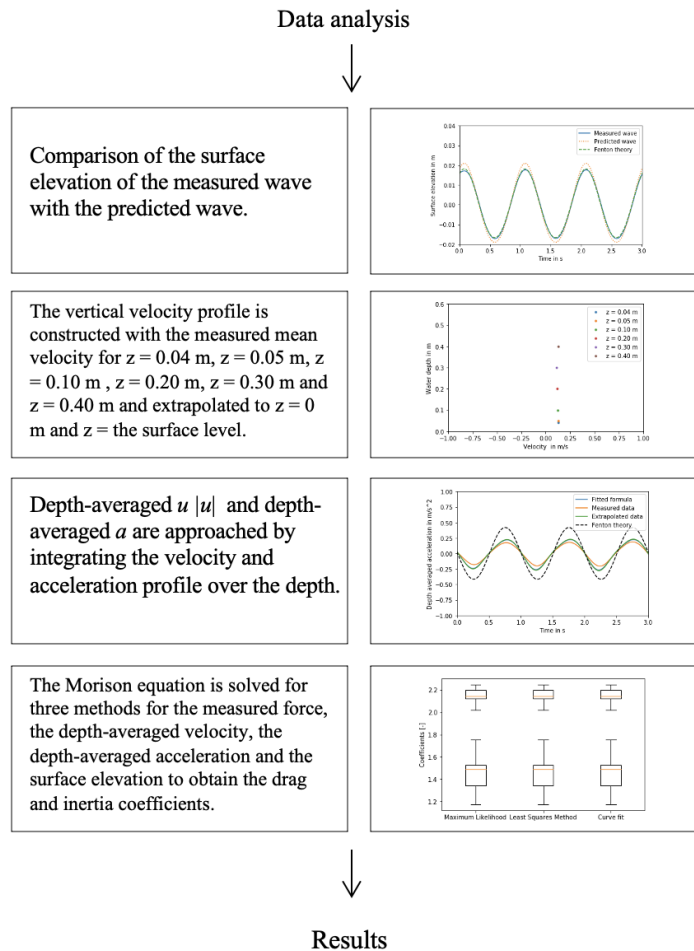


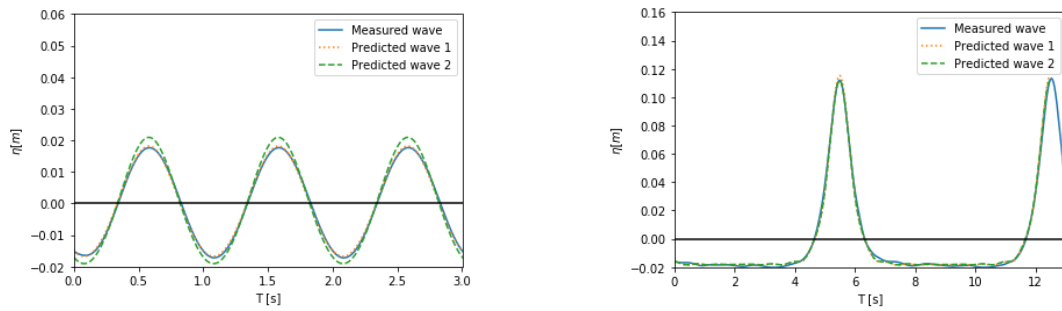
Figure 4.5: An overview of the analysis of the wave experiments. This is also the order in which the results are presented.

The measurements of the following wave conditions are not included in the results due to incorrect measurement by the force transducer: H013T15, H013T4 and H013T5. This may be caused by the cylinders touching the bed of the flume. The graphs of the surface elevation, depth integrated velocity squared ( $U|U|$ ), depth integrated acceleration and drag and inertia coefficient are presented in appendix G for every wave run.

### 4.3.1. Surface elevation

Figure 4.6 displays the surface elevation of  $H = 0.04$  m and  $T_w = 1$  s (H004T1) and  $H = 0.13$  m and  $T_w = 7$  s (H004T1). It shows that the measured and predicted wave signals have the same period but some differences in wave amplitude. The relative errors oscillated between -13 % and 19%, and the largest inconsistency corresponded to wave condition H066T2, as seen in figure 4.7. The reason for this inconsistency is unclear.

Predicted wave 2 shows the surface elevation estimated by the Fenton theory with the measured wave height as input instead of the input of table 3.4. This enables a fair comparison between the measured and expected waves and shows that the Fenton theory correlates well with the measured surface elevations for both wave conditions.



(a) The wave condition with a wave height of 0.04 m and a period of 1 second (H004T1). (b) The wave condition with a wave height of 0.13 m and a period of 7 seconds (H013T7).

Figure 4.6: The measured (solid blue line) and the predicted (dashed orange line) surface elevations are plotted for the two wave conditions. The black line represents the  $y = 0$  axis. The dashed green line is the predicted surface elevation with the measured wave height as input and is called predicted wave 2. Predicted wave 2 is used for the results.

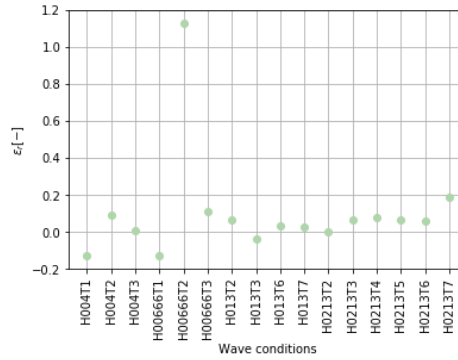
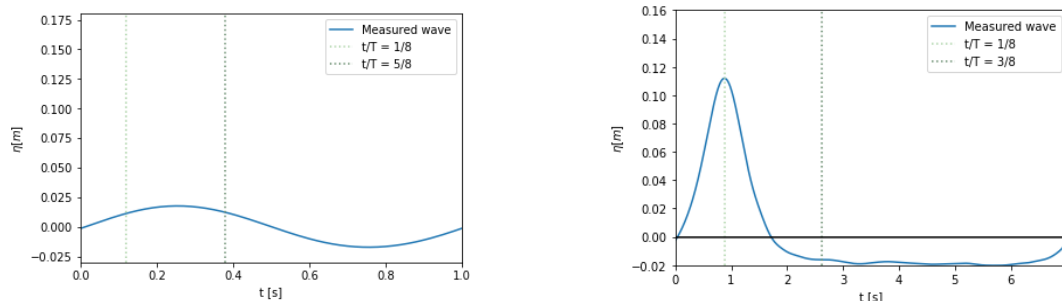


Figure 4.7: Relative error  $\epsilon = dH/H$  for different wave conditions, where  $dH$  is the difference between the target and the measured wave condition, and  $H$  is the target wave condition.



### 4.3.2. Vertical velocity and acceleration profile

The surface elevation time series are shown in figure 4.8 for H004T1 and H013T7. In addition, the vertical velocity and acceleration profiles for both wave conditions are presented for  $t/T = 1/8$  and  $t/T = 3/8$ , where  $t$  indicates the relative time with respect to the wave period  $T_w$ , as shown in figure 4.8a and 4.8b. Showing the profiles at multiple relative times validates the fit of the fitted function and the non-linear extrapolation function.



(a) The wave condition with a wave height of 0.04 m and a period of 1 second (H004T1). (b) The wave condition with a wave height of 0.13 m and a period of 7 seconds (H013T7).

Figure 4.8: The surface elevation of the measured wave for two wave conditions. The dashed lines show at which relative time with respect to the wave period  $T$  the velocity profiles are shown in figure 4.9

Figure 4.9 presents the vertical velocity and acceleration profiles for both wave conditions at  $t/T = 1/8$  and  $t/T = 3/8$ . The profiles of the fitted function and the non-linear extrapolation show similar values for the velocity and acceleration. The equations of the fitted function and the non-linear extrapolation are included in appendix H. However, they are underestimated compared to the Fenton theory, except for the vertical velocity profiles of figure 4.9c and 4.9g. The largest underestimations of velocity and acceleration are seen at the surface level. For example, the acceleration of the Fenton theory is 1.65 times larger than the acceleration of the extrapolated profile at the surface level for wave condition H004T1 (4.9d).

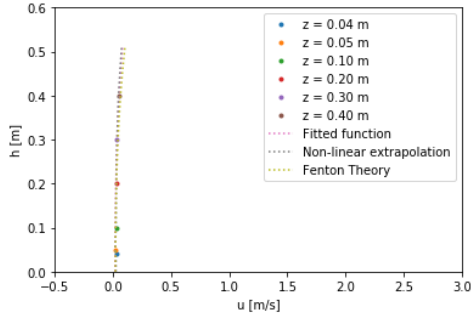
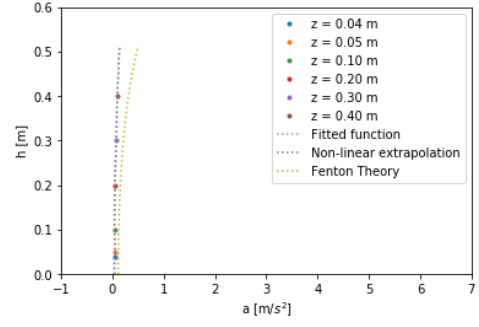
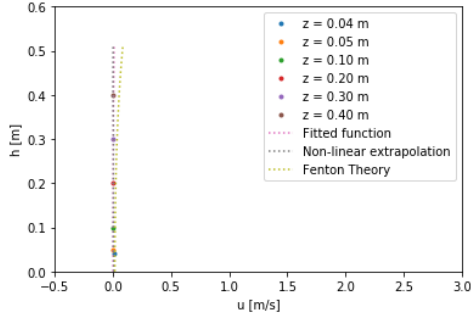
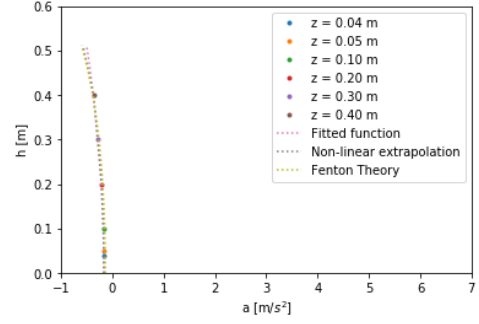
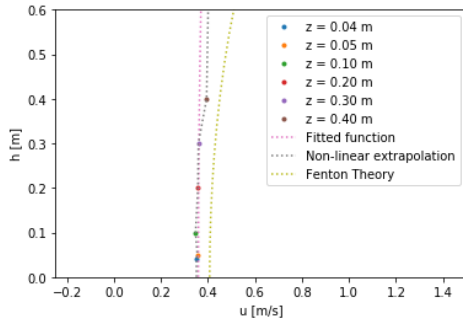
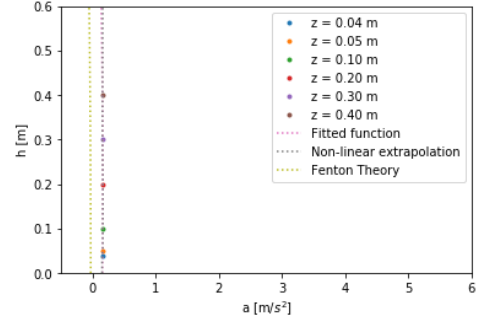
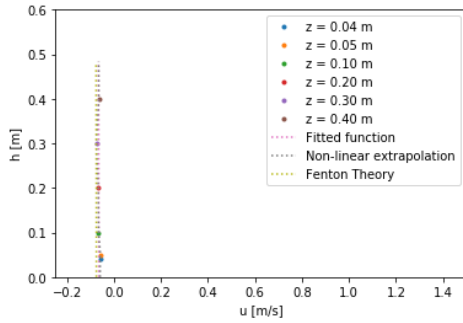
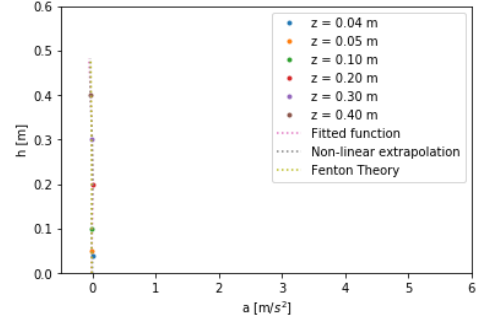
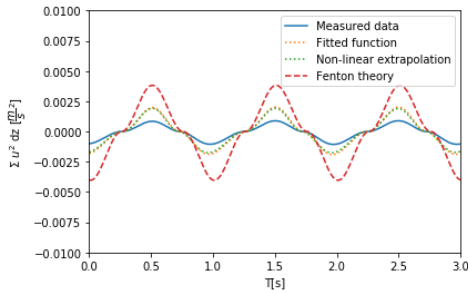
(a) Vertical velocity profile at  $t/T = 1/8$  for H004T1(b) Vertical acceleration profile at  $t/T = 1/8$  for H004T1(c) Vertical velocity profile at  $t/T = 3/8$  for H004T1(d) Vertical acceleration profile at  $t/T = 3/8$  for H004T1(e) Vertical velocity profile at  $t/T = 1/8$  for H013T7(f) Vertical acceleration profile at  $t/T = 1/8$  for H013T7(g) Vertical velocity profile at  $t/T = 3/8$  for H013T7(h) Vertical acceleration profile at  $t/T = 3/8$  for H013T7

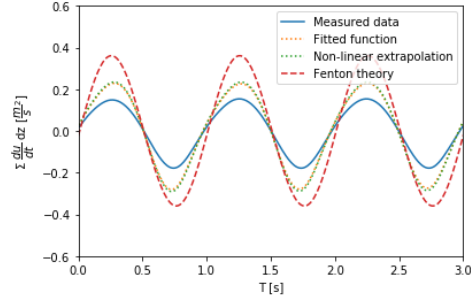
Figure 4.9: The vertical velocity and accelerations profiles at  $t/T = 1/8$  and  $t/T = 3/8$  of figures 4.8a and 4.8b. The points represent the mean measured velocity at  $z = 0.04$  m,  $z = 0.05$  m,  $z = 0.10$  m,  $z = 0.20$  m,  $z = 0.30$  m and  $z = 0.40$  m. The vertical velocity profile constructed with fitting a function through the points is presented with a pink dashed line called the fitted function. The vertical velocity profile constructed with non-linear extrapolation is presented with a grey dashed line called scaled. More information on the extrapolation of the profiles is included in appendix H. Lastly, the vertical velocity profile from Fenton is presented as a yellow dashed line.

### 4.3.3. Depth integrated velocity squared and acceleration.

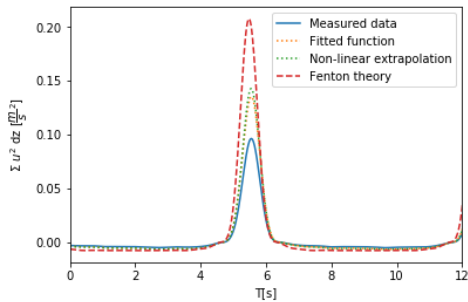
The drag and inertia coefficients are derived from the Morison equation (2.6) with the help of the depth-integrated velocity squared ( $U|U|$ ), depth-integrated acceleration and the surface elevation. The depth-integrated velocity and acceleration are obtained by integrating the fitting function over the depth and applying a discretized approximation based on the relative vertical distance between points. It must be noted that the figures show the depth-integrated velocity squared instead of the depth-integrated velocity. Figure 4.10 of the depth-integrated squared velocity and acceleration confirms the observation in section 4.3.2: the extrapolated and fitted function lines show similar values for the depth-integrated velocity squared and the acceleration, but their values are respectively 65 % and 45 % of the Fenton Theory.



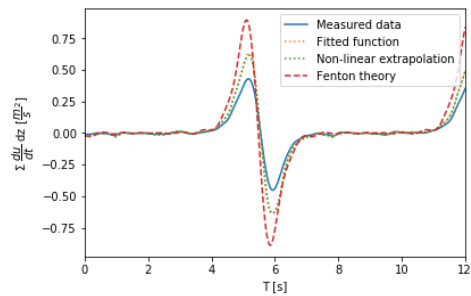
(a) Depth-integrated  $U|U|$  for H004T1



(b) Depth-integrated acceleration for H004T1



(c) Depth-integrated  $U|U|$  for H013T7



(d) Depth-integrated acceleration for H013T7

Figure 4.10: The depth-integrated velocity squared and acceleration is plotted over time for both wave conditions. The solid blue line shows the measured data, the dashed yellow line presents the line constructed with fitting a function through the points, the dashed green line shows the line based on the non-linear extrapolation and the dashed red line presents the Fenton theory.

#### 4.3.4. The drag and inertia coefficients

The last step of figure 4.5 is to solve the Morison equation (2.6) with the measured force, (equivalent) diameter, the depth-integrated  $U|U|$  and the depth integrated acceleration. The drag and inertia coefficients are derived using two different methods, namely the Least Squared method and the Maximum Likelihood method. This is to see if the method of solving has any influence on the results. The coefficients of the Least Squared method are obtained using different functions in Python: the Least Squared Method function and the function Curvefit. For each function, drag and inertia coefficients were derived using (1) the measured signals and (2) the signals estimated using Fenton. Figure 4.11 shows the results of the derivations for the wave conditions H004T1 and H013T7. The velocity was measured at six points over the height during the experiments. Therefore, six signals of the force are measured for every wave condition. The box plots show the variability of the six force signals. The derivation method does not seem to impact the results for drag and inertia coefficients significantly. However, the Maximum Likelihood for H013T7 shows more considerable variability than the Least Squared Methods, as seen in figure 4.11d. Also, the force coefficients are smaller when using signals estimated with Fenton than when using the measurements as input. This difference is likely due to underestimating the depth-integrated velocity and acceleration.

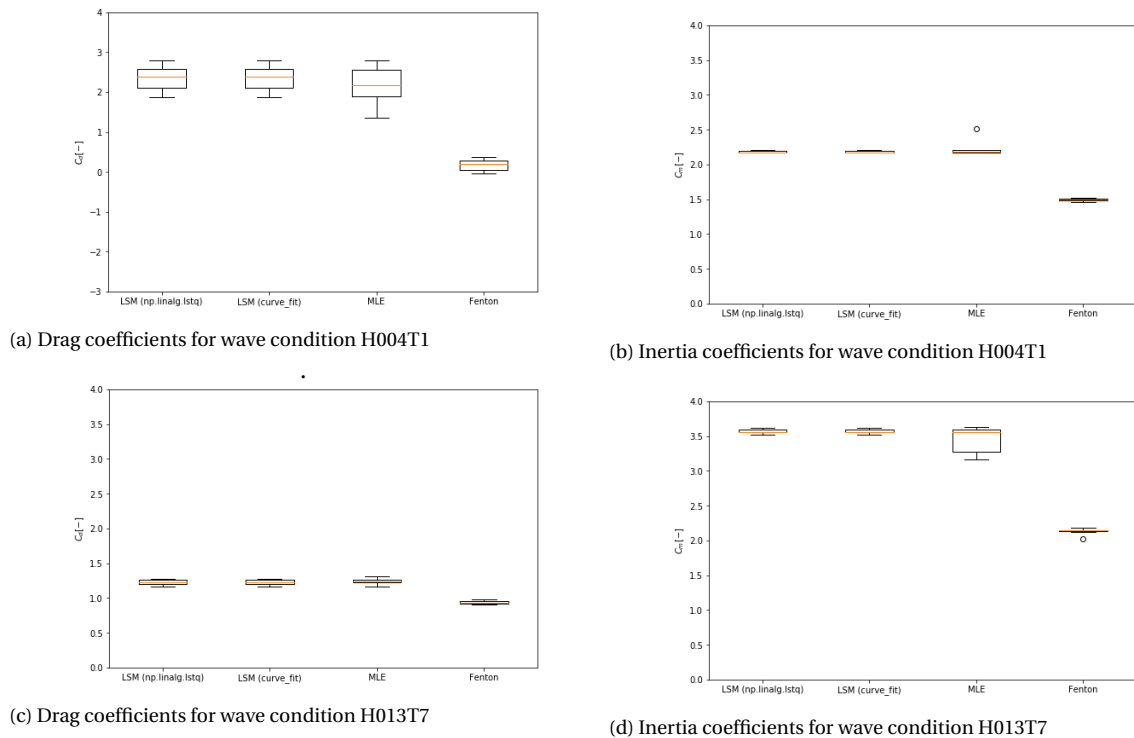
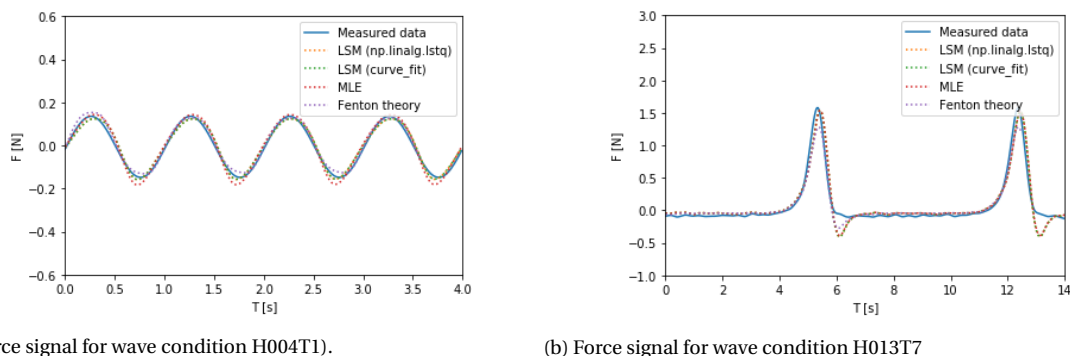


Figure 4.11: Drag and inertia coefficients are plotted for three different approach methods, namely the Least Squared Method with python function `np.linalg.lstsq`, the Least Squared Method with the fitted function and the Maximum Likelihood. Moreover, the obtained coefficients by using the Fenton theory are depicted. The variability of the box plots is due to the variability in the force signals. The velocity was measured at six points over the height during the experiments. Therefore, six signals of the force are measured for every wave condition.

Figures 4.12a and 4.12b show the fitted and measured force signals for wave conditions H004T1. All fitting methods agree with the measured signals except for a time interval just after the wave crest, where fitted forces exceed the measurements.

Figure 4.13 shows the results of the drag and inertia coefficients in three different ways. The first two figures (4.13a and 4.13b) present the coefficients fitted to time series with a length of 1 to 4 wave periods. The coefficients reveal significant differences compared to the literature, especially for the inertia coefficient of wave conditions H004T1, as shown in figure 4.13b. Figures 4.13c and 4.13d depict the results when the peak and trough of the wave are seen as two individual waves with their own period and wave amplitudes. The peak of the wave is defined as the area between a zero-up crossing and a zero-down crossing. Consequently, the trough of the wave is the area between a zero-down crossing and a zero-up crossing. For example, the peak of H013T7 has a much smaller period than the full wave,  $T_w = 1.67$  s instead of 7 s. The decrease in period is



(a) Force signal for wave condition H004T1).

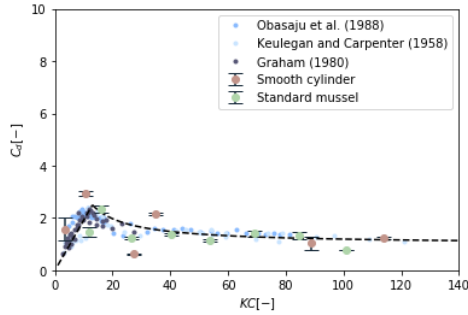
(b) Force signal for wave condition H013T7

Figure 4.12: The measured force signal (solid blue line) is presented with the force signal calculated with the obtained coefficients by the Least Squared Methods (dashed orange and dashed green line) and the Maximum likelihood (dashed red line). Moreover, the signal is compared to the Fenton theory (dashed grey line), solved with the Least squared method.

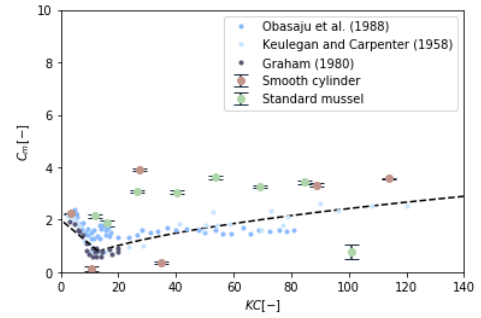
also reflected in the range of  $KC$  values. The coefficients reach only  $KC = 85$ , and most of the coefficients are located between  $KC = 5$ - 50 when the peak and the trough are separated. The drag and inertia coefficients show large variability and do not correspond with the literature. Lastly, figures 4.13e and 4.13f show the results when the parameters of the Fenton theory are used with the measured force. The Fenton theory best fits both the drag and inertia coefficients. However, not all the methods can be assumed to be reliable as the relative differences between the measured values are significant.

#### 4.3.5. Summary of results of the wave results

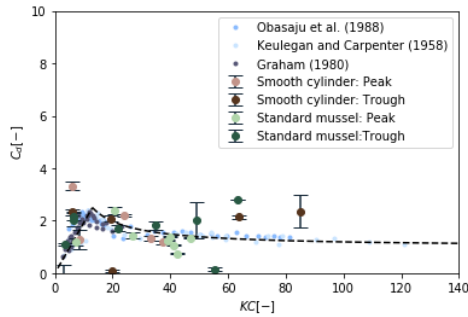
- The vertical velocity and acceleration profile are underestimated compared to the Fenton theory. The largest difference in velocity/acceleration is seen at the surface level. Consequently, the depth-integrated velocity squared ( $U|U|$ ) and acceleration are 35 % and 55% lower than the values of the Fenton theory.
- The drag and inertia coefficients are derived by solving the Morison equation. Results are shown for three different methods; 1) solving for the measured force, velocity and surface elevation, 2) solving for cnoidal waves that are split into two sinusoidal waves and 3) solving with the measured force and the velocity and surface elevation by the Fenton theory. The drag and inertia coefficients show large variability and  $C_{Ms}$  do not correspond with the literature. The best fit to literature was found for method 3.



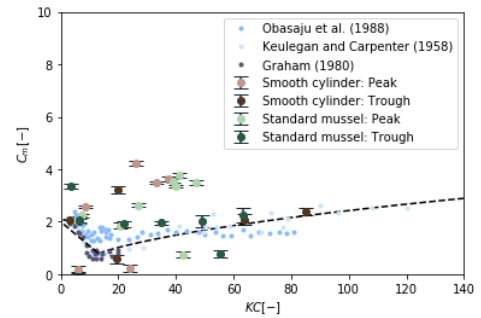
(a) Drag coefficients obtained for the full wave



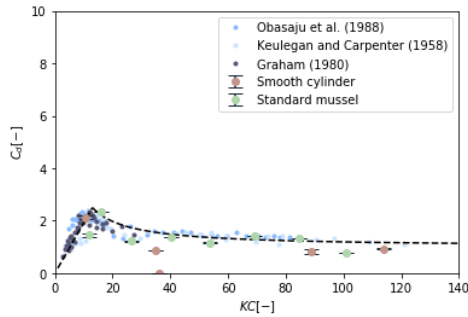
(b) Inertia coefficients obtained for the full wave



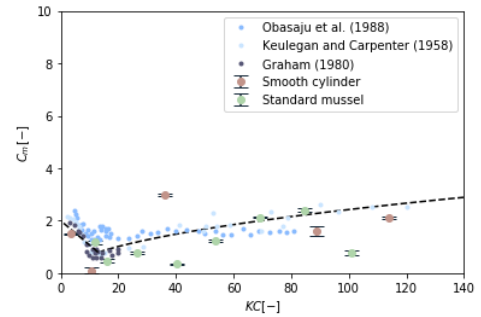
(c) Drag coefficients for separated peak and trough of the waves



(d) Inertia coefficients for separated peak and trough of the waves



(e) Drag coefficients for the derivation with the variables of the Fenton Theory



(f) Inertia coefficients for the derivation with the variables of the Fenton theory

Figure 4.13: The results are plotted together with data points of Obasaju et al.(1988), Graham(1980) and Keulegan and Carpenter (1958). Moreover, a line was plotted to fit the measurements (dashed black line). The variability of the data points is due to the variability in the force measurements.

# 5

## Discussion

This chapter reflects on the physical model, experiments' set-up, and the results. First, the physical modelling of the mussels is discussed in section 5.1. Next, section 5.2 elaborates on the outcome of the steady flow experiments and the derived drag coefficients. Lastly, section 5.3 discusses the performance of the wave experiments and the results of the drag and inertia coefficients.

### 5.1. Physical Model

This section discusses the physical model and its limitations.

#### 5.1.1. Mussel schematization

The mussel schematization presented in this study is less idealized than other studies from the literature, which used geometric shapes such as pyramids to represent mussels (Wolfram and Naghipour, 1999). Marty et al. (2021) also used physical models that emulated the mussel shapes observed, but their distribution followed a fixed pattern around the cylinder. In section 3.1.5, the images of mussel poles were analyzed to investigate the spatial distribution and orientation of the mussels in the field. It was observed that the mussels have a 45° or 90° difference with their neighbour for 52 % of the time and the rest of the time, the mussels have an average  $\pm 10^\circ$  difference. Moreover, the inclination of the mussel was influenced by neighbouring mussels. These three aspects were incorporated into a script and verified with different images of mussel poles. The presented method could be useful for future studies, however, more images should be analyzed to evaluate the generality of the observed patterns. Laboratory experiments should also compare homogeneously placed mussels and exact replicas of mussels to test how important it is to consider an accurate representation.

The physical model may also have limitations related to the derivation of the equivalent diameter, the uniform roughness height, and the fit of the mussel ring. Firstly, the equivalent diameter of the mussel cylinder is calculated by projecting the 3D model of the cylinder covered by mussels on a 2D plane and dividing the projected area by the cylinder height (section 4.1.1). However, the projected area includes the area of the mussels behind the first row of mussels. This suggests that the equivalent diameter is overestimated, and the drag coefficient is subsequently underestimated. Further research must be done on how to determine the equivalent diameter. Secondly, there is no variability in the roughness height of the mussels per ring. This is different from nature, where each mussel does not grow at the same rate at every height over the depth. This variability was investigated by Marty et al. (2021), where the mussels on a line having heights varying between 1.5 cm to 3 cm. Laboratory experiments should evaluate whether the variability in mussel height can be simplified by using a representative mussel size all over the cylinder. Lastly, the rings are attached to the cylinder with four screws. The rings of the standard and medium mussels had a perfect fit for the cylinders, but the large mussel rings did not fully close at the back of the cylinder. This leads to a larger equivalent diameter and thus an underestimation of the drag coefficient. An improvement on the ring for the larger mussels can be made by decreasing layer 3 so that the ring is less rigid and can be easier formed to the cylinder.

### 5.2. Measurements of the steady flow

This section describes the discussion on the measurements of the steady flow experiments. Firstly, in section 5.2.1 the difference between literature and the measurements is discussed. Next in the section 5.2.2, 5.2.3 and

5.2.4 the potential factors that can be the cause of any discrepancies are considered.

### 5.2.1. Measured drag coefficients

For steady flow experiments, two situations were tested. The first set of tests analyzed the forces on a smooth cylinder, the standard mussel and a cylinder with an equivalent diameter that represented the size of the standard mussels (section 3.2.3). A second set of experiments compared the smooth cylinder with the medium mussels and the large mussels. For the smooth cylinder, the measured drag coefficients followed a clear relationship as a function of  $Re$ . Drag coefficients decreased and converged to a constant value with increasing  $Re$ . However, the literature shows that drag coefficients for smooth cylinders converge to a value of 1, whereas the present measurements tend to have larger values of 1.49 and 1.74 (table 4.5) (White, 2006; Munson et al., 1994). Moreover, measured drag values increase for  $Re < 3000$ , whereas in the literature drag-enhancement due to viscous processes is observed for  $Re < 10$  (Sumer and Fredsoe, 1997). Considering a qualitative comparison between smooth cylinders and cylinders with mussels, the experiments show that the drag coefficient increases up to 66% when large-sized mussels are present on a cylinder. Such large differences between the smooth and mussel-covered cylinders are not found for the first set, while testing the same roughness height for a different scale. This finding suggests that the mussels with a roughness height of 0.36 cm (standard mussel and medium sized mussel) do not increase the drag coefficient compared to the smooth cylinders. A possible explanation for this might be that the physical model should have been scaled with the scaling length of the mussel instead of the diameter. By recalculating the  $Re$  numbers for the tested velocities with  $Re_x = k * U/v$ , it shows  $Re_x$  numbers between 86.4 and 864 for the standard mussel. For such  $Re$  numbers the drag coefficient increases rapidly, as seen figure 2.4. However, this hypothesis would not explain the high  $C_d$ s of the smooth cylinders. Therefore, this qualitative comparison should be reevaluated with new experiments where the  $C_d$ - $Re$  relationships of the single smooth cylinder agree with those of the literature. Moreover, new experiments should include a physical model scaled to the dimension of the mussel instead of the diameter. The differences between the drag measurements of this thesis and the literature may be due to inaccuracy in the velocity and force measurements. The performance of the EMF and force transducer and the steps done to assess their well functioning and accuracy are discussed below.

### 5.2.2. EMF performance during the steady flow experiments

The EMF height was changed between tests to record the velocity profile at five elevations over the water column. A higher vertical resolution was analysed in separate tests, where the velocity was recorded at 13 heights from the bottom. Depth-integrated velocities coincided with the values derived from 5 vertical points, suggesting that the vertical resolution for the velocity measurements was sufficient. The EMF sensor showed oscillations in the test, but these were addressed by earthing the sensors, keeping them submerged at night and cleaning them with alcohol. Moreover, the wave gauge next to the EMF interfered with the sensor; thus, it was turned off. This decreased the oscillation to a level that corresponds to reading accuracy but did not completely solve the problems. Therefore, the sensor offset was also analyzed, in case it was introducing an error in the measurements. Figure 5.1 shows the offset change on October 29 by comparing offset measurements collected in the morning, at noon, and the end of the day. The morning offset falls in the reading accuracy of 0.01 m/s, but this is not the case for the offset at noon and the end of the day. The changes in the EMF offset throughout the day may thus be a source of inaccuracy in the measurements because the step size of the steady flow experiments is in the same order of magnitude as the offset. Therefore, the offset of the EMF was measured every day at the start and the end of the day. The offset at noon was measured when the EMF showed significant oscillations during the morning. The cause and solution for these changes are unknown and should be further investigated by the manufacturer.

### 5.2.3. Performance of the force transducer during the steady flow experiments

The initial force transducer caused oscillation in the cylinder in the x and y-direction. Therefore, it was opted to use a more stiff force transducer. However, the new force transducer had a 0 - 98.1 N range, while the highest force had a value of 7 N. This means that the force transducer only used 7 % of the sensor range. An option was to use a larger amplification factor. However, this was not chosen because this would also increase the noise in the signal. Uncertainties appear in the measurements for waves with a wave height of 0.04 m. The force transducer showed a cascading signal due to limited discretization resolution, as seen in figure 5.2. This was solved by plotting a sinus function through the points, though this is not the exact measured signal.



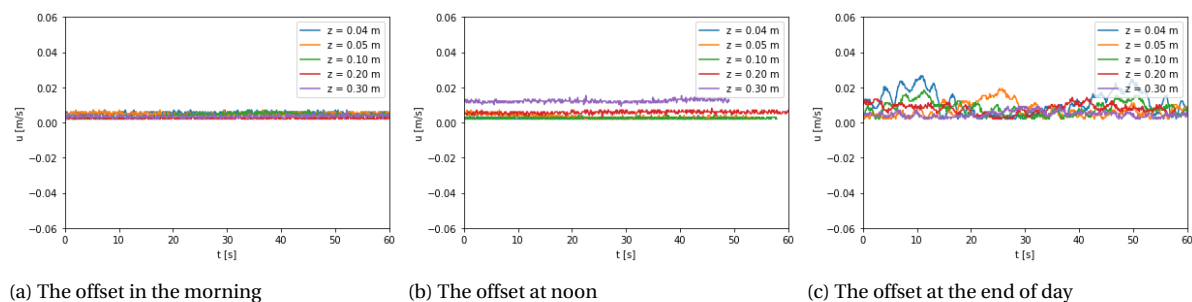


Figure 5.1: The EMF's velocity signal in still water at five different heights over the water depth. The signal is used as the offset for the velocity. This signal was measured on 29/10/2021. (a) presents the signal in the morning, (b) presents the signal at noon, and (c) presents the signal at the end of the day

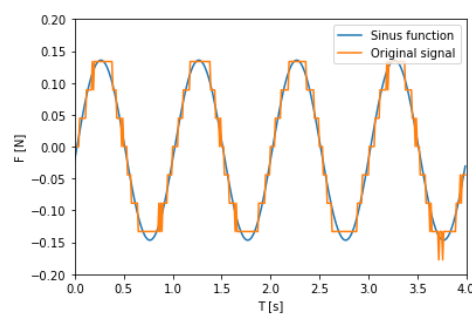


Figure 5.2: A comparison of the original output signal of the force (orange line) with the fitted sinus function (blue line).

#### 5.2.4. Determination of the flow velocity

The differences between the drag measurements of this thesis and the literature may be due to inaccuracy in the velocity and force measurements. The performance of the EMF and force transducer, and the steps done to assess their well functioning and accuracy are discussed below.

In the experiments of the steady flow (section 3.2.3), the aim was to test the drag forces on cylinders for currents that would result in Reynolds numbers between  $Re = 10^3 - 10^4$ . However, the steady flow was generated by manually adjusting a pump that did not provide discharge reading. During the data processing, it became clear that some velocities were higher than expected. This resulted in results that were not evenly distributed. One concern is that for the comparison of the scale 1:3, the smooth cylinder and medium mussel cylinder do not reach  $Re = 10^4$ . This gives an incomplete comparison with the large mussel cylinder.

### 5.3. Measurements on waves

This section describes the measurements of the wave experiments.

#### 5.3.1. Observations of the drag and inertia coefficient

Measured drag and inertia coefficient were obtained in several ways. The best agreement with the literature was obtained when the measured forces were fitted with velocities estimated using Fenton, rather than with the measured velocities. When the recorded velocities and accelerations were used, the drag coefficient seemed to fall in the range of previous findings by Obasaju et al. (1988), Graham (1980) and Keulegan and Carpenter (1958). However, the inertia coefficients are higher than expected from the findings by the same authors. As mentioned in the literature review, Nath (1982) did find  $C_M$  values of 2.8 and 2.5 for cones with similar relative roughness as the standard and large mussels. However, the largest inertia coefficients are seen for  $KC > 20$  and not for  $KC = 5$  and 12. Higher  $C_M$  values were reported by Theophanatos and Wolfram (1989), who show values of  $C_M = 2.24-2.59$  for macro-roughened cylinders with a  $k/d$  of 0.098. However, they state that inertia forces measured are not fully representative of those obtained in wave and planar oscillatory flows since the returning wake effects are not present (Theophanatos and Wolfram, 1989). Surprisingly, Marty et al. (2021) found inertia coefficients of 1.4 and 1 for  $KC = 3$  in their experiments, while also using a realistic model instead of cones or pyramids. They suggested that a realistic shape for mussels appears to change the inertia coefficient drastically. That finding is contrary to the results of this study which did not found a drastic

decrease in the inertia coefficients for  $KC$  numbers around 3.

The data processing also evaluated whether the fact that waves were cnoidal (and thus had asymmetric surface elevations and velocities) was affecting the drag coefficient by comparing the fitting of the coefficients over (1) a full wave period, (2) the trough of the wave, and (3) the crest of the wave. One concern could be that a cnoidal wave, a highly non-linear wave, could not be represented with a single  $KC$  number, as the drag and inertia coefficient could vary during the wave cycle. Namely, the definition of the  $KC$  number is based on a single velocity magnitude, under the assumption that the wave-driven velocities are sinusoidal. However, figures 4.13c and 4.13d did not show a better fit for the literature. It must be noted that studies by Sarpkaya (1986), Keulegan and Carpenter (1958) investigated horizontal cylinders underwater with simple sinusoidal currents. The mismatch with the literature, when using measurements, can also be due to underperformance of the EMF (see section 4.3.3). Other potential factors could be related to underestimating the velocity profile, the eigenfrequency of the smooth cylinder, and the wave's phase velocity.

Firstly, the underestimation of the velocity profile is discussed. Figure 4.9 shows the vertical velocity and acceleration profile. It can be concluded that the profiles are underestimated compared to the Fenton theory. The differences between the measured and the literature are even more evident in figure 4.10, which depicts the depth-integrated velocity squared and acceleration. Figures 4.13e and 4.13f show the results if the depth-integrated velocity squared and acceleration of Fenton theory are used with the measured force measurements. These results seem to agree better with literature values for the drag and inertia coefficients. However, still, a large spread of data points can be seen.

Secondly, the phase velocity may explain the spread of the data. As explained in section 3.4.3, the phase velocity was calculated by determining the time shift between the signals of wave gauges 1, 2, 3 and 4. However, the phase velocity is not consistent over the length of the flume and has been increasing for most of the experiments. This gives uncertainties in the time shift of the signals of different instruments. These phase differences are minor for the wave conditions of H004T1 and H013T7, as seen in figure 4.10. However, for wave condition H004T2, the phase difference is significant, and the inertia coefficient changes significantly (figure 5.3). It could be speculated that this confirms that the largest uncertainty is in the velocity signals.

Another source of uncertainty is the eigenfrequency of the smooth cylinder for high  $KC$  numbers, which can play a role in the results. Appendix F elaborates on the choice of the filter for the force signal. It aims to dismiss the interference of the oscillations by the smooth cylinder. Therefore, the average value of the oscillation is taken as default. However, the peak or trough of the oscillation could also be the real force signal. This would result in a peak with a longer or a shorter period and thus affect the coefficients.

It remains unclear to which degree each factor attributed to the mismatch or whether this could be the case at all. A cautious conclusion that can be made is that there is an insignificant difference between the smooth and standard mussel provided the accuracy of the experimental method. This was already reflected in the steady flow experiments. Moreover, more experiments with the designed physical models are required to refute the results of Marty et al. (2021) and verify the results of this study. It is important that the velocity is correctly measured and therefore it is needed to have multiple types of velocity meters.

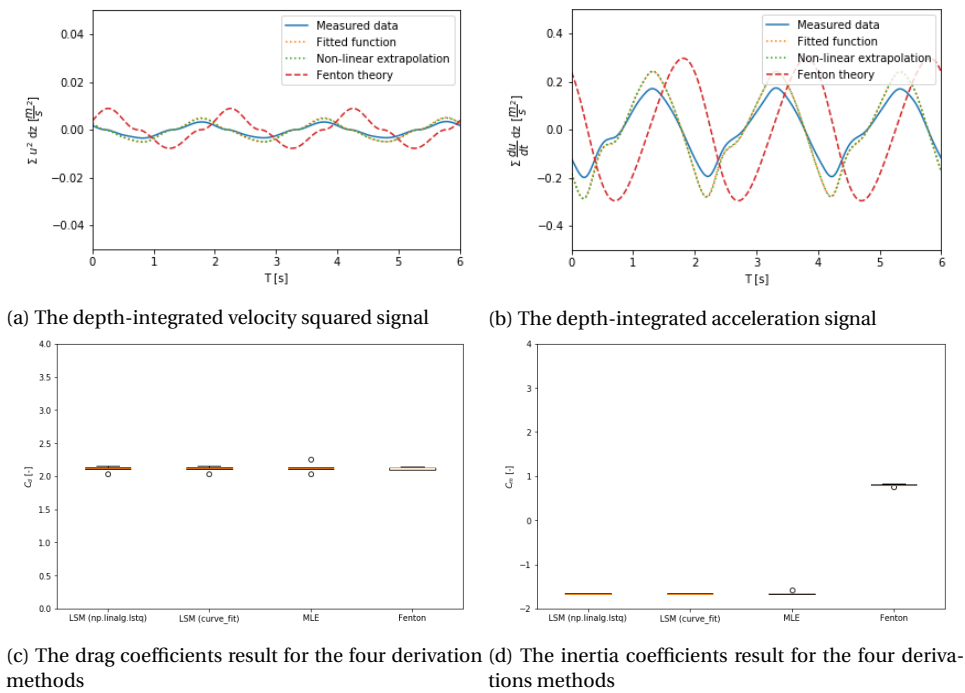


Figure 5.3: The signals of wave condition H004T2. The blue line presents the measured data, the dashed orange and green lines represent the fitted function and non-linear extrapolation of the velocity profiles. The signals are compared with the Fenton theory (dashed red line). The results of the coefficients are presented with box plots. The error bars indicate the variability in the force measurements.

# 6

## Conclusion and recommendations

### 6.1. Conclusion

The present research aims at describing and quantifying the effect of mussels on vertical poles in currents and under waves.

#### 6.1.1. Sub-questions

The following sub-questions are answered to support the main research question:

**1. How can mussels in small-scale experiments be schematized?**

The growth of Green Asian mussels on bamboo poles was schematized as mussel rings consisting of three parts, namely roughness elements, an impermeable layer and an extra thickness. The mussel rings were printed by a 3D printer and multiplied by resin casting. The present study improves on existing knowledge by using well-described model mussels with realistic shapes, orientation and distribution. In contrast, previous studies assumed simplified shapes and uniformly arranged orientations. This new way of realistic modelling should help predict the effect of the growth of mussels. However, further study should assess the importance of the distribution by comparing it to a uniform distribution.

**2. What is the effect of mussels on the hydrodynamic forces of a vertical pole in a current?**

While this study did not exactly agree with the commonly found drag coefficients for smooth cylinders, it partially substantiated mussels' effect on the hydrodynamic forces of a vertical pole in a current. The experiments have shown a significant relative difference between the drag coefficient of the large mussels cylinder and the smooth cylinder. These findings show a 50-66 % increase for  $Re = 4000-6000$  compared to the smooth cylinder. The differences in drag coefficients of the standard mussels and the large mussels, despite having the same relative roughness, suggest that the roughness height of the standard mussel is too small for investigating the effect of mussels. This could also be confirmed by the results of the medium mussel cylinder, where the drag coefficient also has a negligible difference from the smooth cylinder. Recalculating the  $Re$  numbers for the mussel size, instead of the diameter, shows  $Re = 10^2 - 10^3$ , where the drag coefficient is higher than between  $Re = 10^3 - 10^4$ . However, this does not justify the high drag coefficient numbers of the smooth cylinder. Therefore, laboratory experiments should be redone with models scaled to the size of the mussel and multiple types of velocity instruments to establish this hypothesis. The inaccuracies in the results might also stem from EMS recordings.

**3. Is the drag crisis likely to be relevant for a bamboo pole with mussels in the field?**

A hypothesis would be that the drag coefficient crisis for cylinders with mussels are located in the range of  $Re = 10^3 - 10^4$ . For example, the drag coefficient crisis for  $\frac{k}{D} = 0.03$  had a decrease of 0.5. Nevertheless, the experiments did not detect any clear evidence of a drag crisis in this range of  $Re$  numbers. It is unclear whether this means that the drag crisis became negligibly small due to an increase in relative roughness or that the drag crisis takes place outside the  $Re$  values tested in this study. The results

provide evidence that the drag coefficient for the tested wave conditions is not in a regime with a drag crisis.

#### 4. What is the influence of mussels on the hydrodynamic forces of a vertical pole in waves?

The findings on the influence of mussels on hydrodynamic forces on a vertical pole in waves are highly uncertain. The drag coefficients shows good correspondence with the literature for smooth cylinders, but the inertia coefficients do not. Moreover, no relative differences between the smooth and standard mussel cylinders are found. The experiments with steady flow already showed this. The calculated drag and inertia coefficients showed better agreement with literature when velocities estimated with Fenton were used as an input value. This suggests that forces are correctly measured and that the inaccuracies may stem from the EMS recordings. This study has shown similar increase in inertia coefficients as for cones and pyramids, but has contradictory results to literature with similar realistic modeling. Further work is needed regarding the inertia coefficients and the uncertainty due to underestimating the velocity profile, the phase velocity or the distance between the instruments, and the cylinder's eigenfrequency.

#### 5. Can the drag coefficient of cnoidal waves be linked to the Keulegan-Carpenter number, as it is done for the linear waves?

Cnoidal waves are highly non-linear and behave differently than sinusoidal waves, which has been the subject of extensive research. Parameters such as the  $KC$ ,  $C_d$  and  $C_M$  have been developed assuming sinusoidal waves, where the positive and negative parts of the wave cycle have similar velocity magnitude. The wave cycle of a cnoidal does not consist of a similar peak and trough but consists of high and short peaks and long and shallow troughs. Therefore, in the data analysis waves were split into two separate parts: waves and troughs. By fitting the drag and inertia coefficients separately for the crest and the trough, the variability of  $C_d$ ,  $C_M$ , and  $KC$  of the wave cycle could be evaluated. Drag and inertia coefficients had comparable values for the different parts of the wave cycle, suggesting that the force coefficients of cnoidal waves can be linked to the  $KC$  numbers, as it is done for linear waves. Nevertheless, it is recommended to do further research on this topic due to the uncertainties in the laboratory measurements. Wave attenuation by cnoidal waves can be estimated by integrating the wave flow velocities from Fenton theory, using drag coefficients measured in flume experiments.

### 6.1.2. Main research question

With the help of the sub-questions, the main research question can be answered:

**How does the growth of the mussel, *Perna Viridis*, on vertical bamboo poles affect the physical processes driving wave dissipation for different wave conditions?**

This thesis has provided deeper insight into the effect of mussel growth with a  $k/D$  of 0.1 and 0.06 on vertical bamboo poles for a steady flow and a large range of wave conditions ( $KC = 3-113$ ). For currents, the drag coefficients with mussels increased 66% in the range of  $Re = 10^3 - 10^4$ , whereas for waves, the differences in drag coefficients were almost negligible. The presence of mussels increases the diameter up to 63%, for the maximum mussel size expected in Demak. The relative difference between the smooth and the mussel cylinder and the increase of the diameter indicates the effect of wave attenuation. The wave attenuation by cnoidal waves can be estimated by integrating the wave flow velocities from Fenton theory, using drag coefficients measured in the flume experiments. Nevertheless, it should be taken into account that the data analysis identified inaccuracies in the velocity measurements, which may be influencing the previous results.

## 6.2. Recommendations

The most important recommendations for further research are:

1. Further experimental investigations with the physical model should be done using the 1:3 scale model. This scale showed significant differences between the smooth and mussel cylinders. Moreover, a scale model should be designed using the mussel size as scaling length. Measuring with two different devices instead of one is recommended, due to reoccurring problems with the velocity signals,

2. Further laboratory experiments should be done to verify the use of realistic modelling. The physical model of this thesis should be compared to homogeneously placed mussels and mussel pole replicas to quantify the difference in drag coefficients.
3. Numerical modelling should be done to assess the effect of mussel growth on wave attenuation. With the drag coefficients measured for single cylinders in the flume experiments, the effect of a bamboo pole field can be assessed. The longitudinal and transversal length between each bamboo pole must be at least  $5D$ , so the poles do not interact. By changing the field's length, the water depth, and the longitudinal and transversal distance, a bamboo field can be designed that satisfies the aim to attenuate 60 % of the wave energy for mangrove rehabilitation.
4. It should be investigated whether it is economically feasible to implement the bamboo field. Factors that should be included are labour costs, material costs of the structures, sales price and transport costs.

# A

## Mussel pattern

### A.1. Dimensions

The dimensions are based on six images from the internet, as seen in A.1. A blue outline, based on mussel number 1, is placed over the other five mussels. This was done to verify that green Asian mussels have similar shapes. Moreover, the outline was used to determine the height, width, thickness and height from the widest point. The definitions of the measured parameters are shown in figure A.2.



(a) Mussel number 1



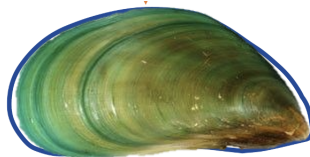
(b) Mussel number 2



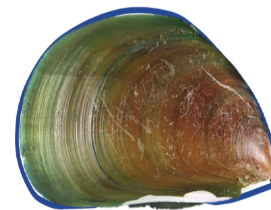
(c) Mussel number 3



(d) Mussel number 4



(e) Mussel number 5



(f) Mussel number 6

Figure A.1: Six images of mussels. A blue outline of mussel number 1 is shown around the other five mussels to verify that the mussels have similar shape.



(a) Front view of the mussel. The outline gives an indication of where the height, width and height from the widest point are measured.

(b) Side view of the mussel. The outline gives an indication of where the thickness is measured.

Figure A.2: The definitions of the measured parameters.

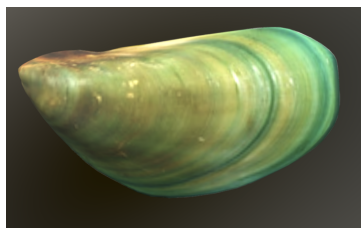
The values of the parameters of the six images are depicted in table A.1. The values are the dimensions in the field. Next, the average dimensions are calculated for the design mussel. The height, width, thickness and height from the widest point are 5 cm, 2.4 cm, 1.5 cm and 2.3 cm, respectively. The dimensions are scaled down to a scale of 1:6 and 1:3, as shown in table 3.1.

Table A.1: Averaged dimensions in the field in cm

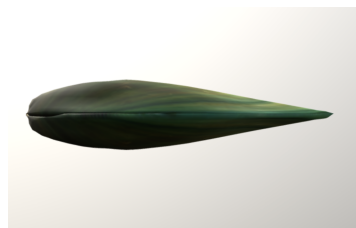
Number	Height	Max width	Thickness	Height from the widest point
1	5	2.3	-	2.2
2	5	2.3	1.6	2.2
3	5	2.3	-	2.4
4	5	2.4	1.4	2.3
5	5	2.6	-	2.2
6	5	2.4	1.5	2.2
Average	5	2.4	1.5	2.3

## A.2. Realistic shape

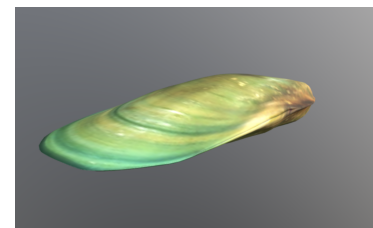
The shape of the design mussel is based on a realistic 3D model taken from the site Sketchfab. The impressions of the 3D model can be seen in the figure A.3. The 3D model is scaled down to the desired dimension of table 3.1.



(a) Front view of the mussel of the 3D model.



(b) Side view of the mussel of the 3D model.



(c) Side view 2 of the mussel of the 3D model

Figure A.3: Three sides of the 3D model.

## A.3. Mussel pattern

Images from the field were used to understand the natural position of the mussels and to recreate their pattern. First, a red square was drawn to define a fixed area, as can be seen in figure A.4.

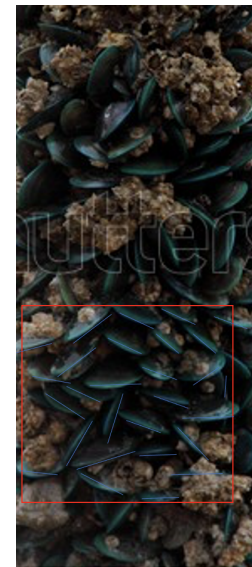




(a) Image from the field.



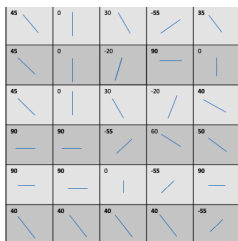
(b) Image from the field.



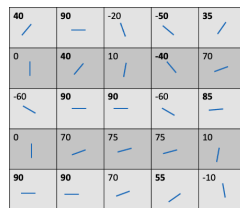
(c) Image from the internet to verify the pattern.

Figure A.4: Three images from the field. The red box defines a fixed area, where the position of the mussel are investigated.

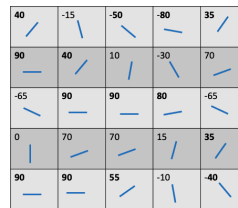
From the red square figure A.4, the angles are determined and placed in a grid. This can be seen in the figure A.5. There were two option in the translation of figure A.4b to a grid. Therefore, figures A.5b and A.5c are both based on figure A.4b.



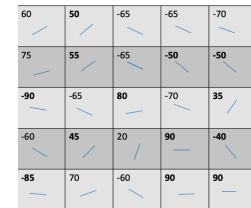
(a) Pattern from A.4a



(b) Pattern from A.4b



(c) Pattern from A.4b



(d) Pattern from A.4c

Figure A.5: Three sides of the 3D model.

Now that the patterns of the three images are simplified and established in grids, an analysis is done. The following aspects were researched:

1. The averaged angle between the mussels, counted in the rows of the grid (deviation X)
2. The averaged angle between the mussels, estimated in the columns of the grid (deviation Y)
3. The number of mussels next to each other with the same angle (pairs)
4. The number of mussels that had an angle of 45 degrees or 90 degrees with its neighbour (in both directions) with a 10-degree range (# of angles).

From all this, it was concluded that the mussels have an average angle of 10 °difference from their neighbour. Also, 51 % of the mussels have a 45°or 90°angle with their neighbour. The values are presented in table A.2.

Table A.2: Analysis of the simplified patterns. Version A is figure A.5a, version B is figure A.5b, version C is figure A.5c and version D is figure A.5d

Version	Deviation X [°]	Deviation Y [°]	Pairs [-]	# of angles [-]
A	$160/24 = 7$	$145/25 = 6$	13	$16/30 = 0.53$
B	$230/20 = 11.5$	$240/20 = 12$	3	$12/25 = 0.48$
C	$190/20 = 9.5$	$240/20 = 12$	3	$14/25 = 0.56$
D	$250/20 = 12.5$	$260/20 = 13$	5	$12/25 = 0.48$
Average	10.125	10.75	4	$77/150 = 0.51$

## A.4. Python Script

The Python script that is used to generate the mussel pattern is included. First, an empty matrix with the size of 4 by 13 was constructed. Then random locations were determined for the 45 °or 90 °angle. Next, the average of 10 °with their neighbouring mussels was included in the pattern.

```

1 from random import randint
2 import random
3 # step 1: empty matrix
4 a = 4 #rows
5 b = 13 #columns
6 factor = 0.51 #percentage of mussel that have 45 degree of 90 degree with their
   neighbour
7 n = round(a*b*factor)
8 mussel_matrix = np.zeros((a,b)) #matrix for the mussel
9
10 #step 2: find random locations
11
12 array_1 = np.arange(0,a)
13 array_2 = np.arange(0,b)
14 comb_array = np.array(
15 np.meshgrid(array_1, array_2)).T.reshape(-1, 2)
16 new_array = shuffle(comb_array, random_state = 0)
17
18 x = new_array.shape[0]
19 random_indices = np.random.choice(x, size=n, replace=False)
20 random_rows = new_array[random_indices, :]
21 #print(random_rows)
22 row1 = random_rows[:,0]
23 row2 = random_rows[:,1]
24
25 #step 3: include the random location in the empty matrix and give them an random angle
   45 degree
26
27 for y in range(len(row1)):
28     mussel_matrix[row1[y], row2[y]] = random.randrange(45,271, 45)
29
30
31 # Step 4: start with a random point in [0,0]
32 mussel_matrix[0,0] = random.randrange(0,361,10)
33
34 #step 5: angle of the mussel depending on the neighbouring mussel + range of 10 degree
   difference with the neighbour + value given by step 2 (can be 0, 45, 90)
35 #for the rows
36 for i in range(a-1):
37     mussel_matrix[i+1,0] = (mussel_matrix[i,0]+ random.randrange(-10,11, 10)+
   mussel_matrix[i+1,0])%360
38 # for the columns
39 for j in range(b-1):
40     mussel_matrix[0,j+1] = (random.randrange(-10,11,10) + mussel_matrix[0,j+1] +
   mussel_matrix[0,j])%360
41
42 # step 6: fill the rest of the matrix with: the mean of the angle of the mussel above
   and next to the mussel + range of 5 degree difference with the neighbour + value
   given by step 2 (can be 0, 90, 270)
43 for i in range(a-1):
44     for j in range(b-1):
45         neighbour = (np.int((mussel_matrix[i,j+1] + mussel_matrix[i+1,j])/2))%360

```

```

46     mussel_matrix[i+1,j+1] = (5*round(neighbour/5) +random.randrange(-10,11,10) +
47     mussel_matrix[i+1,j+1]) %360
48 #step 7: Give an angle between -180 and 180 degree instead of between 0 and 360
49 k = mussel_matrix[0,:]
50 j = mussel_matrix[1,:]
51 e = mussel_matrix[2,:]
52 a = mussel_matrix[3,:]
53 for i in range(len(k)):
54     if k[i]>180:
55         k[i]= k[i] -360
56     if j[i]>180:
57         j[i]= j[i] -360
58     if e[i]>180:
59         e[i]= e[i] -360
60     if a[i]>180:
61         a[i]= a[i] -360

```

Listing A.1: Mussel pattern

## A.5. Verification

The outcome of the Python script was check and and verified by using other sections of the previous used images.

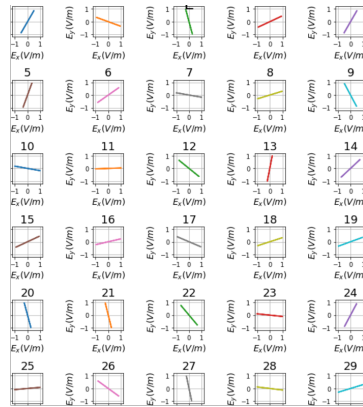


Figure A.6: Outcom of the python script

# B

## Instruments

## B.1. Details on wave height meters



*Instrument*

### Wave height meter

The wave height meter is developed for measurement of dynamically varying liquid levels, wave heights of water in particular. The wave height meter can be used as a standalone probe or combined with a control unit. The main difference when using a control unit is the ability to adjust the gain and zero shift of the output signal by means of dials. Furthermore, the control unit provides the probe with power. The output signal for the surface elevation is analogue for both the standalone version as the control unit.

#### Applications

The wave height meter is, amongst others, used for laboratory research in the fields of:

- wave penetration in harbours
- performance of breakwaters and dikes
- coastal protection
- load and stability of off-shore structures

#### Probe

The probe of the wave height meter is constructed of two parallel stainless steel rods, mounted underneath a small box. This box contains electronics for sensor excitation, signal detection, amplification and galvanic isolation. The rods act as the electrodes of an electric conduction meter. A platinum reference electrode is included to compensate the surface elevation measurement for the effect of varying electrical conductivity of the fluid. The analogue output signal is linearly proportional to the liquid level between the sensor rods.

#### Features

- fast dynamic response
- wide range 0.5 m, other ranges optional
- automatic compensation for conductivity variation
- high linearity
- easy installation
- analogue output indication on control unit





## Deltares

Instrument, Wave height meter, version 1.1

### Technical specifications

Wave height electrodes	<ul style="list-style-type: none"> <li>rods, stainless steel, type 316, 4 mm diameter</li> <li>electrode spacing 24.3 mm</li> <li>electrode length 590 mm (other lengths optional)</li> </ul>
Reference electrode	platinum
Other materials exposed to liquid	PVC-U
Liquid medium	<ul style="list-style-type: none"> <li>medium conductive liquids non-aggressive to mentioned materials</li> <li>minimum required conductivity 0.1 mS/cm</li> <li>sensitivity variation &lt; 1 % for 0.1 to 2.0 mS/cm</li> </ul>
Accuracy	0.5 % of measuring range, best straight line
Output	0.4 V/cm level variation (standard: -10 to +10 VDC for 50 cm liquid level change)
Frequency response	> 15 Hz
Dimensions	incl. electronics 675 mm long (standard length)
Cable	25 m (optional up to 100 m)

### Control unit

The control unit supplies the wave height meter with power and provides a way to adjust the wave height meter to the desired calibration. Four switch selectable ranges are available to adjust the gain of the output signal. The zero level is adjustable by a dial. One universal carrying case (UCC) can support two control units.

### Features

- output indication
- switch selectable ranges
- adjustable zero level
- can be used with probes of various length

### Technical specifications

Probes available	standard probe 0.5 m range special probe 1.0 m range other lengths on request
Ranges	0.05, 0.1, 0.2, 0.5 m for standard probe 0.1, 0.2, 0.4, 1.0 m for special probe
Frequency response	> 15 Hz
Output	+/- 10 VDC
Dimensions cassette	standard eurostyle cassette

Several configurations can be built on request. One example is a setup where a number of wave height meters without control units are powered by one electronics box. For each wave height meter the analogue output signal is available on a BNC connector. Furthermore, there is the possibility to include data output over USB or Ethernet.



probe



Control unit front view



Control unit rear view

More information: [instrumentation@deltares.nl](mailto:instrumentation@deltares.nl)

## Deltares

PO Box 177  
2600 MH Delft, The Netherlands  
T +31 (0)88 335 82 73  
[info@deltares.nl](mailto:info@deltares.nl)  
[www.deltares.nl](http://www.deltares.nl)

*Deltares is an independent institute for applied research in the field of water, subsurface and infrastructure. Throughout the world, we work on smart solutions, innovations and applications for people, environment and society. Deltares is based in Delft and Utrecht.*

(Deltares, 2022b)

## B.2. Details on electromagnetic velocity meter



*Instrument*

### Programmable electromagnetic liquid

### velocity meter

The electromagnetic velocity meter measures bi-directional water velocity in two perpendicular directions. The measurement principle is based on conductive liquid moving through a magnetic field. The magnetic field is induced by electrical current in a small coil inside the body of the probe. Two pairs of diametrically opposed platinum electrodes sense the induced voltages produced by the flow past the probe. The probe has been designed in such a way that these voltages are proportional to the liquid velocity parallel to the plane of the electrodes.

#### Applications

Specific applications where the electromagnetic liquid velocity meter can be used include:

- laboratory research
- engineering studies
- open channel stream gauging
- slurries and sludge transport
- environmental and hydrological measurements
- sedimentation and filtration processes
- flow monitoring under surge conditions

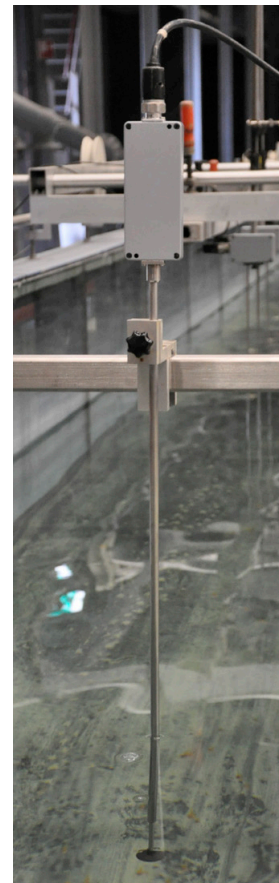
#### Standard probes

There are two standard probes available. The E30 type probe is especially suitable for physical model studies and laboratory research due to its smaller probe size. The E40 type probe has a larger probe size and is therefore more robust. Furthermore, the E40 type probe can be fully submerged in liquid, as opposed to the E30 type probe. Next to these two standard probes, special probes (e.g. cranked) can be made to suit specific applications.

As described above, the probes measure the liquid velocity using a magnetic field beneath the probe. This magnetic field should not be disturbed. The probes have to be connected to a control unit.

#### Features

- 0 - 2.5 m/s bi-axial four quadrant range
- towing tank calibration
- < 10 mm/s per 24 hours zero stability
- ellipsoid type probes for high spatial resolution and minimum flow disturbance
- galvanic isolation between probe and output





## Deltares

Instrument, Programmable electromagnetic liquid velocity meter, version 1.1

### Technical specifications

Materials exposed to liquid	<ul style="list-style-type: none"> <li>stainless steel 316</li> <li>platinum</li> <li>PU finish 03-69554 Ral 9021 F9</li> </ul>
Medium	<ul style="list-style-type: none"> <li>liquids and suspensions, including slurries</li> <li>minimum required conductivity 0.2 mS/cm</li> <li>maximum temperature 40°C (water)</li> </ul>
Probe	<ul style="list-style-type: none"> <li>electromagnetic, bi-axial, 4-quadrant</li> <li>E30 type: ellipsoid 11x33 mm, total length 1090 mm, immersion depth 850 mm</li> <li>E40 type: ellipsoid 14x40 mm, total length 500 mm, fully immersible (max. 30 m)</li> <li>special probes available on request (e.g. cranked probe)</li> </ul>
Range	up to 2.5 m/s (E40 type optional up to 5.0 m/s)
Accuracy	+/- 0.01 m/s +/- 1 % of measured value
Tilt response error	negligible for tilt angles < 10° if compensated for cosine response
Temperature influence	<ul style="list-style-type: none"> <li>medium: &lt; 1.0 mm/s per °C</li> <li>ambient: &lt; 0.3 mm/s per °C</li> </ul>
Conductivity influence	< 0.02 % of reading per mS/cm
Cables	<ol style="list-style-type: none"> <li>E30 type: 10 m (optional up to 100 m)</li> <li>E40 type: 25 m (optional up to 100 m)</li> </ol>

### Control unit

The control unit for the electromagnetic liquid velocity meter can be used with different types of probes. Its various functions can be controlled by three keys on the front panel. The control unit is able to communicate in ASCII coded messages (text) via the RS-232c port with a PC, terminal, etcetera. Measurements can be programmed and data collected at distance from the control unit (data handling software is not included).

### Features

The following features can be selected from the control unit:

- Vx and Vy or magnitude and direction
- display in volts or m/s
- actual or average data, standard deviation of values measured
- continuous or single measurement
- averaging time 0.1 - 9999.9 s
- probe type
- baud rates from 1200 to 9600
- zero calibration
- synchronization to mains

### Technical specifications

Range	0 to +/- 1.0 or +/- 2.5 m/s optional 0 to +/- 2.0 or +/- 5.0 m/s
Output	analog voltage 0 to +/- 10 V, range selected, short circuit proof RS-232c port for data transfer to PC
Measuring period	by menu, continuous or single period
Averaging time	By menu, 0.1 - 9999.9 s
Dynamic response (70%)	7 Hz
Dimensions cassette	standard eurostyle cassette



E40 probe

E30 probe



Control unit front view



Control unit rear view

More information: [instrumentation@deltares.nl](mailto:instrumentation@deltares.nl)

## Deltares

PO Box 177  
2600 MH Delft, The Netherlands  
T +31 (0)88 335 82 73  
[info@deltares.nl](mailto:info@deltares.nl)  
[www.deltares.nl](http://www.deltares.nl)

*Deltares is an independent institute for applied research in the field of water, subsurface and infrastructure. Throughout the world, we work on smart solutions, innovations and applications for people, environment and society. Deltares is based in Delft and Utrecht.*

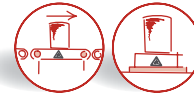


### B.3. Details on force transducer

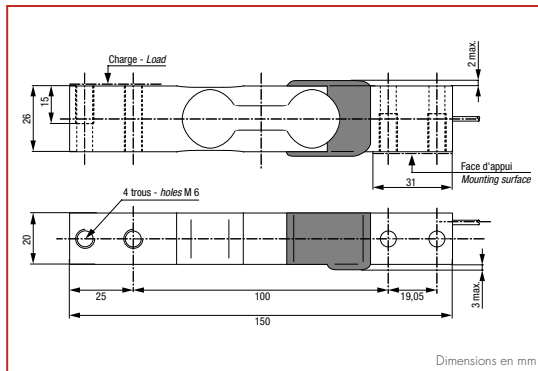
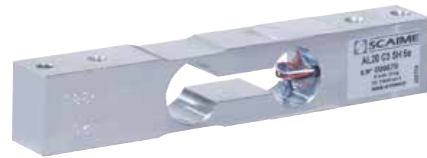
Load cell - Single point

# AL

3 kg ... 30 kg



- Aluminum construction, protection class IP65
- 3 000 d OIML R60 and 5 000 d NTEP approved
- Off-centered load compensated
- Low cost model for high volume production



+ Excit.: Red | + Sign.: Black | - Sign.: Blue | - Excit.: White



Signal at FS: 2 mV/V ± 10 %  
 Combined error: ±0.017 %FS  
 Impedance (in/out): 410 Ω ± 20 / 350 Ω ± 5  
 Compensated temperature range: -10 ... +40°C  
 Platform size: up to 300 x 350 mm  
 Cable/length: 4 shielded wires / 1 m  
 Warranty: 1 year

Replaces: TH 1040/1042, HBM SP4, RT 642, CAS BCA, (+ 14 mm spacer)

P/N	Designation	FS	V <sub>min.</sub>	DC
400778	LOAD CELL AL3 C3 SH 10e	3 kg	0.3 g	R1
400779	LOAD CELL AL5 C3 SH 10e	5 kg	0.5 g	R1
400780	LOAD CELL AL7 C3 SH 10e	7 kg	0.7 g	R1
400781	LOAD CELL AL10 C3 SH 10e	10 kg	1 g	R1
400782	LOAD CELL AL15 C3 SH 10e	15 kg	1.5 g	R1
400784	LOAD CELL AL30 C3 SH 10e	30 kg	3 g	R1
	<b>Option:</b>			
850203	OPTIONAL PROTECTIVE COATING			R1

FS: rated capacity / v min = minimal interval (according to cert. OIML R60) / C.E. = Combined error in % of FS / DC = Code per back

## B.4. Calibration of the force transducer

The calibration of the force transducer was repeated for four different heights, namely at  $z = 0.23$  m,  $z = 0.345$  m,  $z = 0.46$  and  $z = 0.72$  m. This resulted in the new formulas, which are shown in figures B.1, B.2, B.3 and B.4.

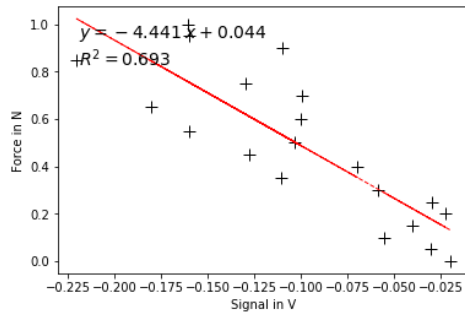


Figure B.1: Calibration formula measured at 23 cm from the bed

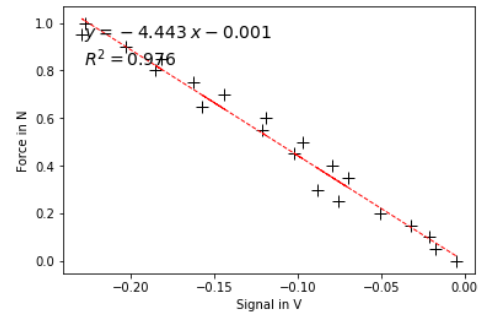


Figure B.2: Calibration formula measured at 34.5 cm from the bed

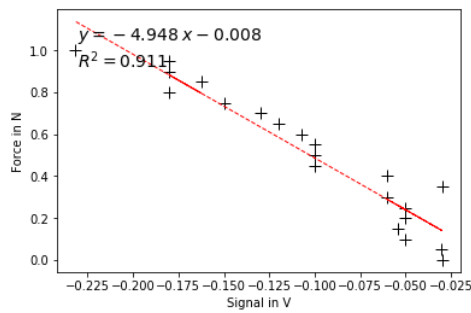


Figure B.3: Calibration formula measured at 46 cm from the bed

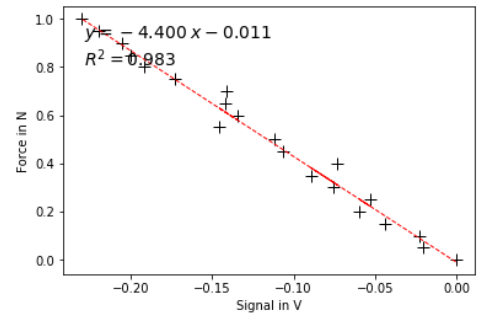


Figure B.4: Calibration formula measured at 72 cm from the bed

# C

## Wave paddle script for Cnoidal waves

The script that was used to generate the cnoidal waves is included. It determines the time series for the wave paddle position. The input parameters are the wave height, water depth and wave period and the surface elevation and phase velocity are based on the Fenton theory. Moreover, a ramp-up and ramp-down is included to slowly start and shut down the wave generator.

```
1 % wave paddle motion
2 clear all
3 close all
4
5 %% wave properties
6 H = 0.17; % Wave height [m]
7 h = 0.5; % Water depth [m]
8 T = 5.6; % Wave period [s]
9 omeg = 2.*pi./T;
10 EorS = 'Eulerian'; % Either 'Stokes' or 'Eulerian' drift.
11 uEorS = 0; % Magnitude of the Stokes or Eulerian drifts
12 nsteps = 15;
13 g = 9.81;
14 N = 10; % number of harmonics
15
16 %% Integration characteristics
17 % definition of points for vertical velocity profile
18 % to calculate depth averaged velocity
19 dz = 0.01; % spacing for vertical integration
20 emfHeight = dz:dz:h; % height of each point from the bed
21 emfHeight = emfHeight';
22 numz = length(emfHeight);
23
24 % definition of time series
25 t1 = 0; %first point for time series
26 t2 = 30.*T; %last point for time series
27 numpoints = t2*25; % number of points time series
28 t = linspace(t1,t2,numpoints+1); % generated time series
29 dt = t(2)-t(1); % time step
30
31 %definition of ramp-up and ramp-down time
32 Tr = 5*T; %in this case, five times the wave period
33
34 %% generation of the wave with stream function theory
35 [eta, B, Q, c, k, R, uBar] = StreamFunctionCoefficientsPeriod(N,H,h,T,uEorS,EorS,nsteps
    ,g);
36
37 %% calculating the surface elevation and velocities
38 % Solving for the surface elevation coefficients
39 matrix = ones(N+1);
40
41 for i=0:N
42     matrix(i+1,1:end-1) = cos((1:N) * i * pi / N);
43 end
44
```

```

45 A = matrix\eta';
46
47 % Calculating surface elevation time series
48 etaT = zeros(size(t)) + A(end);
49 for j=1:N
50     etaT = etaT + A(j) * cos(- j * 2 * pi / T * t);
51 end
52
53 tim = 0;
54 numtim = length(etaT);
55
56 %% Calculating depth-averaged velocity
57 x_int(1) = 0; % turn-on this line to follow paddle motion
58
59 tim = t1;
60 for i = 1:numtim
61     tim = dt + tim;
62     f_up(i) = sin((2*pi/Tr)*min(tim,Tr/4)); % Ramp-up scaling factor
63
64     for j = numz:-1:1 % loop over the vertical coordinate
65         u(j,i) = omeg/k - uBar;
66         uLWT(j,i) = (H/2)*omeg*cosh(k*emfHeight(j,1))/sinh(k*h)*cos(-omeg*tim); %
        Linear wave theory
67         for l = 1:N % adding the different harmonics
68             %u(j,i) = u(j,i)+B(l)*cosh(l*k*emfHeight(j,1))/cosh(l*k*h)*cos(-l*omeg*tim)
69
70             % to follow the paddle motion, use the line below
71             u(j,i) = u(j,i)+B(l)*cosh(l*k*emfHeight(j,1))/cosh(l*k*h)*cos(l.*k.*x_int(i)
72             -l*omeg*tim);
73         end
74     end
75
76     u_int(1,i) = trapz(u(:,i)).*dz./h; % depth-averaged velocity
77
78 % to follow the paddle motion, use the line below
79 x_int(i+1) = x_int(i) + u_int(1,i).*dt;
80 end
81
82 f_down = flip(f_up); % Ramp-down scaling factor
83
84 figure,
85 subplot(4,1,1)
86 plot(t,etaT)
87 ylabel('\eta [m]')
88
89 subplot(4,1,2)
90 plot(t,u_int)
91 ylabel('U_{da} [m/s]')
92
93 %% calculating position paddle
94 X_paddle = cumtrapz(t,u_int);
95
96 subplot(4,1,3)
97 plot(t,X_paddle)
98 ylabel('x_{paddle} (no spin-up) [m]')
99
100 X_paddle = detrend(X_paddle);
101
102 %% multiplying the paddle position by the the ramp-up and ramp-down factors
103 X_paddle = X_paddle.*f_up.*f_down;
104
105 subplot(4,1,4)
106 plot(t,X_paddle)
107 ylabel('x_{paddle} (spin-up) [m]')

```

Listing C.1: Wave paddle

# D

## Location of the cylinder

For the steady flow experiments, the location of the cylinder over the length of the flume has to be determined. There are three requirements for the location of the cylinder:

1. The required Reynolds numbers are reached.
2. The boundary layer must be turbulent in the flume.
3. The boundary layer must have the same thickness as the water level,  $h$ , in the flume.

### D.1. Required Reynolds number

The aim of the steady flow experiments is to obtain the curve for the drag coefficient as a function of the Reynolds number. From 4.11a, it is assumed that the drag crisis for the roughness of the mussels will take place between  $Re = 10^3 - 10^4$ . To achieve these numbers, a certain velocity must be reached. This is calculated with the following equation:

$$u = \frac{Re\nu}{D} \quad (D.1)$$

Where  $u$  is the flow velocity,  $Re$  is the Reynolds number,  $\nu$  is the kinematic viscosity and  $D$  is the diameter. At the same time, the Froude ( $Fr$ ) number must also be smaller than 1 to have sub-critical flow.

$$Fr = \frac{u}{\sqrt{gh}} \quad (D.2)$$

Where  $g$  is the gravitational acceleration and  $h$  is the water depth.

## D.2. Turbulent Boundary layer

The boundary layer starts laminar, and after a critical point, it turns turbulent, as shown in D.1. This transition occurs at Reynolds numbers of  $5 * 10^5 - 3 * 10^6$ . The Reynolds number is now expressed as function of  $x$  and describes the flow in the flume.

$$Re_x = \frac{ux}{\nu} \quad (D.3)$$

where  $x$  is the distance from the beginning of the flume, and  $Re_x$  is the Reynolds number as a function of  $x$

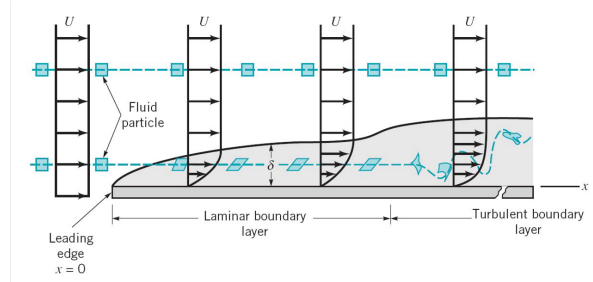


Figure D.1: Development of the boundary layer over the distance,  $x$  (Munson et al., 1994)

## D.3. Thickness of the boundary layer

As depicted in D.1, the growth of the boundary layer changes after the transition. For laminar flow, the layer thickness can be described with the following formula:

$$\delta = \frac{5x}{\sqrt{Re_x}} \quad (D.4)$$

Where  $\delta$  is the boundary layer thickness.

The layer thickness changes for a turbulent flow to:

$$\delta = \frac{0.37x}{Re_x^{\frac{1}{5}}} \quad (D.5)$$

Therefore any point after the critical point, the boundary layer thickness can be described as:

$$\delta = \frac{5x}{\sqrt{Re_x}} + \frac{0.37(x - x_{cr})}{Re_x^{\frac{1}{5}}} \quad (D.6)$$

For the location of the model, the  $\delta$  must be equal to the water level,  $h$ .

# E

## Averaging interval

Figure E.1 shows the difference in the mean velocity of various intervals to the mean velocity of  $dt = 1$ . The differences for all intervals are negligibly small.

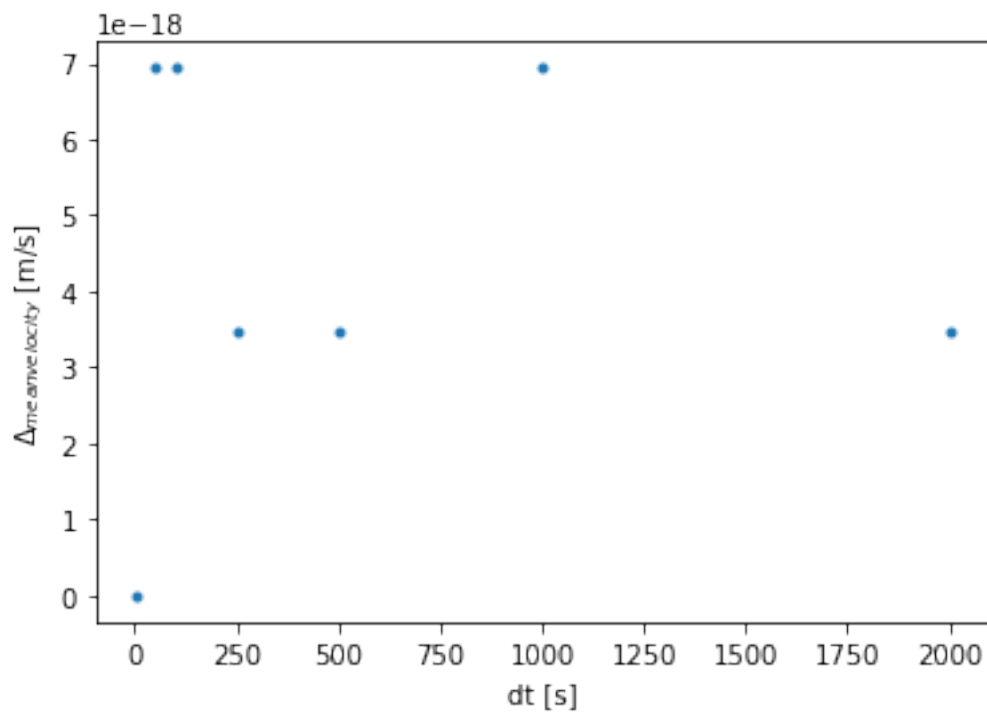


Figure E.1: The difference in mean velocity using multiple averaging intervals.

# F

## Filters for the force data

Figure F.1 shows the raw data series of one of the force measurements. If we zoom in and look at figure F.2, oscillations can be seen after the peak in the force. To remove the oscillations, a filter needs to be applied to the raw time series.

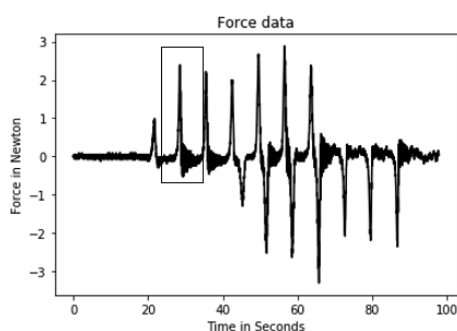


Figure F.1: The full and raw time series of the force data

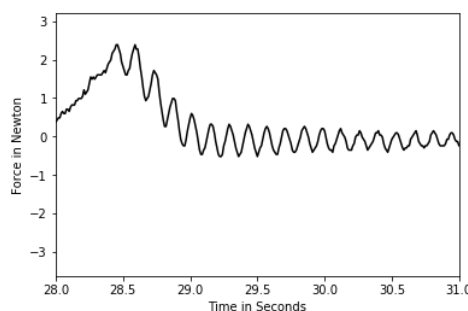


Figure F.2: The zoomed in and raw time series of the force data

Five different filters are applied to the data and shown in figures F.3, F.5, F.4 and F.6. The filters are a moving average, low frequency filter, the peaks, troughs and the zero-crossings of the oscillations. The step size of the moving average is determined manually. The step size is constant and has a value of 14. This suggests that these oscillation are due to the eigenfrequency of the cylinder. The low frequency filter has frequency of 0.05 Hz. The peaks and troughs are determined by the find peaks function of Python. The zero-crossing is determined by the time steps of the peak and troughs of the find peaks function. Eventually, the low frequency filter was chosen to apply to the signals.



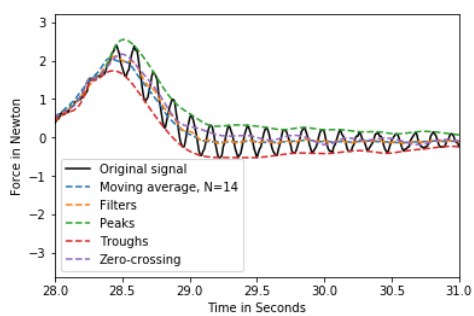


Figure E3: Overview of 5 ways to filter the time series of the force data

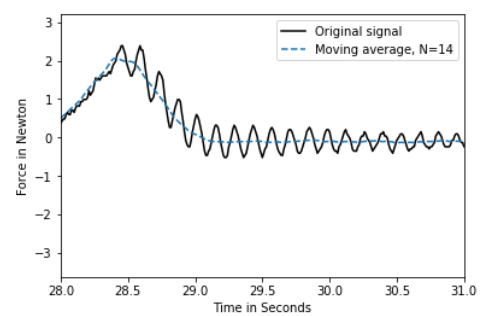


Figure E4: Filter based on the resonance of the cylinder

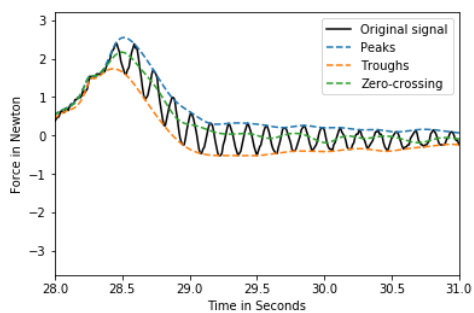


Figure E5: 3 Filter based on the peaks, troughs and zero-down crossing of the force data

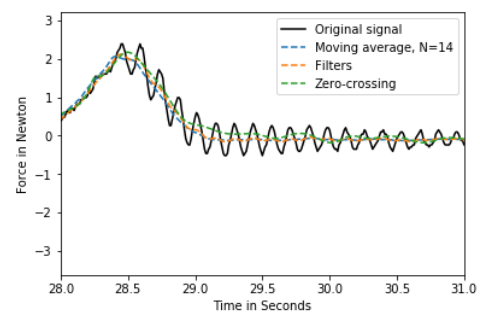


Figure E6: Comparison of the moving average filter, low pass filter and the zero down crossing filter

# G

## Graphs of the waves

### G.1. Smooth cylinder: $H = 4 \text{ cm}$ and $T = 1 \text{ s}$

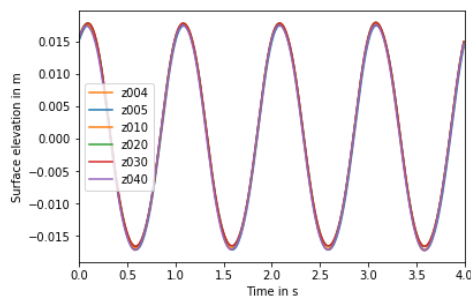


Figure G.1: The surface elevation for  $H = 4 \text{ cm}$  and  $T = 1 \text{ sec}$ .

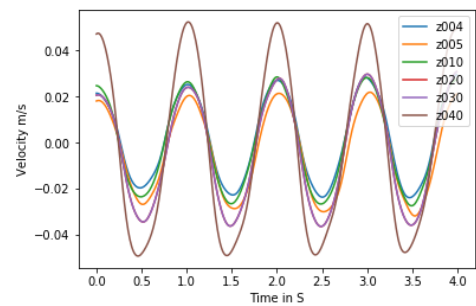


Figure G.2: The velocity for  $H = 4 \text{ cm}$  and  $T = 1 \text{ sec}$

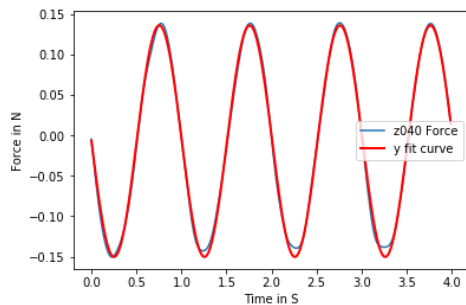


Figure G.3: The force on the cylinder with the fitted sinus function for  $H = 4 \text{ cm}$  and  $T = 1 \text{ sec}$ .

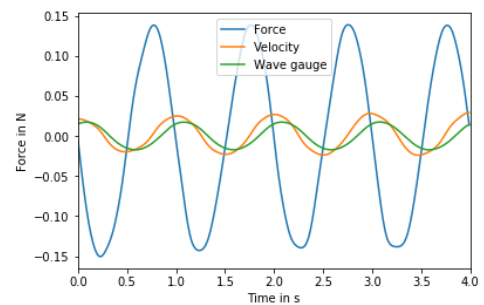


Figure G.4: Surface elevation, velocity and force plotted together.

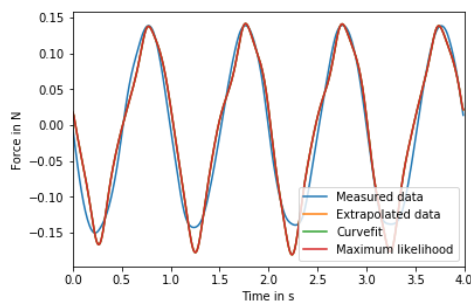


Figure G.5: The measured and calculated force.

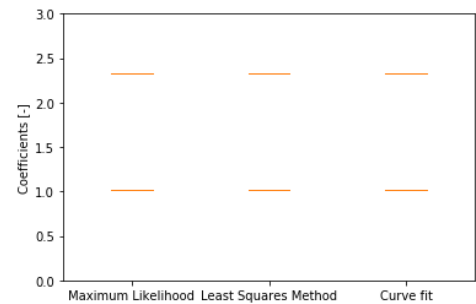


Figure G.6: Drag and inertia coefficients

### G.2. Smooth cylinder: H = 4 cm and T = 2 s

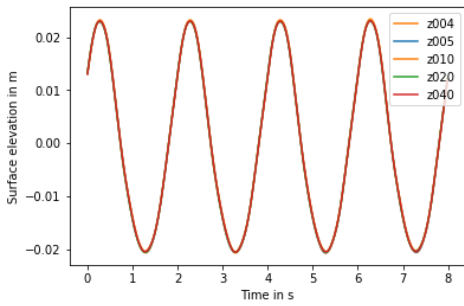


Figure G.7: The surface elevation for H = 4 cm and T = 2 sec.

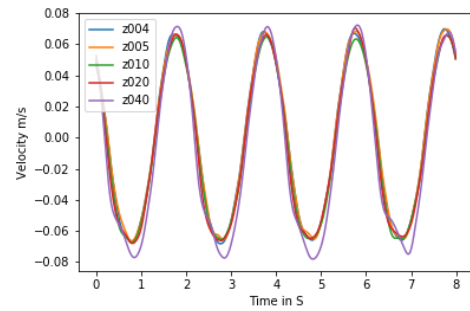


Figure G.8: The velocity for H = 4 cm and T = 2 sec

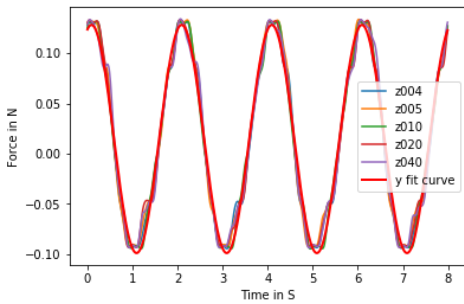


Figure G.9: The force on the cylinder with the fitted sinus function for H = 4 cm and T = 2 sec.

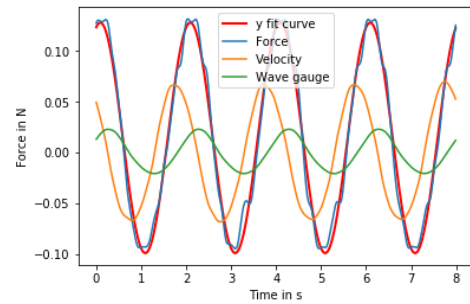


Figure G.10: Surface elevation, velocity and force plotted together.

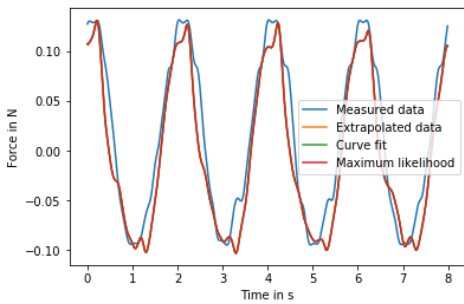


Figure G.11: The measured and calculated force.

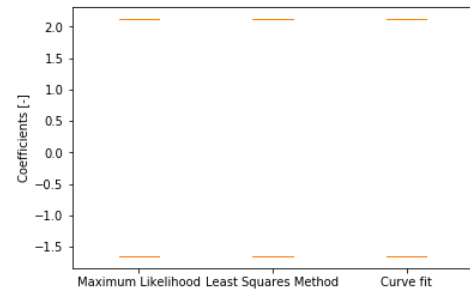


Figure G.12: Drag and inertia coefficients

### G.3. Smooth cylinder: $H = 4$ cm and $T = 3$ s

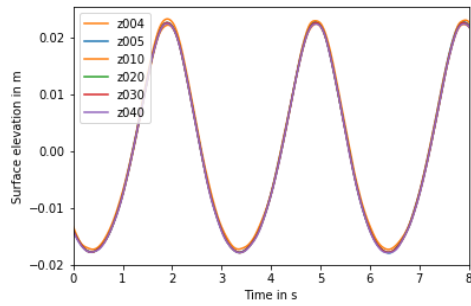


Figure G.13: The surface elevation for  $H = 4$  cm and  $T = 3$  sec.

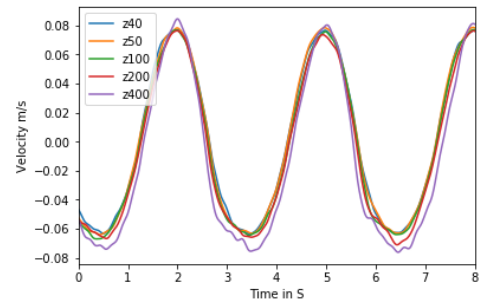


Figure G.14: The velocity for  $H = 4$  cm and  $T = 3$  sec

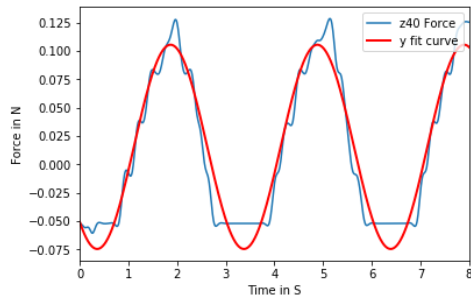


Figure G.15: The force on the cylinder with the fitted sinus function for  $H = 4$  cm and  $T = 3$  sec.

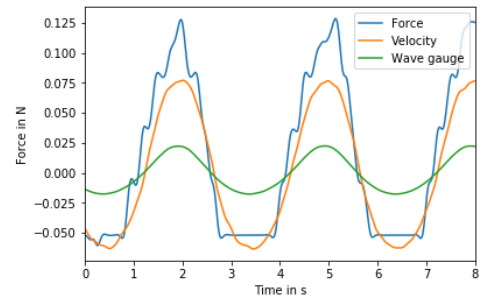


Figure G.16: Surface elevation, velocity and force plotted together.

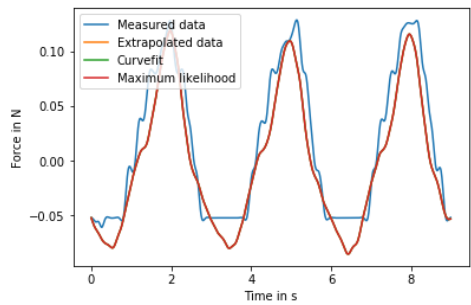


Figure G.17: The measured and calculated force.

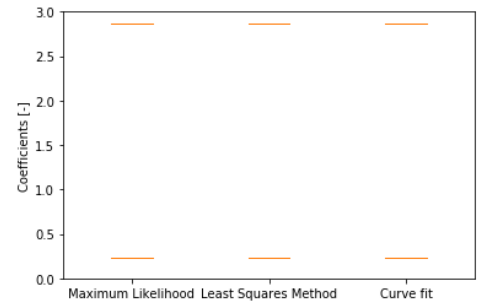


Figure G.18: Drag and inertia coefficients

### G.4. Smooth cylinder: $H = 13$ and $T = 2$ s

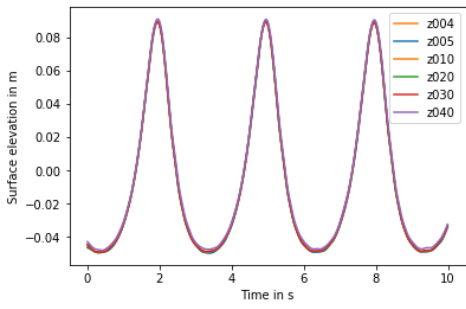


Figure G.19: The surface elevation for  $H = 13$  cm and  $T = 2$  sec.

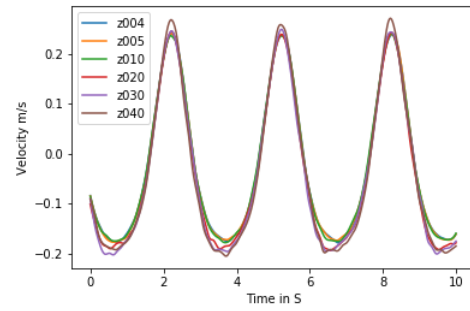


Figure G.20: The velocity for  $H = 13$  cm and  $T = 2$  sec.

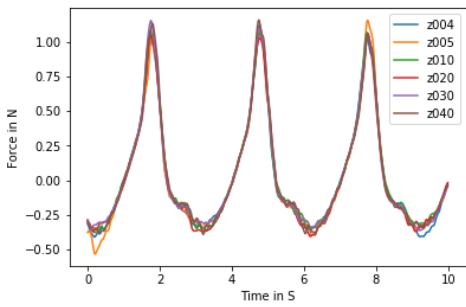


Figure G.21: The force on the cylinder with the fitted sinus function for  $H = 13$  cm and  $T = 2$  sec.

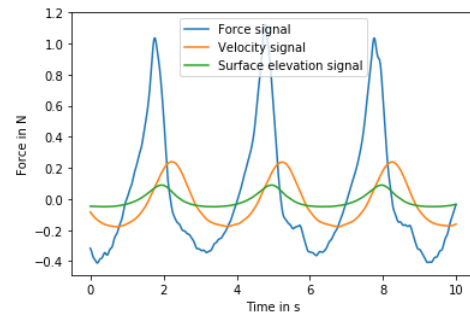


Figure G.22: Surface elevation, velocity and force plotted together.

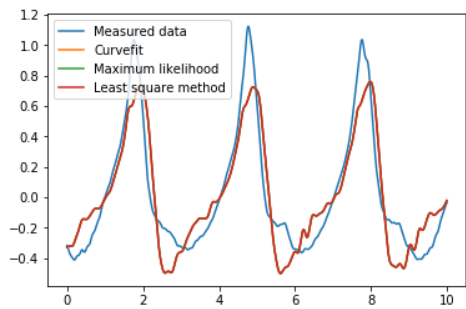


Figure G.23: The measured and calculated force.

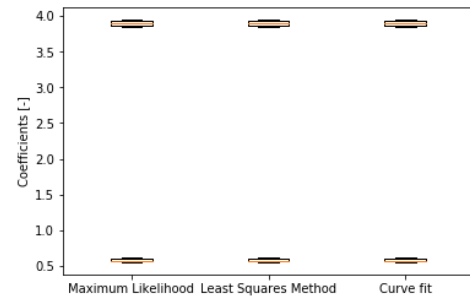


Figure G.24: Drag and inertia coefficients

### G.5. Smooth cylinder: $H = 13$ cm and $T = 3$ s

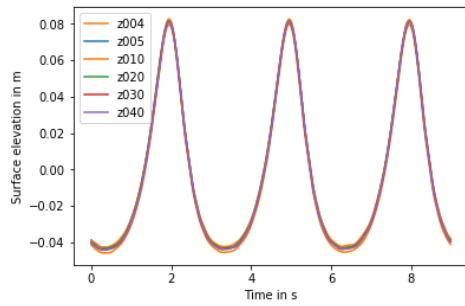


Figure G.25: The surface elevation for  $H = 13$  cm and  $T = 3$  sec.

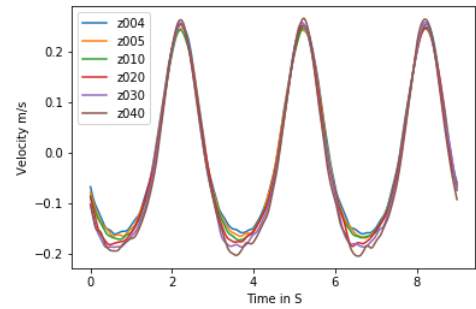


Figure G.26: The velocity for  $H = 13$  cm and  $T = 3$  sec

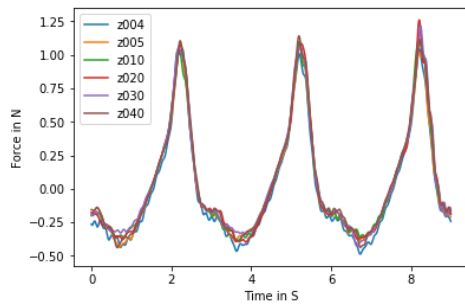


Figure G.27: The force on the cylinder with the fitted sinus function for  $H = 13$  cm and  $T = 3$  sec.

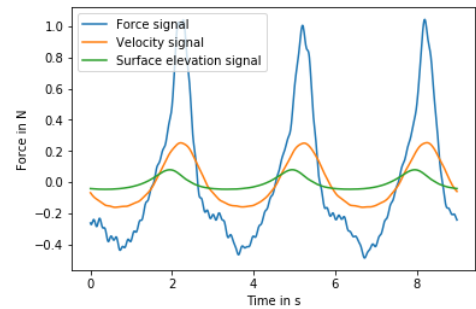


Figure G.28: Surface elevation, velocity and force plotted together.

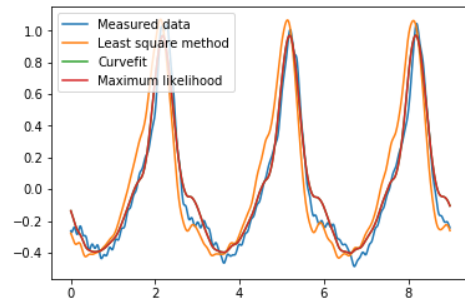


Figure G.29: The measured and calculated force.

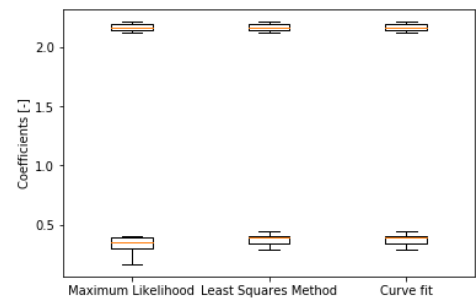


Figure G.30: Drag and inertia coefficients

### G.6. Smooth cylinder: H = 13 cm and T = 6 s

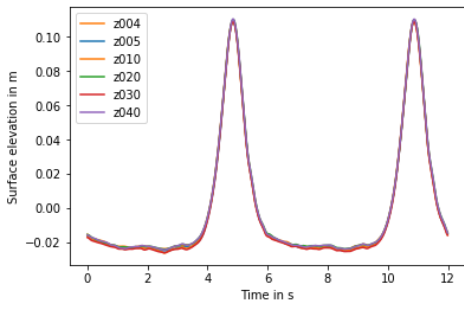


Figure G.31: The surface elevation for H = 13 cm and T = 6 sec.

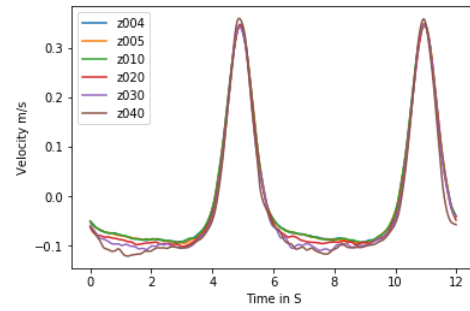


Figure G.32: The velocity for H = 13 cm and T = 6 sec

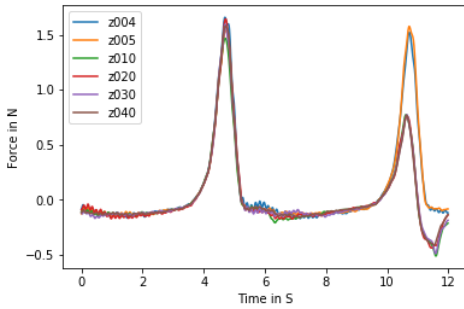


Figure G.33: The force on the cylinder with the fitted sinus function for H = 13 cm and T = 6 sec.

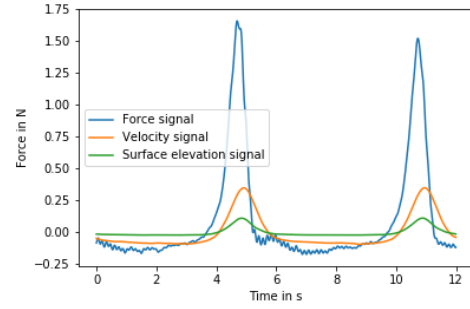


Figure G.34: Surface elevation, velocity and force plotted together.

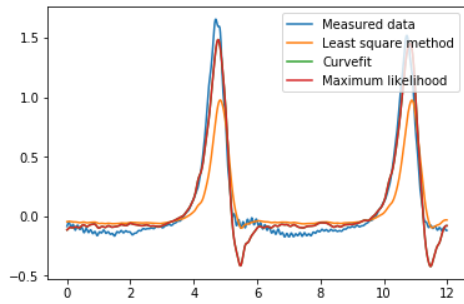


Figure G.35: The measured and calculated force.

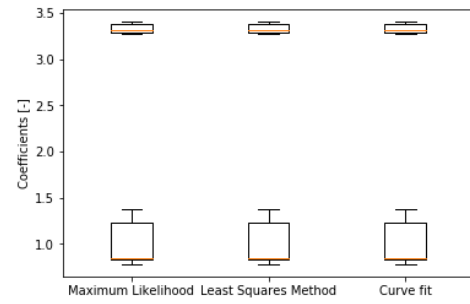


Figure G.36: Drag and inertia coefficients

### G.7. Smooth cylinder: $H = 13$ cm and $T = 7$ s

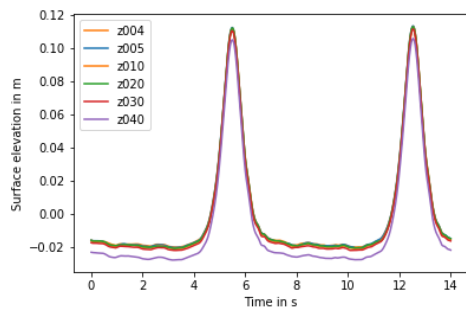


Figure G.37: The surface elevation for  $H = 13$  cm and  $T = 7$  sec.

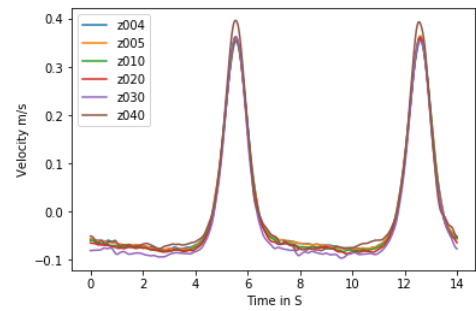


Figure G.38: The velocity for  $H = 13$  cm and  $T = 7$  sec

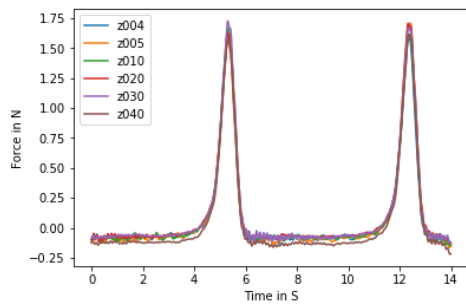


Figure G.39: The force on the cylinder with the fitted sinus function for  $H = 13$  cm and  $T = 7$  sec.

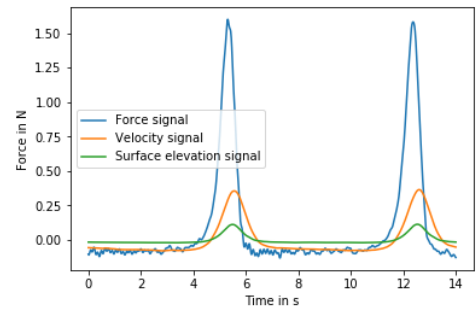


Figure G.40: Surface elevation, velocity and force plotted together.

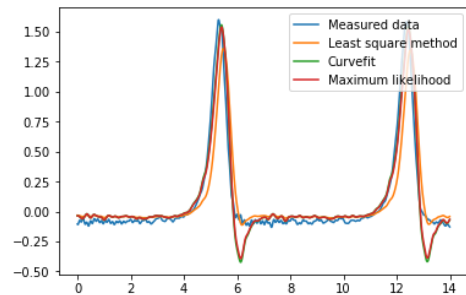


Figure G.41: The measured and calculated force.

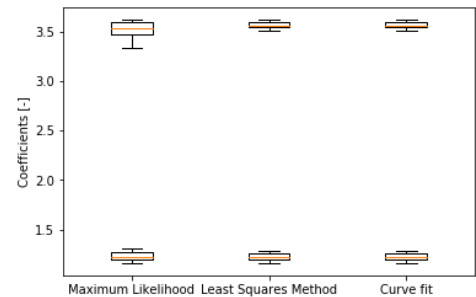


Figure G.42: Drag and inertia coefficients



### G.8. Mussels: $H = 6.66$ cm and $T = 1$ s

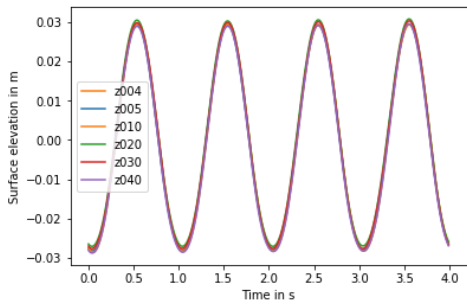


Figure G.43: The surface elevation for  $H = 6.66$  cm and  $T = 1$  sec.

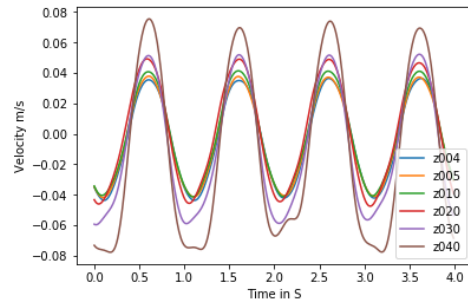


Figure G.44: The velocity for  $H = 6.66$  cm and  $T = 1$  sec

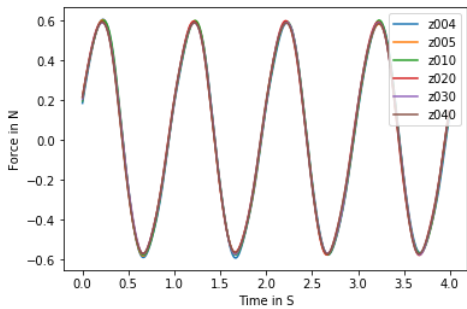


Figure G.45: The force on the cylinder with the fitted sinus function for  $H = 6.66$  cm and  $T = 1$  sec.

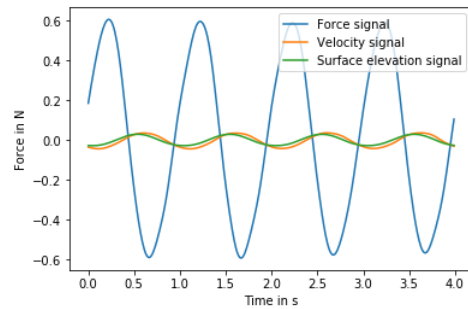


Figure G.46: Surface elevation, velocity and force plotted together.

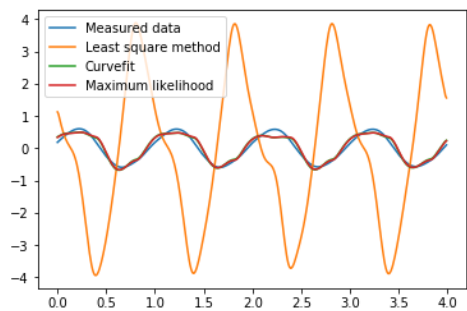


Figure G.47: The measured and calculated force.

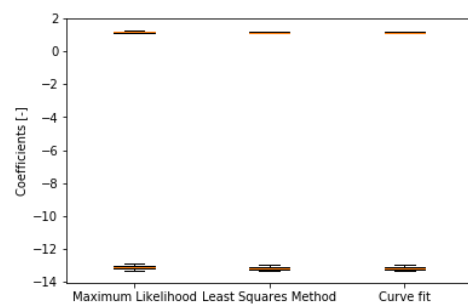


Figure G.48: Drag and inertia coefficients

**G.9. Mussels:  $H = 6.66$  cm and  $T = 2$  s**

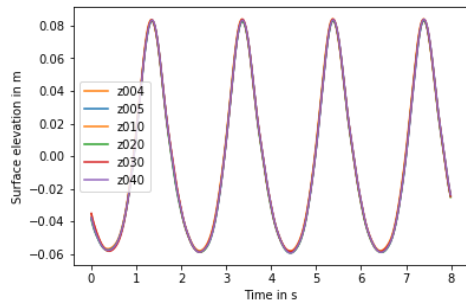


Figure G.49: The surface elevation for  $H = 6.66$  cm and  $T = 2$  sec.

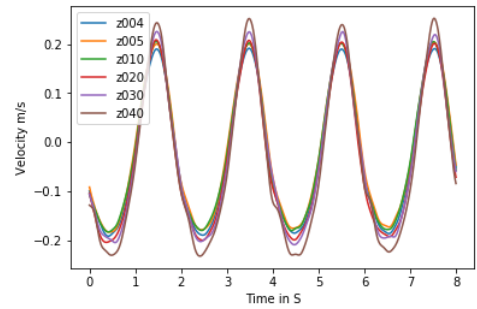


Figure G.50: The velocity for  $H = 6.66$  cm and  $T = 2$  sec

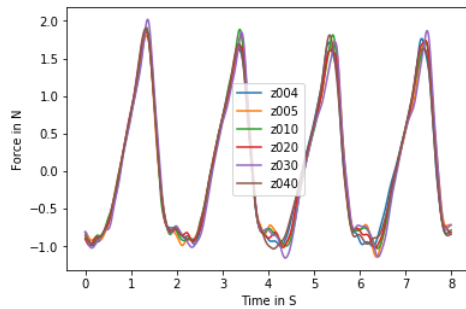


Figure G.51: The force on the cylinder with the fitted sinus function for  $H = 6.66$  cm and  $T = 2$  sec.

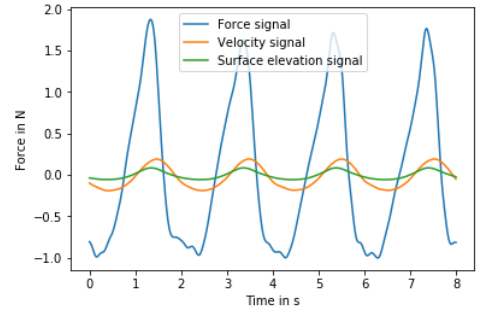


Figure G.52: Surface elevation, velocity and force plotted together.

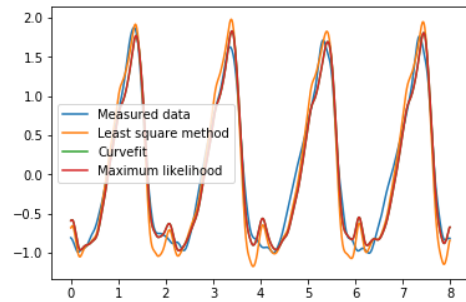


Figure G.53: The measured and calculated force.

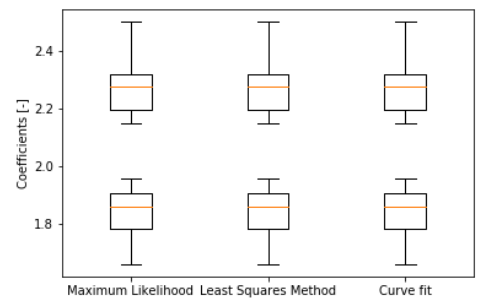


Figure G.54: Drag and inertia coefficients

**G.10. Mussels:  $H = 6.66$  cm and  $T = 3$  s**

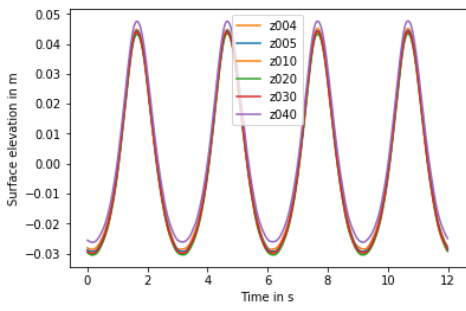


Figure G.55: The surface elevation for  $H = 6.66$  cm and  $T = 3$  sec.

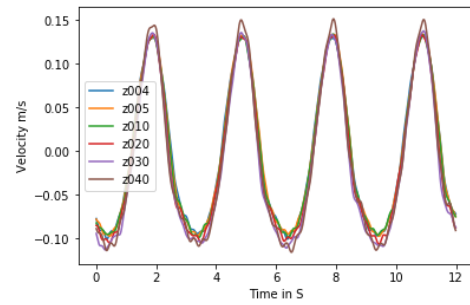


Figure G.56: The velocity for  $H = 6.66$  cm and  $T = 3$  sec.

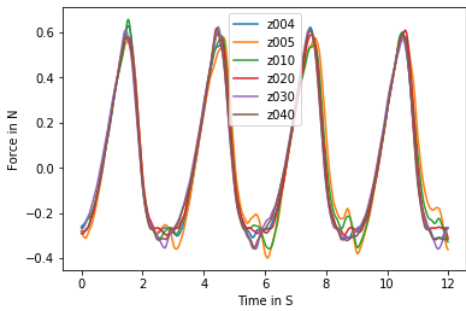


Figure G.57: The force on the cylinder with the fitted sinus function for  $H = 6.66$  cm and  $T = 3$  sec.

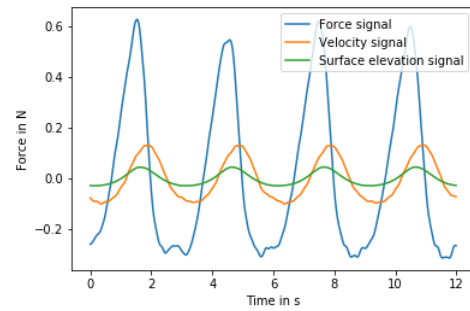


Figure G.58: Surface elevation, velocity and force plotted together.

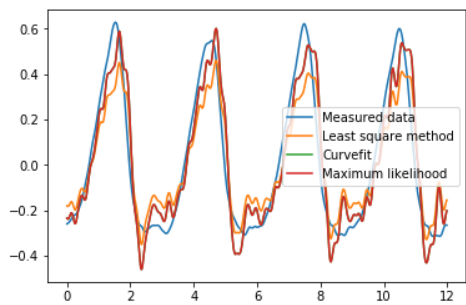


Figure G.59: The measured and calculated force.

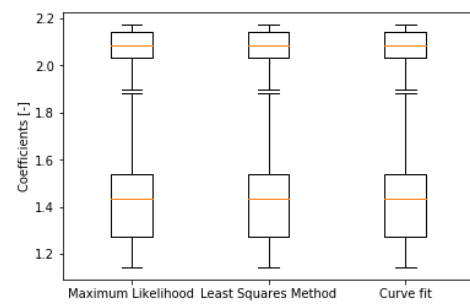


Figure G.60: Drag and inertia coefficients

### G.11. Mussels: $H = 21.3$ cm and $T = 1.5$ s

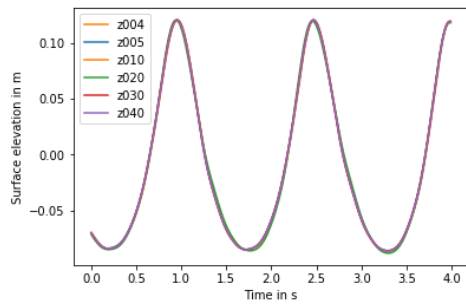


Figure G.61: The surface elevation for  $H = 21.3$  cm and  $T = 1.5$  sec.

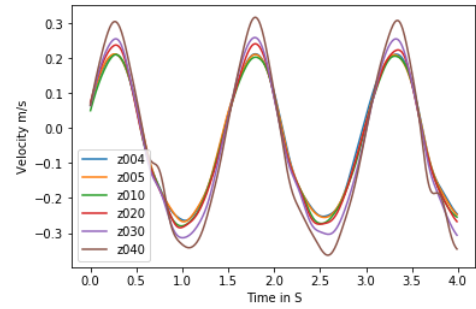


Figure G.62: The velocity for  $H = 21.3$  cm and  $T = 1.5$  sec.

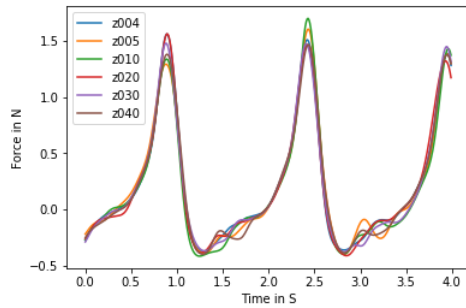


Figure G.63: The force on the cylinder with the fitted sinus function for  $H = 21.3$  cm and  $T = 1.5$  sec.

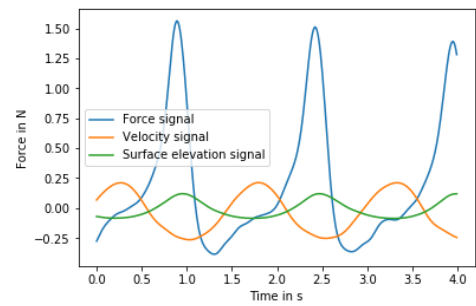


Figure G.64: Surface elevation, velocity and force plotted together.

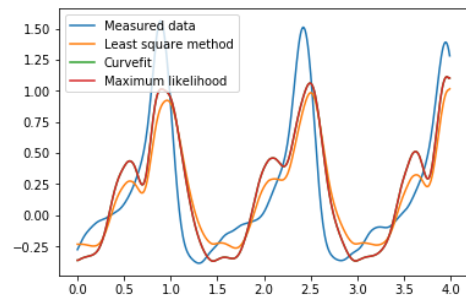


Figure G.65: The measured and calculated force.

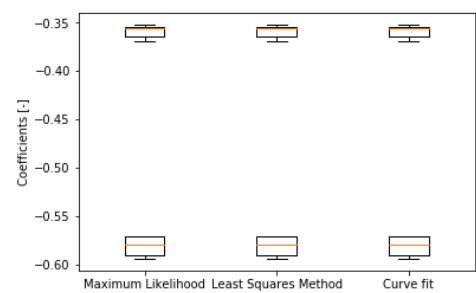


Figure G.66: Drag and inertia coefficients

### G.12. Mussels: $H = 21.3 \text{ cm}$ and $T = 2 \text{ s}$

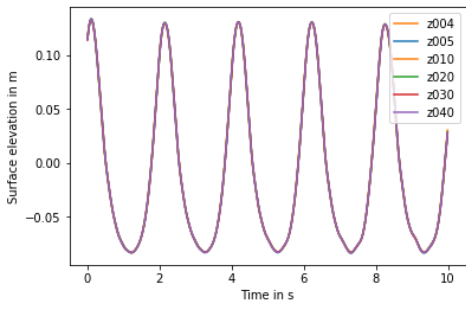


Figure G.67: The surface elevation for  $H = 4 \text{ cm}$  and  $T = 1 \text{ sec}$ .

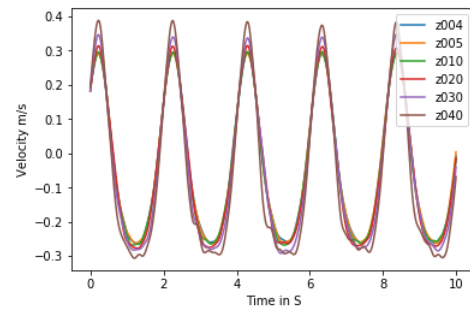


Figure G.68: The velocity for  $H = 4 \text{ cm}$  and  $T = 1 \text{ sec}$

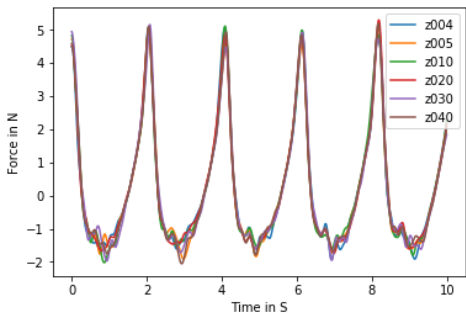


Figure G.69: The force on the cylinder with the fitted sinus function for  $H = 4 \text{ cm}$  and  $T = 1 \text{ sec}$ .

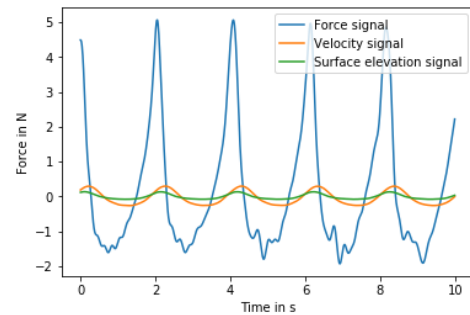


Figure G.70: Surface elevation, velocity and force plotted together.

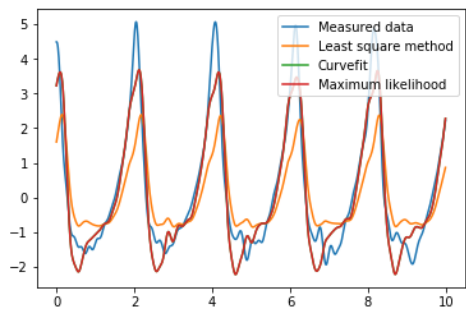


Figure G.71: The measured and calculated force.

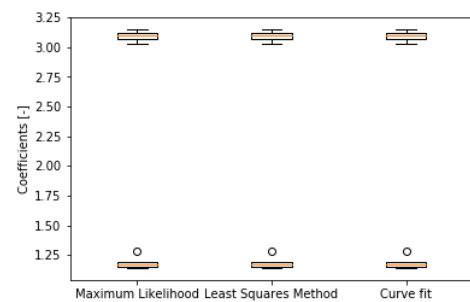


Figure G.72: Drag and inertia coefficients

**G.13. Mussels:  $H = 21.3$  cm and  $T = 3$  s**

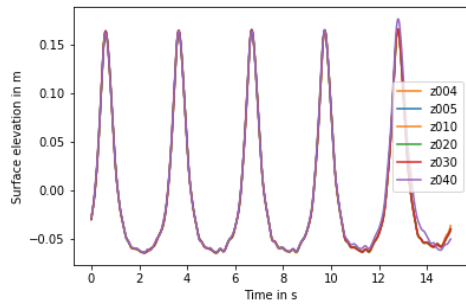


Figure G.73: The surface elevation for  $H = 4$  cm and  $T = 1$  sec.

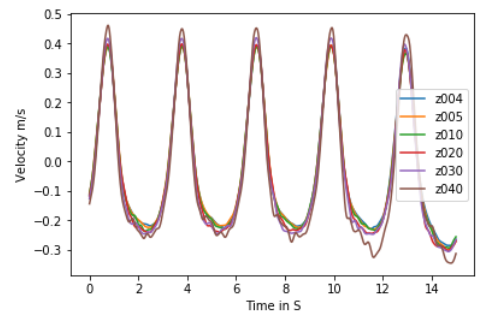


Figure G.74: The velocity for  $H = 4$  cm and  $T = 1$  sec

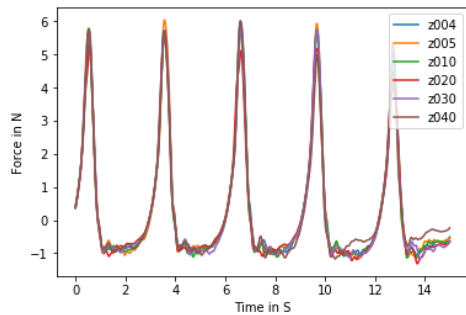


Figure G.75: The force on the cylinder with the fitted sinus function for  $H = 4$  cm and  $T = 1$  sec.

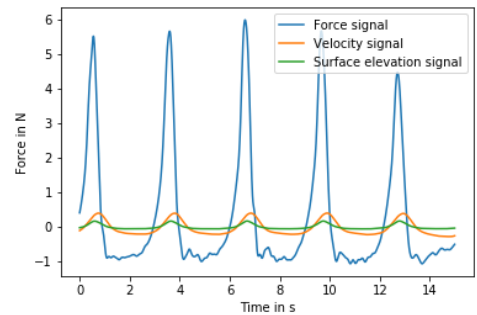


Figure G.76: Surface elevation, velocity and force plotted together.

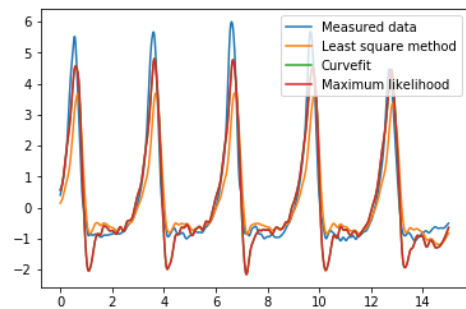


Figure G.77: The measured and calculated force.

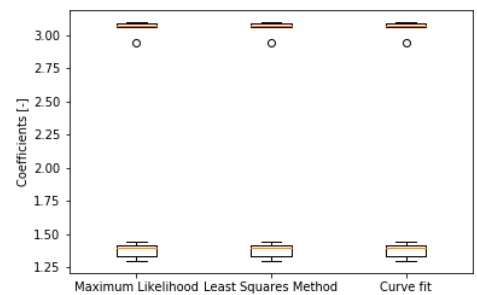


Figure G.78: Drag and inertia coefficients

### G.14. Mussels: $H = 21.3$ cm and $T = 4$ s

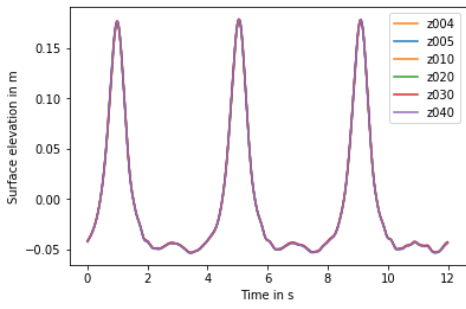


Figure G.79: The surface elevation for  $H = 21.3$  cm and  $T = 4$  sec.

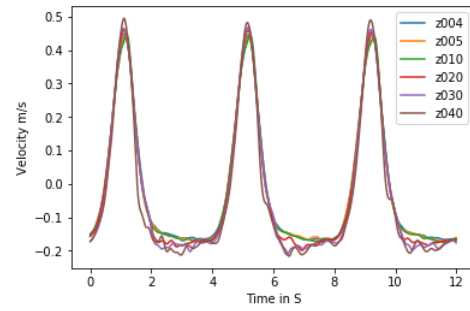


Figure G.80: The velocity for  $H = 21.3$  cm and  $T = 4$  sec.

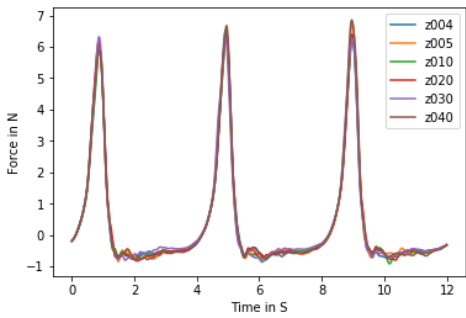


Figure G.81: The force on the cylinder with the fitted sinus function for  $H = 21.3$  cm and  $T = 4$  sec.

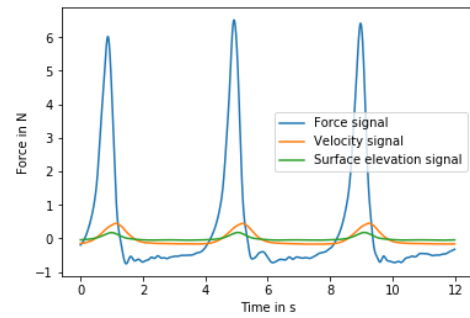


Figure G.82: Surface elevation, velocity and force plotted together.

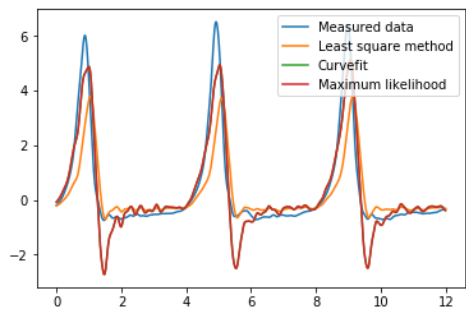


Figure G.83: The measured and calculated force.

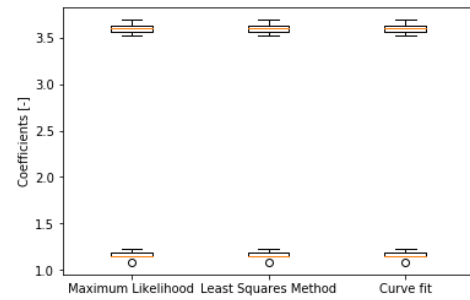


Figure G.84: Drag and inertia coefficients

**G.15. Mussels:  $H = 21.3$  cm and  $T = 5$  s**

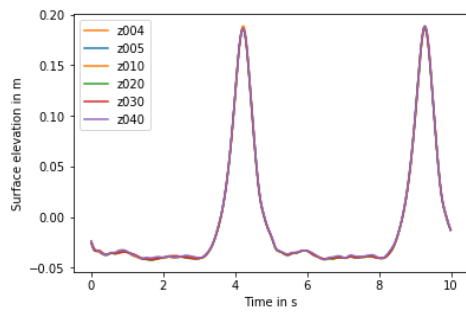


Figure G.85: The surface elevation for  $H = 21.3$  cm and  $T = 5$  sec.

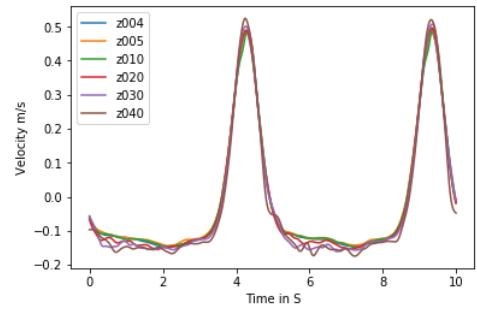


Figure G.86: The velocity for  $H = 21.3$  and  $T = 5$  sec

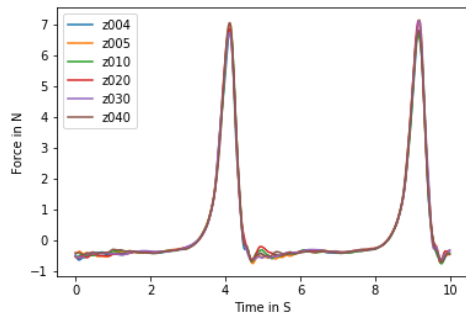


Figure G.87: The force on the cylinder with the fitted sinus function for  $H = 21.3$  and  $T = 5$  sec.

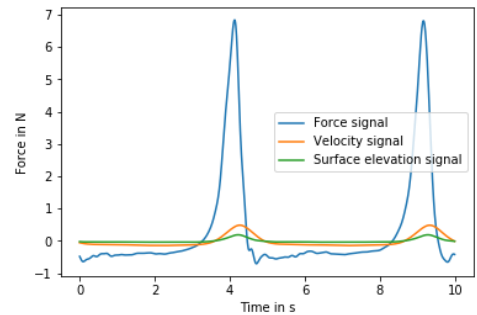


Figure G.88: Surface elevation, velocity and force plotted together.

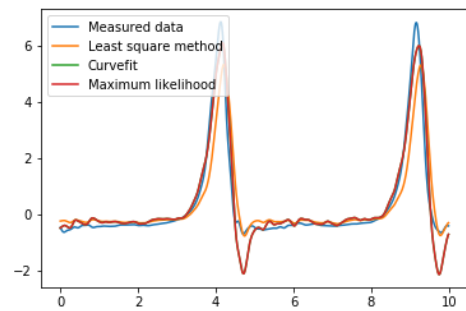


Figure G.89: The measured and calculated force.

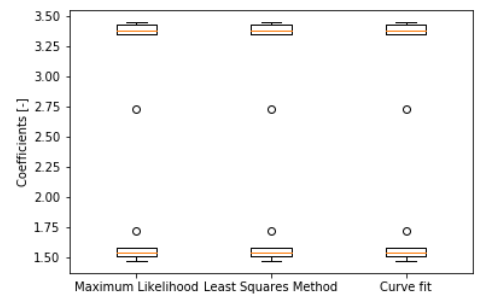


Figure G.90: Drag and inertia coefficients



### G.16. Mussels: $H = 21.3 \text{ cm}$ and $T = 6 \text{ s}$

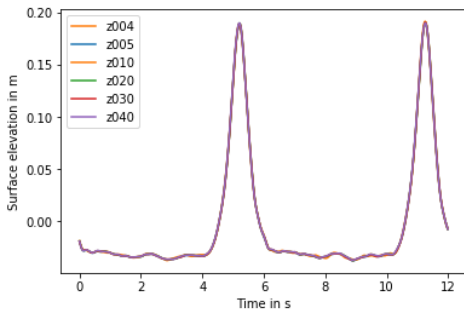


Figure G.91: The surface elevation for  $H = 4 \text{ cm}$   $T = 6 \text{ sec}$

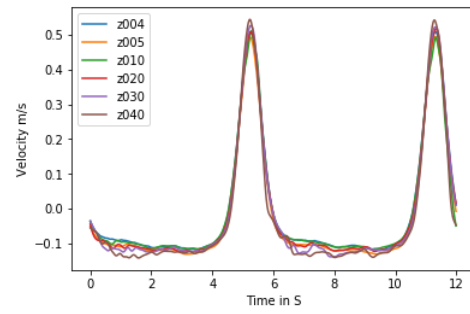


Figure G.92: The velocity for  $H = 4 \text{ cm}$  and  $T = 6 \text{ sec}$

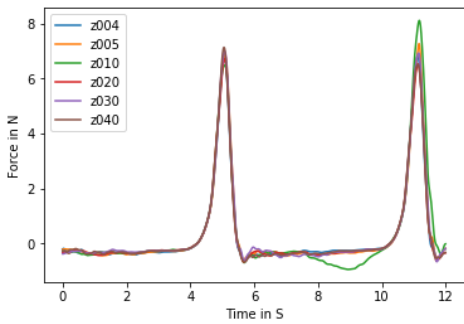


Figure G.93: The force on the cylinder with the fitted sinus function for  $H = 4 \text{ cm}$  and  $T = 1 \text{ sec}$ .

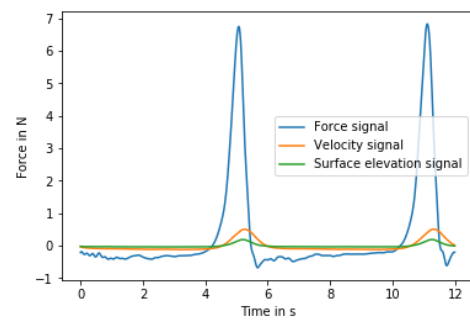


Figure G.94: Surface elevation, velocity and force plotted together.

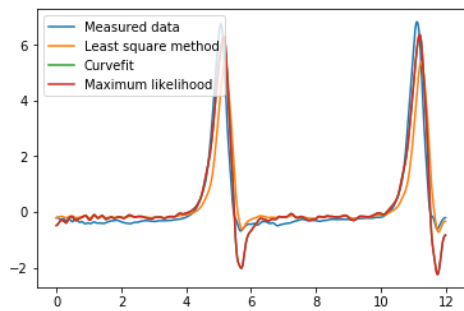


Figure G.95: The measured and calculated force.

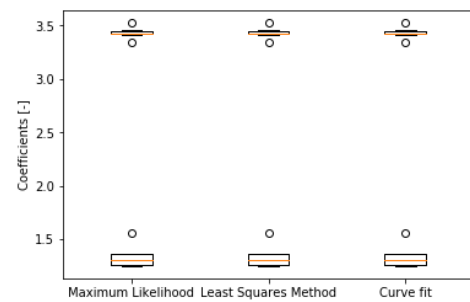


Figure G.96: Drag and inertia coefficients

### G.17. Mussels: $H = 21.3 \text{ cm}$ and $T = 7 \text{ s}$

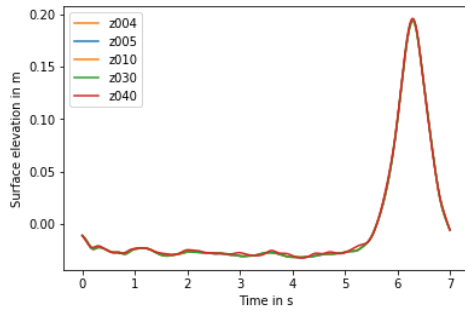


Figure G.97: The surface elevation for  $H = 4 \text{ cm}$  and  $T = 7 \text{ sec}$ .

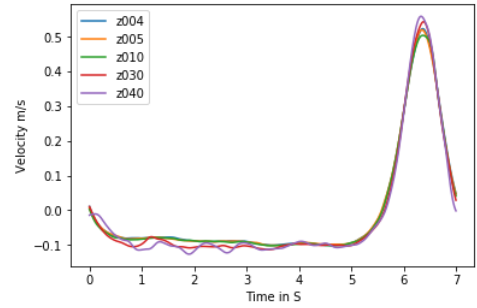


Figure G.98: The velocity for  $H = 4 \text{ cm}$  and  $T = 7 \text{ sec}$

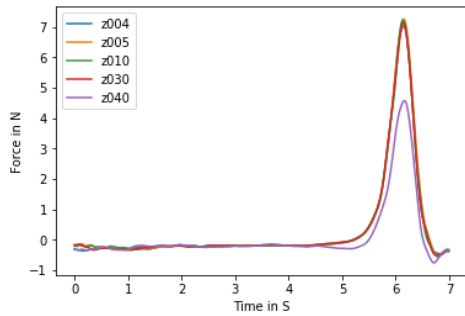


Figure G.99: The force on the cylinder with the fitted sinus function for  $H = 4 \text{ cm}$  and  $T = 7 \text{ sec}$ .

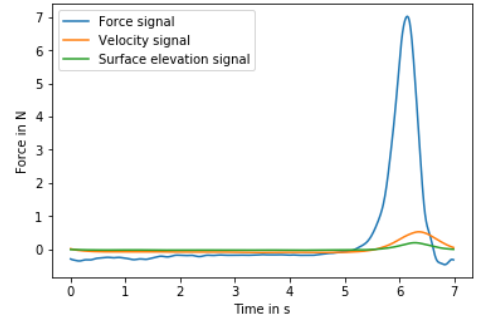


Figure G.100: Surface elevation, velocity and force plotted together.

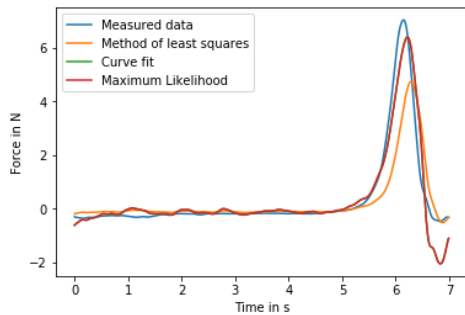


Figure G.101: The measured and calculated force.

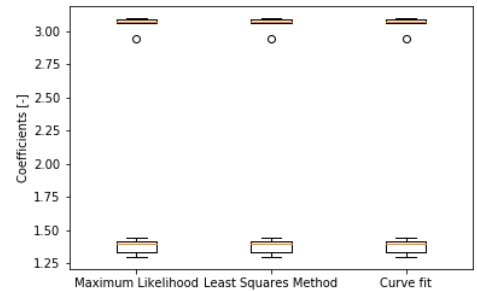


Figure G.102: Drag and inertia coefficients

### G.18. Overview

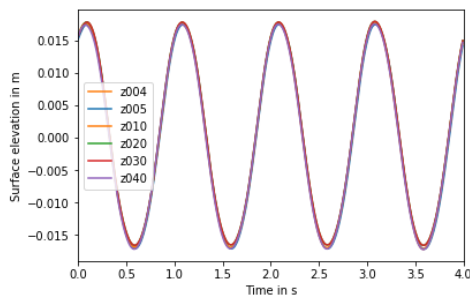


Figure G.103: Drag coefficient

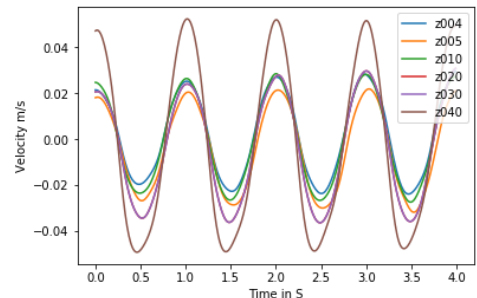
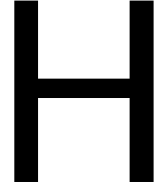


Figure G.104: Inertia coefficient



# Velocity and acceleration profile

The vertical velocity and acceleration profiles consist of data points at elevations of  $z = 0.04$  m,  $z = 0.05$  m,  $z = 0.10$  m,  $z = 0.20$  m,  $z = 0.30$  m and  $z = 0.40$  from the bed. The profiles need to be extrapolated from the bed to the surface level to have an accurate representation of the velocity and acceleration. This is done in two ways, namely by calculating the the velocity and acceleration points at the bed and the surface level and by fitting a line through the measured points.

## H.1. Velocity and acceleration points at the bed and surface

The equations to calculate the velocity at the bed and surface level are as follows:

$$u_{bed} = \cosh(k * z_0) * \frac{u_{0.04}}{\cosh(k * z_{0.04})} \quad (H.1)$$

Where  $u_{bed}$  is the velocity at the bed in  $m/s$ ,  $k$  is the wave number and  $z$  is the surface elevation in  $m$ .

$$u_{surface} = \cosh(k * z_{0.50}) * \frac{u_{0.40}}{\cosh(k * z_{0.40})} \quad (H.2)$$

Where  $u_{surface}$  is the velocity at the surface in  $m/s$ . The same equations are used for the acceleration. Only the velocity at  $0.04$  m and  $0.40$  m are replaced by the acceleration at  $0.04$  m and  $0.40$  m

## H.2. Fitted line

A line is fitted through the measured data points for the velocity and acceleration and extrapolates the data from the bottom to the surface. The velocity data points uses equation H.3 as a basis for the velocity profile. The acceleration data points uses equation H.4 as a basis for the acceleration profile. The variables are determined with the best fit function of Python.

$$u_z = \cosh(k * z_{EMF}) * a \quad (H.3)$$

$$a_z = a * z_{EMF} + b * z_{EMF}^2 + c \quad (H.4)$$

Where  $U_z$  is the velocity at the elevation  $z$  of the EMF,  $k$  is the wave number,  $z_{EMF}$  is the elevation of the EMF and  $a$ ,  $b$  and  $c$  are variables that the function is fitted to.



# Script for Fenton

```
1 def disper(k,omega,h):
2     g = 9.81
3     return omega**2-g*k*np.tanh(k*h)
4
5 def streamfunction1(x,n,H,d,T,uEorS,EorS,g):
6
7     js = np.arange(1,n+1,1)
8     F = np.zeros(5+2*n)
9
10    F[0] = x[3] - x[3+n] - H
11    F[1] = x[3] + x[3+n] + 2*np.sum(x[4:4+n-1])
12
13    if EorS == 'Euler':
14        F[2] = x[0] - uEorS + x[4+n]
15    elif EorS == 'Stokes':
16        F[2] = x[0] - uEorS + x[4+n] - x[1]/d
17    else:
18        print('EorS must be either "Euler" or "Stokes".')
19
20    k = 2*np.pi/(x[0]*T)
21
22    for i in range(n+1):
23        psi = x[n+4]*x[3+i] + np.sum(x[n+5:2*n+5]/(js*k) * np.sinh(k*js*(x[3+i] + d))/
24        np.cosh(js*k*d)*np.cos(js*i*np.pi/n))
25
26        u = x[n+4] + np.sum(x[n+5:2*n+5]*np.cosh(k*js*(x[3+i] + d))/np.cosh(js*k*d)*np.
27        cos(js*i*np.pi/n))
28
29        w = np.sum(x[n+5:2*n+5]*np.sinh(k*js*(x[3+i] + d))/np.cosh(js*k*d)*np.sin(js*i*
30        np.pi/n))
31
32        F[3+i] = psi + x[1]
33        F[3+n+1+i] = g*x[3+i] + 0.5*(u**2+w**2) - x[2]
34
35    return F
36
37 def streamfunctioncoefficients1(n,H,d,T,uEorS,EorS,nsteps,g):
38
39    #Initial parameters:
40
41    omega = 2*np.pi/T
42    k0 = fsolve(disper,0.01, args=(omega,d))
43    L0 = 2*np.pi/k0
44    c0 = omega/k0
45
46    H0 = H
47    H = H0/nsteps
48
49    x0 =np.concatenate((c0, 0, g/(2*k0)*np.tanh(k0*d), H/2*np.cos(np.arange(0,n+1,1)*np
50    .pi/n), -c0, g*H/2*T/L0, np.zeros(n-1)),axis=None)
```

```

47 sol = root(streamfunction1,x0, args=(n,H,d,T,uEorS,EorS,g), method='lm')
48 x_sol = sol.x
49
50 for i in range(nsteps-1):
51     H = (i+2)*H0/nsteps
52     x0 = x_sol
53     sol = root(streamfunction1,x0, args=(n,H,d,T,uEorS,EorS,g), method='lm')
54     x_sol = sol.x
55
56 c = x_sol[0]
57 q = x_sol[1]
58 R = x_sol[2]
59 eta = x_sol[3:4+n]
60 B = x_sol[4+n:2*n+5]
61
62 return c,q,R, eta, B
63
64 def depthaveraged(T,H,t2,k_da):
65
66     N = 10
67     omeg = 2 * np.pi / T
68     c,q, R, eta, B = streamfunctioncoefficients1(N,H,0.5,T,0,'Euler',15, 9.81)
69
70     dz = 0.05
71     h = 0.5 +dz
72     emfHeight = np.arange(0, h, dz)
73     emfHeight=np.atleast_2d(emfHeight).T.conj()
74     numz = len(emfHeight)
75
76     t1 = 0
77     t2 = t2*T
78     numpoints = 100
79     t = np.linspace(t1,t2, numpoints+1)
80     dt = t[1]-t[0]
81
82     matrix = np.ones((N+1, N+1))
83     time = np.arange(0,N+1,1)
84
85
86     for j in range(N+1):
87         for i in range(N):
88             matrix[j,i] = np.cos((i+1) *j* np.pi/N)
89
90     eta=np.atleast_2d(eta).T.conj()
91     A, res, rnk, s = lstsq(matrix, eta)
92     etaT = np.ones(len(t))*A[10]
93
94     w = np.zeros(N)
95
96     tim = 0
97     numtim = len(etaT)
98
99     #calculating depth averaged velocity
100    emfHeight = np.arange(dz, h, dz)
101    emfHeight=np.atleast_2d(emfHeight).T.conj()
102
103    u = np.zeros((N,numtim))
104    time = np.zeros(numtim)
105    u_int = np.zeros(numtim)
106    for i in range(numtim):
107        tim = dt + tim
108        time[i] = tim
109
110        for j in range(9, -1, -1):
111            u[j,i] = omeg/k_da - c;
112
113            for l in range(N-1):
114                u[j,i] = u[j,i]+B[l+1]*np.cosh((l+1)*k_da*emfHeight[j,0])/np.cosh((
115                    l+1)*k_da*0.5)*np.cos(-(l+1)*omeg*time[i]);
116
117    u_squared = u*abs(u)

```

```
117         u_int[i] = np.trapz(u_squared[:,i])*dz/0.5
118
119     acceleration = np.zeros((N, numtim))
120     acceleration_int = np.zeros(numtim)
121     for i in range(N):
122         acceleration[i,:]= np.gradient(u[i,:])/dt
123     for k in range(numtim):
124         acceleration_int[k] = np.trapz(acceleration[:,k])*dz/0.5
125
126
127     return u_int, acceleration_int, t
```

Listing I.1: Wave paddle

# Bibliography

- Alferink, M. (2022). Wave transmission through permeable structures in Demak Indonesia.
- Ameryoun, H., Schoefs, F., Barillé, L., & Thomas, Y. (2019). Stochastic modeling of forces on jacket-type offshore structures colonized by marine growth. *Journal of Marine Science and Engineering*, 7(5). <https://doi.org/10.3390/jmse7050158>
- Dean, R. G. (1965). Stream function wave theory – Validity and application. *Santa Barbara Specialty Conference*, 269–299.
- Deltares. (2021). *Technical specifications* (tech. rep.). [www.deltares.nl](http://www.deltares.nl)
- Deltares. (2022a). *Programmable electromagnetic liqued velocity meter* (tech. rep.). Deltares. Delft. [www.deltares.nl](http://www.deltares.nl)
- Deltares. (2022b). *Wave height meter* (tech. rep.). Deltares. Delft. [www.deltares.nl](http://www.deltares.nl)
- Donker, J. J., van der Vegt, M., & Hoekstra, P. (2013). Wave forcing over an intertidal mussel bed. *Journal of Sea Research*, 82, 54–66. <https://doi.org/10.1016/j.seares.2012.08.010>
- Fenton, J. D. (1985). A Fifth-Order Stokes Theory for Steady Waves. *Journal of Waterway, Port, Coastal, and Ocean Engineering*, 111(2), 216–234. [https://doi.org/10.1061/\(asce\)0733-950x\(1985\)111:2\(216\)](https://doi.org/10.1061/(asce)0733-950x(1985)111:2(216))
- Fenton, J. D. (1999). The Cnoidal Theory Of Water Waves. *Developments in Offshore Engineering*, 55–100. <https://doi.org/10.1016/b978-088415380-1/50021-2>
- Gieschen, R., Schwartpaul, C., Landmann, J., Fröhling, L., Hildebrandt, A., & Goseberg, N. (2021). Large-scale laboratory experiments on mussel dropper lines in ocean surface waves. *Journal of Marine Science and Engineering*, 9(1), 1–20. <https://doi.org/10.3390/jmse9010029>
- Gijón Mancheño, A., Jansen, W., Uijtewaal, W., Reniers, A., van Rooijen, A., Suzuki, T., Etminan, V., & Winterwerp, J. (2021a). Wave transmission and drag coefficients through dense cylinder arrays: Implications for designing structures for mangrove restoration. <https://doi.org/10.1016/j.ecoleng.2021.106231>
- Gijón Mancheño, A., Jansen, W., Uijtewaal, W., Reniers, A., van Rooijen, A., Suzuki, T., Etminan, V., & Winterwerp, J. (2021b). Wave transmission and drag coefficients through dense cylinder arrays: Implications for designing structures for mangrove restoration. *Ecological Engineering*, 165(October 2020), 106231. <https://doi.org/10.1016/j.ecoleng.2021.106231>
- Goring, D. G. (1978). *TSUNAMIS-THE PROPAGATION OF LONG WAVES ONTO A SHELF* (tech. rep.).
- Graham, J. M. (1980). The forces on sharp-edged cylinders in oscillatory flow at low Keulegan-Carpenter numbers. *Journal of Fluid Mechanics*, 97(2), 331–346. <https://doi.org/10.1017/S0022112080002595>
- Groh, R. (2016). Boundary layer separation and Pressure Drag. <https://aerospaceengineeringblog.com/boundary-layer-separation-and-pressure-drag/>
- Haage, S. S. (2018). Wave Flume Experiments on Permeable Structures, 1–127. <http://repository.tudelft.nl/>
- Holthuijsen, L. (2007). *Waves in Oceanic and Coastal waters*. Cambridge university press. Cambridge University Press.
- Jansen, W. J. (2019). Wave dissipation in a permeable structure. <http://resolver.tudelft.nl/uuid:acce330d-968a-46a7-853f-73137b06002a>
- Journée, J., & Massie, W. (2001). Offshore Hydromechanics, chapter 12 wave forces on slender cylinders. *Offshore Hydromechanics, Delft University of Technology*, (January).
- Keulegan, G., & Carpenter, L. (1958). Forces on cylinders and spheres in a sinusoidally oscillating fluid. *Journal of Research of the National Bureau of Standards*, 60(5), 423–440. <https://doi.org/10.1115/1.3423549>
- Korteweg, G., D.J. ; de Vries. (1895). On the change of form of long waves advancing in a rectangular canal, and a new type of long stationary waves. *Phil. Mag.*, 5(39), 442–443.
- Landmann, J., Ongsiek, T., Goseberg, N., Heasman, K., Buck, B. H., Paffenholz, J. A., & Hildebrandt, A. (2019). Physical modelling of blue mussel dropper lines for the development of surrogates and hydrodynamic coefficients. *Journal of Marine Science and Engineering*, 7(3), 1–15. <https://doi.org/10.3390/jmse7030065>
- Le Méhauté, B. (1976). *An Introduction to Hydrodynamics and Water Waves* (1st ed.). Springer, Berlin, Heidelberg. <https://doi.org/https://doi.org/10.1007/978-3-642-85567-2>

- Lewis, R. R. (2001). Mangrove Restoration - Costs and Benefits of Successful Ecological Restoration. *Mangrove Valuation Workshoop*, 4–8. <http://www.fao.org/forestry/10560-0fe87b898806287615fceb95a76f613cf.pdf>
- Marty, A., Schoefs, F., Soulard, T., Berhault, C., Facq, J. V., Gaurier, B., & Germain, G. (2021). Effect of roughness of mussels on cylinder forces from a realistic shape modelling. *Journal of Marine Science and Engineering*, 9(6). <https://doi.org/10.3390/jmse9060598>
- Morison, J., Johnson, J., & Schaaf, S. (1950). The Force Exerted by Surface Waves on Piles. *Journal of Petroleum Technology*, 2(05), 149–154. <https://doi.org/10.2118/950149-g>
- Munson, B. R., Young, D. E., & Okiishi, T. H. (1994). *Fundamentals of fluid mechanics*. <https://doi.org/10.1201/b15874-2>
- Nath, J. (1982). Heavily roughened horizontal cylinders in waves. *Proc. Conf. Behav. Offshore Struct.*, (1), 387–407.
- NWO, de Schipper, M. A., & Name, T. C. (2017). NWO domain Applied and Engineering Sciences (TTW) Open Technology Programme Project Title : EURECCA. (December), 1–21.
- Obasaju, E. D., Bearman, P. W., & Graham, J. M. R. (1988). A study of forces, circulation and vortex patterns around a circular cylinder in oscillating flow. *Journal of Fluid Mechanics*, 196, 467–494. <https://doi.org/10.1017/S0022112088002782>
- Page, H. M., & Hubbard, D. M. (1987). Temporal and spatial patterns of growth in mussels *Mytilus edulis* on an offshore platform: relationships to water temperature and food availability. *Journal of Experimental Marine Biology and Ecology*, 111(2), 159–179. [https://doi.org/10.1016/0022-0981\(87\)90053-0](https://doi.org/10.1016/0022-0981(87)90053-0)
- Primavera, J. H., & Esteban, J. M. (2008). A review of mangrove rehabilitation in the Philippines: Successes, failures and future prospects. *Wetlands Ecology and Management*, 16(5), 345–358. <https://doi.org/10.1007/s11273-008-9101-y>
- Rejeki, S., Debrot, A. O., van den Brink, A. M., Ariyati, R. W., Lakshmi Widowati, L., & Adolphe Debrot, C. O. (2021). Increased production of green mussels (*Perna viridis*) using longline culture and an economic comparison with stake culture on the north coast of Java, Indonesia. *Aquaculture Research*, 52, 373–380. <https://doi.org/10.1111/are.14900>
- Roshko, A. (1960). *Experiments on the flow past a circular cylinder at very high Reynolds number* (tech. rep.).
- Sarpkaya, T. (1986). Force on a circular cylinder in viscous oscillatory flow at low Keulegan-Carpenter numbers. *Journal of Fluid Mechanics*, 165, 61–71.
- Sarpkaya, T. (1977). In-line and transverse forces on cylinders near a wall in oscillatory flow at high Reynolds numbers. *Proceedings of the Annual Offshore Technology Conference, 1977-May*, 161–166. <https://doi.org/10.4043/2898-ms>
- Scaime. (2014). Aluminium single point load cell, 3 kg ... 30 kg.
- Schewe, G. (1983). On the force fluctuations acting on a circular cylinder in crossflow from subcritical up to transcritical Reynolds numbers. *Journal of Fluid Mechanics*, 133, 265–285. <https://doi.org/10.1017/S0022112083001913>
- Schlichting, H. (1955). Boundary Layer Theory.
- Stokes, G. (1847). On the theory of oscillatory waves. *Mathematical and physical papers*.
- Sumer, B. M., & Fredsoe, J. (1997). *HYDRODYNAMICS AROUND CYLINDRICAL STRUCTURES* (tech. rep.).
- Theophanatos, A., & Wolfram, J. (1989). *Hydrodynamic Loading on Macro-Roughened Cylinders of Various Aspect Ratios* (tech. rep.). <http://offshoremechanics.asmedigitalcollection.asme.org/>
- van Wesenbeeck, B. K., Balke, T., van Eijk, P., Tonneijck, F., Siry, H. Y., Rudianto, M. E., & Winterwerp, J. C. (2015). Aquaculture induced erosion of tropical coastlines throws coastal communities back into poverty. *Ocean and Coastal Management*, 116, 466–469. <https://doi.org/10.1016/j.ocecoaman.2015.09.004>
- van Wiechen, P. (2020). Wave dissipation on a fringing coral reef An experimental study.
- White, F. M. (2006). *Viscous Fluid Flow* 3rd ed.
- Williamson, C. H. K. (1989). *Oblique and parallel modes of vortex shedding in the wake of a circular cylinder at low Reynolds numbers* (tech. rep.).
- Wilms, T., Prusina, I., van der Goot, F., Tonneijck, F., & van Wesenbeeck, B. (2019). Building With Nature: Restoring Mangrove Coast. *38th IAHR World Congress - "Water: Connecting the World"*, 38(September), 3137–3142. <https://doi.org/10.3850/38wc092019-1894>
- Winterwerp, J. C., Albers, T., Anthony, E. J., Friess, D. A., Mancheño, A. G., Moseley, K., Muhari, A., Naipal, S., Noordermeer, J., Oost, A., Saengsupavanich, C., Tas, S. A., Tonneijck, F. H., Wilms, T., Van Bijsterveldt, C., Van Eijk, P., Van Lavieren, E., & Van Wesenbeeck, B. K. (2020). Managing erosion of mangrove-mud



- coasts with permeable dams – lessons learned. *Ecological Engineering*, 158(June), 106078. <https://doi.org/10.1016/j.ecoleng.2020.106078>
- Winterwerp, J. C., Borst, W. G., & De Vries, M. B. (2005). Pilot study on the erosion and rehabilitation of a mangrove mud coast. *Journal of Coastal Research*, 21(2), 223–230. <https://doi.org/10.2112/03-832A.1>
- Wolfram, J., & Naghipour, M. (1999). On the estimation of Morison force coefficients and their predictive accuracy for very rough circular cylinders. *Applied Ocean Research*, 21(6), 311–328. [https://doi.org/10.1016/S0141-1187\(99\)00018-8](https://doi.org/10.1016/S0141-1187(99)00018-8)

